INFORMATION TO USERS

This manuscript has been reproduced from the microfilm master. UMI films the text directly from the original or copy submitted. Thus, some thesis and dissertation copies are in typewriter face, while others may be from any type of computer printer.

The quality of this reproduction is dependent upon the quality of the copy submitted. Broken or indistinct print, colored or poor quality illustrations and photographs, print bleedthrough, substandard margins, and improper alignment can adversely affect reproduction.

In the unlikely event that the author did not send UMI a complete manuscript and there are missing pages, these will be noted. Also, if unauthorized copyright material had to be removed, a note will indicate the deletion.

Oversize materials (e.g., maps, drawings, charts) are reproduced by sectioning the original, beginning at the upper left-hand corner and continuing from left to right in equal sections with small overlaps. Each original is also photographed in one exposure and is included in reduced form at the back of the book.

Photographs included in the original manuscript have been reproduced xerographically in this copy. Higher quality 6" x 9" black and white photographic prints are available for any photographs or illustrations appearing in this copy for an additional charge. Contact UMI directly to order.

UMI

A Bell & Howell Information Company
300 North Zeeb Road, Ann Arbor MI 48106-1346 USA
313/761-4700 800/521-0600

NORTHWESTERN UNIVERSITY

Microstructure and Composition of Magnetic Flux Pinning Defects in High-Temperature Superconductors

A DISSERTATION

SUBMITTED TO THE GRADUATE SCHOOL
IN PARTIAL FULFILLMENT OF THE REQUIREMENTS

for the degree

DOCTOR OF PHILOSOPHY

Field of Materials Science and Engineering

By

Bradford George Storey, III

EVANSTON, ILLINOIS

December 1996

ABSTRACT

Microstructure and Composition of Magnetic Flux Pinning Defects in High-Temperature Superconductors

Bradford G. Storey, III

The superconducting coherence length in $YBa_2Cu_3O_{7-x}$ is extremely small, 15-30 Å parallel to the a-b plane and 2-4 Å parallel to the c-axis. This small coherence length results in superconducting properties which are extremely sensitive to small defects, even those on the atomic scale. Point defects, defect clusters, and small regions of disorder are known to enhance the critical current density by effectively pinning the magnetic vortices.

TEM was used to investigate the structure of small defects in $YBa_2Cu_3O_{7-x}$, the defects studied include: point defect clusters in as-grown Au-doped $YBa_2Cu_3O_{7-x}$, 3.5 MeV proton irradiation induced point defects and defect clusters, and defect cascades resulting from 50 keV Kr^+ irradiation. Defect features such as: size, shape, strain field, density, and atomic models are proposed.

As chemical substitution can also enhance the critical current density, Cr doping of the Hg site in $HgSr_2CuO_{4+\delta}$ was investigated. TEM revealed an incommensurate chemical modulation containing some disorder within the modulation. These results were combined with the average local defect structure obtained by Reitveld refinement of powder-

neutron-diffraction data to generate a complete structural model of the Cr substitution. A similar project involving Cr doping of $HgBa_2CuO_{4+\delta}$ system was underway as this thesis was nearing completion. There was no evidence, however, for any modulation.

Approved by

Professor Laurence D. Marks (Thesis advisor)
Department of Materials Science and Engineering
Robert R. McCormick School of Engineering and Applied Science
Northwestern University, Evanston, IL 60208

To my mother for all the boat rides to Timbuktu and Kalamazoo. To Lillian go with peace in your soul, love in your heart, and no regrets.

CONTENTS

TABLES

FIGURES

ACKNOWLEDGMENTS

I would like to thank my two advisors Prof. Laurie Marks and Dr. Mark Kirk for helping to make this dissertation possible. Laurie's guidance and motivation along with Mark's understanding, patience, and willingness to listen are greatly appreciated.

Thanks go to Prof. Vinayak Dravid and his research group for participating in a joint group meeting with Dr. Mark's group and his thoughtful suggestions and critique regarding my work. I would also like to thank Dr. Julia Weertman for her time and consideration as a member of my thesis committee.

To my fellow labmates from the early years, Jinping, Ganesh, Dorai, Boris, and Derren, thanks for helping me adjust to grad school and all of its intricacies. Dan's multiple proof readings of this thesis are appreciated.

Several people at Argonne National Laboratory deserve recognition for their assistance: Dr. Boyd Veal for growing YBCO single crystals, Dr. Peter Kostic for making T_c measurements, and Dr. Loren Funk and Pete Baldo for performing the ion irradiations.

Without the outstanding service of the Hitachi H-9000 by Jim Poulis this whole project would have been significantly harder. His service was so quick and sure that I would not have come to know him except for his pleasant conversation and good humor.

Thanks to Dave Popp for catching me running in the hall as a ninth grader and making me sit in his chemistry class through lunch. He got me interested in science and is by far the best teacher I have ever had the

privilege to learn from. Thanks also to Dave Luzzi for showing me the world through a microscope.

This research was supported by the National Science Foundation under contract No. DMR 91-20000 through the Science and Technology Center for Superconductivity.

ACRONYMS AND SYMBOLS

ANL	Argonne National Laboratory
B	Internal magnetic field
BF	Bright-field
C_s	Spherical aberration coefficient
DF	Dark-field
E_d	Threshold displacement energy
EDS	Energy dispersive x-ray spectroscopy
FOLZ	First order Laue zone
g	Reciprocal lattice vector
H	External magnetic field
H_c	Upper limit of external magnetic field for superconductors
H_{c1}	Below this field B = 0 in Type II superconductors
H_{c2}	Upper limit of H for Type II superconductors
HREM	High-resolution electron microscopy (or microscope)
HVEM	High-voltage electron microscope
J_c	Critical current density
λ	Magnetic penetration depth
R	Stacking fault displacement vector
SA	Selected area
SAD	Selected area diffraction
SQUID	Superconducting quantum interference device
T_c	Critical transition temperature
TEM	Transmission electron microscopy (or microscope)
TRIM	Monte Carlo Radiation Simulation Program - Transport of Ions in Matter
ξ	Coherence length
ξ_g	Extinction distance for a particular **g**
u	Spatial frequency
YBCO	$YBa_2Cu_3O_{7-x}$
Δz	Objective defocus
ZOLZ	Zero order Laue zone

INTRODUCTION

Widespread research on high-T_C superconductors began in 1986 when Bednorz and Müller introduced the La-Ba-Cu-O system with an onset critical transition temperature (T_C) of 30 K (Bednorz and Müller 1986). Research further intensified with reports of even higher T_C's in similar ceramic systems (Chu et al. 1987; Wu et al. 1987). The most studied compound has been $YBa_2Cu_3O_{7-x}$ (YBCO) where $0<x<0.6$ for the superconducting state and it has an optimal T_C of 93 K for $0<x<0.1$ (Rothman et al. 1991).

A major obstacle to practical applications of YBCO is a low critical current density (J_C). All high-T_C superconductors allow an external magnetic field to penetrate as vortices of quantized magnetic flux and are known as type II superconductors. Current in a type II superconductor imposes a Lorentz force on the internal magnetic flux lines; if the flux lines yield to this force and move, the material will show resistance. Therefore, to enhance J_C much research has been done to develop the theory of magnetic flux pinning (Abrikosov 1957; Anderson and Kim 1964; Clem 1992; Dew-Hughes 1974; Kes 1987). Defects were found to pin the magnetic flux effectively; although, the type, size, and shape of a defect strongly influence its flux pinning strength. In YBCO the most studied defects are irradiation damage induced defects, although intrinsic defects have also been studied including: dislocations (Jin et al. 1991; Kirk et al. 1988), precipitates (Jin et al. 1991; Kulik 1991; Li et al. 1988), and twins (Kvam 1992; Kwok et al. 1991).

Irradiation damage induced defects are effective magnetic flux pinning centers; hence, they enhance J_C significantly. In the attempt to maximize J_C

many forms of irradiation have been employed: electrons (Giapintzakis et al. 1992), protons (Civale et al. 1990; Kirk 1993), neutrons (Lessure et al. 1991; Vlcek et al. 1992), and ions (Budhani, Zhu, and Suenaga 1992; Civale et al. 1991). Depending upon the energy and mass of the bombarding particle a wide variety of defects are generated. Electrons and light ions predominately produce Frenkel pairs and clusters of vacancies or interstitials. Fast neutrons produce several types of damage dominated by defect cascades and smaller cluster defects (Frischherz et al. 1994; Vlcek et al. 1992). GeV ions leave continuous tracks of damage greater than several microns in length (Wheeler et al. 1993). Knowing the defect structure of tracks, cascades, or small clusters of interstitials or vacancies is important in relating a defect type to its flux pinning properties.

The crux of this thesis was to investigate the structure, chemical composition, and stability of defects in YBCO using various transmission electron microscopy (TEM) techniques. Three types of defects in YBCO single crystals were investigated: point defects in as-grown Au-doped YBCO single crystals, defects produced by 3.5 MeV proton irradiation, and defect cascades produced by 50 keV Kr^+ irradiation. In order to estimate the flux pinning strength of a particular defect, magnetic property measurements are required. Consequently, work was done in collaboration with researchers at Argonne National Laboratory (ANL), to make magnetic property measurements on the YBCO crystals before and after irradiation.

An alternate method of creating defects in high-T_c materials is by chemical substitution. Hopefully this will lead to a more feasible industrial process for mass producing superconducting devices with strong as-grown

magnetic flux pinning sites. To this extent, Chap. 6 deals with a chemical modulation resulting from the partial substitution of Cr on the Hg site in $Hg(Sr,Ba)_2CuO_{4+\delta}$; the doped material exhibits enhanced magnetic flux pinning.

An aspect of this thesis that is primarily of interest as a TEM technique but also has relevance as a materials science issue is the investigation of point defects. There is a belief by many that TEM is incapable of imaging point defects; hence, they are often referred to as invisible. The work presented in Chaps. 3 and 5 clearly demonstrates the fallacy in this belief. Not only is there evidence of point defects in the electron diffraction patterns and high resolution images, but through careful modeling and image simulation the structure of point defect clusters can be discerned.

Chapter 1 BACKGROUND

This chapter reviews the relevant theory and information fundamental to this work. There are three subsections: 1.1 provides a background in superconductivity theory emphasizing magnetic flux pinning, 1.2 contains the crystallographic structures and relevant physical properties of the materials to be studied, finally 1.3 discusses some of the theory involved in irradiation damage considering both electronic and nuclear stopping mechanisms.

1.1 Superconductivity and Magnetic Flux Pinning

The phenomenon of superconductivity was discovered in 1911 by Kamerlingh Onnes (Onnes 1911). Initially, superconducting materials were envisioned carrying large currents thereby generating large magnetic fields with no power loss. It rapidly became apparent, however, that the known superconductors of the time, certain pure metals (e.g., Hg, Sn, and Pb), loose their superconducting state under modest currents; thus, only small magnetic fields could be generated. When a superconductor is placed in a weak magnetic field, it completely expels the field from the superconducting material except for a layer at the surface of thickness equal to the penetration depth. This phenomenon of perfect diamagnetic behavior is referred to as the Meissner effect (Meissner and Ochsenfeld 1933). Materials requiring perfect diamagnetic behavior to be superconducting are known as type I, soft,

Pippard, or superconductors of the first kind. These materials have an upper limit on the magnetic field that they will expel before returning to a non-superconducting or normal state. This critical magnetic field (H_C) can be either an externally imposed magnetic field or generated by the superconducting current. H_C depends on the Gibb's free energy difference between the superconducting state and the normal state; thus, it is a function of temperature which increases with decreasing temperature. That is, if $T = T_C$ then $H_C = 0$ and as T decreases to 0 K, H_C increases to its maximum value.

In the 1930's it was realized that some materials remain superconductors at magnetic fields higher than H_C (now referred to as H_{C1}), by allowing the external magnetic field to penetrate the material by creating columns of non-superconducting or normal material known as vortices (Gorter 1935; London 1935; Mendelssohn and Moore 1935). These superconducting materials are known as type II, London, hard, or superconductors of the second kind and they allow this penetration of the magnetic field up to a second critical magnetic field H_{C2}. A negative normal-superconducting interfacial energy permits the penetration of magnetic flux internally in type II materials, while type I superconductors have a positive interfacial energy which prohibits magnetic flux penetration (Abrikosov 1957). The internal magnetic field is quantized (London 1950), and a given column or vortex contains a single quantum of magnetic flux (Parks 1965).

There are several important material parameters used in superconducting theory and its applications. The penetration depth (λ) was first introduced in 1925 by Mrs. de Haas (Gorter 1964) and further developed by Frank London. For type I superconductors λ represents the depth of

surface penetration by an external magnetic field. In type II superconductors λ is also the penetration depth up to H_{c1}, but may be thought of as an upper limit on the vortex diameter when the magnetic field is between H_{c1} and H_{c2}.

In 1953, Brian Pippard introduced a coherence length (ξ_0), as a measure of the superconducting electron's non locality (Pippard 1987). The coherence length is a function of the defect concentration, where ξ_0 is reserved for defect free pure materials near 0 K and ξ is used otherwise. The coherence length is now considered to be the size of a Cooper pair, i.e., a pair of electrons with spins of equal magnitude but opposite polarity. The concept of Cooper pairs was introduced by the BCS theory in 1957 which is still accepted as an accurate theory for classic low temperature superconductor behavior (Bardeen, Cooper, and Schreiffer 1957). The Ginzburg-Landau parameter (κ) is the ratio of λ to ξ, and Abrikosov demonstrated that for $\kappa < 2^{-1/2}$ the material is type I and type II for $\kappa > 2^{-1/2}$ (Abrikosov 1957). In YBCO $\lambda_{ab} \approx 30$ nm and $\xi_{ab} \approx 2$ nm, it follows that $\kappa_{ab} \approx 15$; thus, YBCO is certainly a type II superconductor.

As mentioned previously, type II superconductors have vortex cores of normal state material which contain a quantum of magnetic flux. In the absence of any current or defects the vortices will repel each other and form a triangular lattice (Abrikosov 1957). When a current is applied to the superconductor, however, there will be a Lorentz force on the vortices in the direction of $\mathbf{J}\times\mathbf{B}$. If this Lorentz force exceeds the pinning force holding the vortices in place, the vortices will move. Vortex motion sets up an electric field opposing the superconducting current, leading to a dissipation of

energy. This resistance heats the sample locally and can create a positive feedback loop leading to a complete loss in the superconducting current. Consequently, if the current density surpasses a critical value (J_c), vortices will flow and a normal state resistance will be realized. Therefore, much research is done to produce strong flux pinning defects.

Because defects create a volume of material with a lower (possibly zero) superconducting order parameter, i.e., density of superconducting electrons, magnetic vortices align themselves with defects. Pinning occurs at defects because it costs less energy if the vortex core is at a site that is normal, than if it has to transform a superconducting region into a normal one. It should also be noted that most high-T_c superconductors are highly anisotropic; thus, a defect's pinning force depends upon the crystallographic directions of **J** and **B**.

1.2 Cuprate Superconductors

The majority of high-T_c superconductors contain CuO_2 planes in which the density of superconducting electrons, i.e., Cooper pairs, is highest. The Y-Ba-Cu-O system, described in 1.2.1, has been exhaustively studied and is the primary material used in this work. A short section describing the structure of the single layer $HgBa_2Ca_{n-1}Cu_nO_{4+\delta}$ system is also presented.

1.2.1 $YBa_2Cu_3O_{7-x}$

In 1987 Wu reported that $YBa_2Cu_3O_{7-x}$ (YBCO) has an onset T_c of 93 K with a transition width less than 0.5 K (Wu et al. 1987). The YBCO structure is a triple perovskite unit cell with two CuO_2 planes perpendicular to the

long axis of the unit cell. This orthorhombic structure was determined in 1987 using neutron diffraction, is illustrated in Fig. 1.1, and has two main crystallographic features of interest (Jorgensen et al. 1987). The first is the CuO_2 planes above and below the Y atom which provide the primary superconducting path in the material. The other structural feature to note is the CuO chains that lie in the [010] direction. This oxygen ordering makes the unit cell orthogonal in which the a-axis is slightly smaller than the b-axis. The CuO chains are generally referred to as "isolation planes" or "charge reservoirs" for the superconducting CuO_2 planes.

The most common intrinsic defects in the orthorhombic structure, besides oxygen vacancies, are (110) twins. Due to the orthorhombic structure, the [110] directions that are nearly perpendicular to the twin plane are nonparallel. This in turn results in a slight splitting of the (110) spots in a [001] zone axis electron diffraction pattern (assuming it is taken from an area that includes a twin boundary). As the oxygen deficiency increases, the b:a ratio approaches unity and a tetragonal structure evolves. Therefore, it is possible to correlate the degree of spot splitting in a diffraction pattern with the oxygen concentration. A graph of this relationship is provided in Fig. 1.2.

As will be discussed later, in regard to proton irradiation, one proposed defect is copper oxide interstitial platelets in the b-c plane created by the migration and coalescence of Cu and O point defects. Studies of oxygen tracer diffusion in single crystal YBCO have found that oxygen diffusion is highly anisotropic with the b-axis being the preferred diffusion direction (Rothman et al. 1991). Another tracer diffusion study indicates that the

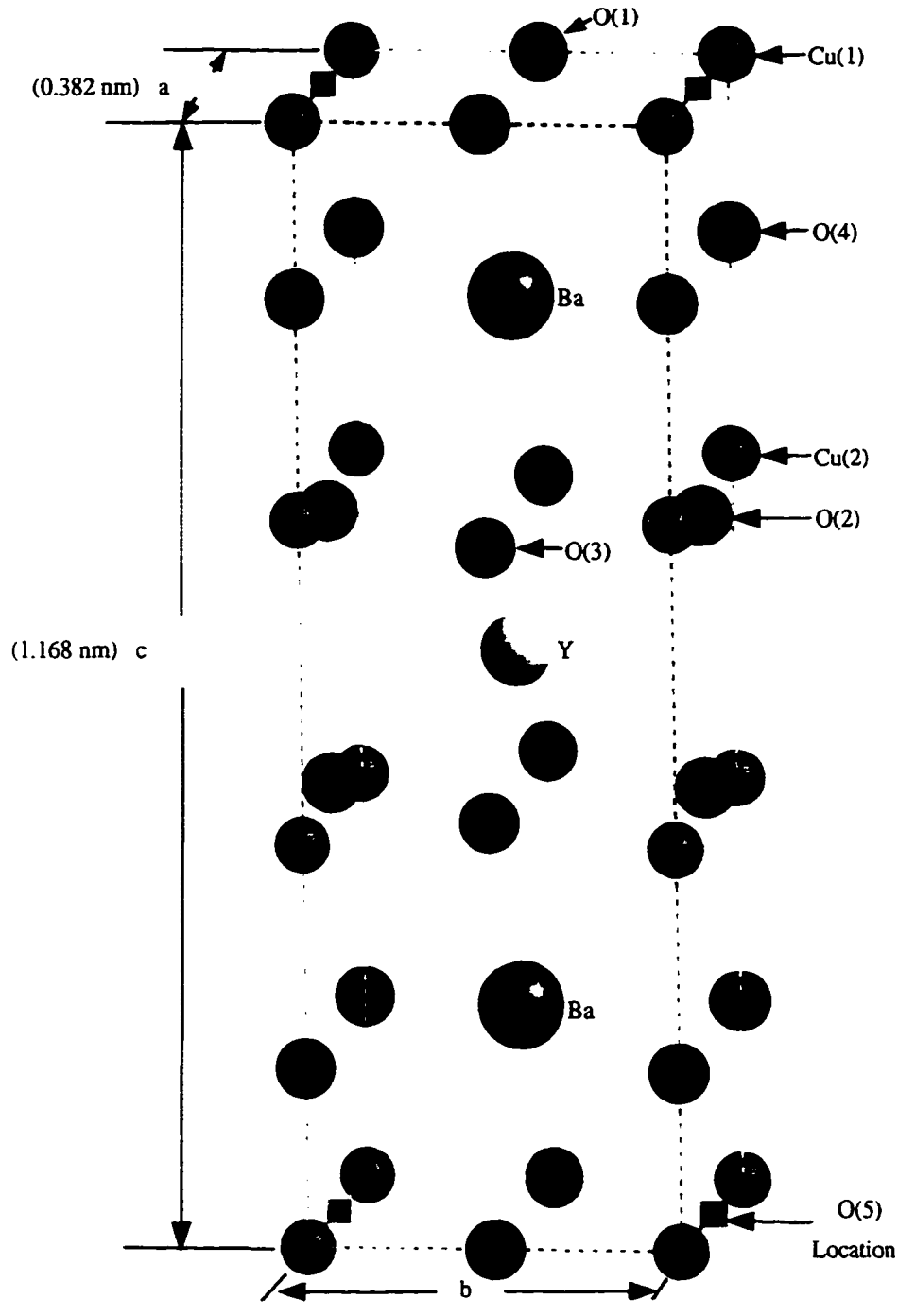

Figure 1.1 Schematic for the $YBa_2Cu_3O_{7-x}$ orthorhombic unit cell. Oxygen vacancies typically occupy the O(1) site, note that the O(5) site is normally vacant and is not considered as an oxygen vacancy.

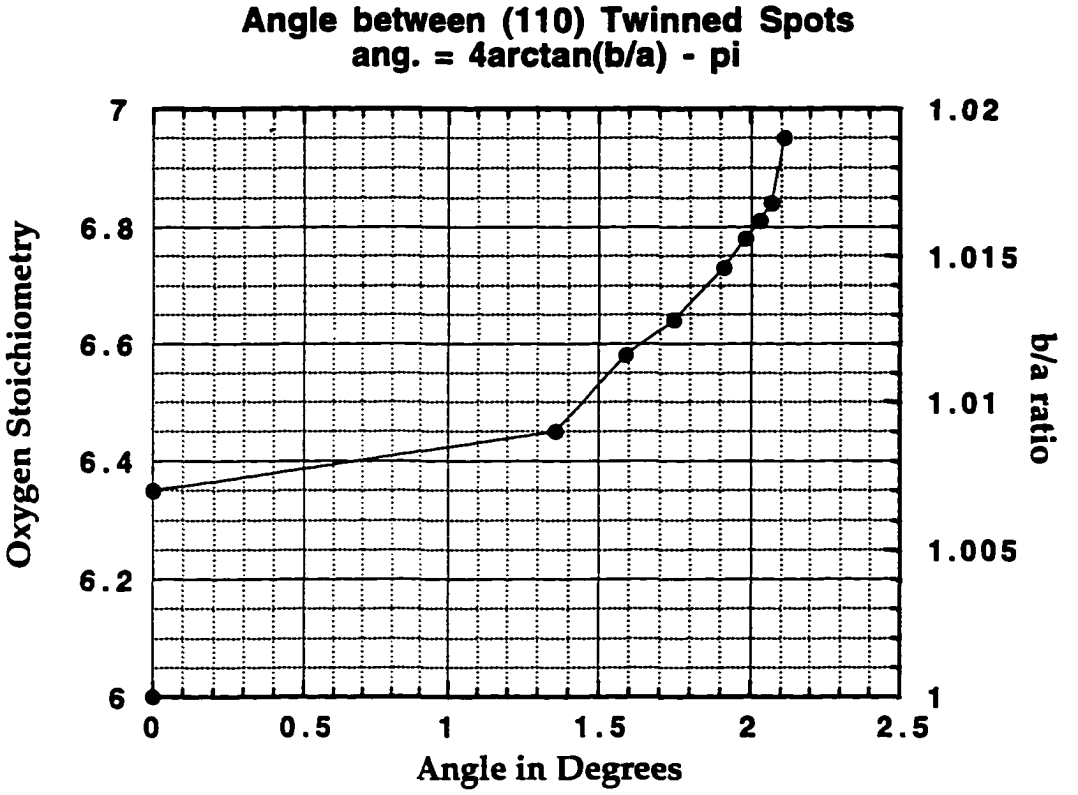

Figure 1.2 Plot of the oxygen content vs. the angle between (110) twinned reflections in an electron diffraction pattern. Note that as the oxygen content decreases, b/a goes to one, i.e., the structure transforms from orthorhombic to tetragonal. The relationship between the oxygen content and the lattice parameters was taken from an x-ray study by Cava et al. 1990.

diffusion rates of O and Cu are much faster than Ba or Y (Chen et al. 1992). The oxygen diffusion mechanism in the b-direction was proposed to be O(1) atoms jumping into the normally vacant O(5) lattice position and rapidly moving to the next O(5) position until an empty O(1) site was encountered and occupied; the key being that diffusion does not occur by random oxygen motion in the a-b plane, instead it occurs along the empty O(5) channels. They also found the diffusion rates to be largely independent of oxygen partial pressure. In another diffusion study, YBCO was found to lose oxygen

at room temperature very slowly and not lose significant amounts of oxygen until about 350 °C in either vacuum or non-oxygen environments (Kishio et al. 1989). This was also observed when YBCO TEM samples were heated in-situ to 400 °C without any structural change. At 400 °C, however, the sample rapidly transformed into a tweed structure (Iijima et al. 1987; Zhu, Suenaga, and Moodenbaugh 1991) indicating that the sample was losing a significant amount of oxygen.

1.2.2 Mercury Based Materials

The first Hg-based cuprate high-T_c superconductor was discovered in 1993 with an onset T_c of 94 K (Putilin et al. 1993). Various dopants have been attempted to either stabilize the compounds or enhance T_c, and $HgBa_2Ca_2Cu_3O_y$, in particular, showed record-high T_c's of 134 and 164 K under ambient and high pressures (31 GPa), respectively (Gao et al. 1994). High pressure synthesis is an impractical sample preparation technique, but it provides evidence that higher T_c's can be achieved. Knowledge of the high pressure synthesized material's structure may provide insight on what to alter in materials prepared under ambient conditions, so that practical T_c enhancements may be realized.

The material used in this work was $Hg_{1-x}Cr_x(Ba,Sr)_2CuO_{4+\delta}$ which has a single CuO_2 layer per unit cell. A collaboration with Dr. Jorgensen's group at ANL investigated $(Hg_{1-x}Cr_x)Ba_2CuO_{4+\delta}$ $(0<x<0.4)$ and $(Hg_{0.6}Cr_{0.4})Sr_2Cu\text{-}O_{4+\delta}$. A schematic of the basic undoped structure is provided in Fig. 1.3. The details of the Cr substitution into each compound are the province of Chap. 6 and will not be discussed here.

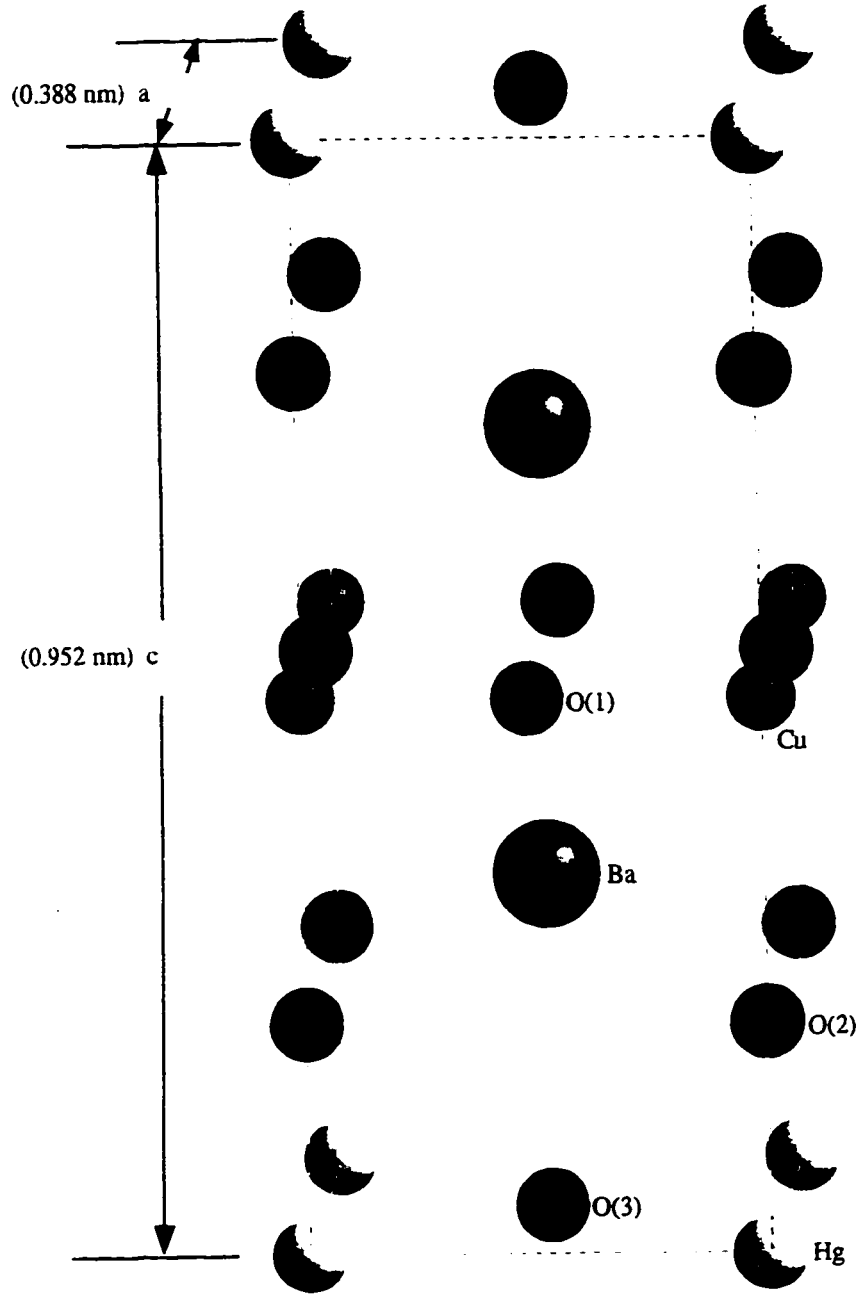

Figure 1.3 Schematic of the undoped $HgBa_2CuO_4$ unit cell.

1.3 Irradiation Damage

This work used an electron probe to study the atomic structure of native point defects and small irradiation induced defects. Hence, there are two areas of interest concerning irradiation damage theory: the desired ion irradiation effects and the unavoidable electron irradiation effects inherent to TEM analysis.

There are many types of irradiation, for instance: ions, electrons, neutrons, protons, and photons. Regardless of the projectile, however, irradiation damage is the result of either elastic or inelastic collisions each of which can occur by several mechanisms. This section contains a brief review of irradiation damage theory with a focus on the relevant details unique to ion and electron irradiation.

1.3.1 Knock-On Damage

A fraction of the trajectile's energy will be transferred to the sample in elastic collisions. These collisions (knock-on damage) require both the momentum and kinetic energy of the particles involved to be conserved. In a single collision, the projectile may transfer to the target atom any fraction of energy between a minimum and maximum quantity, through a Coulombic interaction. The minimum transferable energy, T_{min}, is established by the lowest energy phonon vibration mode, and the maximum transferable energy, T_{max}, is given below in equation 1.1

$$T_{max} = \frac{4M_1M_2}{(M_1 + M_2)^2} E_1 \qquad 1.1$$

where M_2 is the mass of the target atom, and M_1 and E_1 are the mass and energy of the projectile respectively. This equation is for the non-relativistic case and applies here, as the proton energy in this experiment is 3.5 MeV which yields a wavelength of 0.153 x 10^{-4} nm and velocity of 2.58 x10^7 m/s (8.6% of the speed of light); similarly, 50 keV Kr^+ is also non-relativistic. If the energy transferred is small, then the projectile is scattered through a small angle and the target atom will vibrate around its lattice position, causing local heating. If, however, the energy transfer is greater than the threshold energy (E_d) required to displace the target atom from its lattice position into a distant interstitial site, a stable Frenkel pair will be created. This is commonly known as ballistic knock-on displacement. Furthermore, if the energy transferred is substantially greater than E_d then the target atom may recoil into neighboring atoms causing multiple secondary displacements, which in turn generate further displacements. This continues until all of the particles involved have an energy less than E_d and results in a branched region of highly disordered material, referred to as a defect cascade.

1.3.2 Radiolytic Damage

The other energy transfer process is an inelastic collision. This requires the conservation of momentum and total energy; the distinction here is that the kinetic energy is not conserved. Energy is transferred to the target atom when a closely bound or inner core electron is excited out of its ground state. Displacement damage resulting from this process is known as radiolysis or ionization damage. The excited electron may either decay back

to the ground state or generate a defect. According to Hobbs there are five criteria necessary for damage production by radiolysis: (1) The excitation must be localized to a few atomic sites. (2) The excitation must have a lifetime longer than the phonon period to couple into a mechanical response of the nuclear mass ($\approx 10^{-13}$ s). (3) The available excitation energy must be comparable to the atomic displacement energy in its excited state. (4) The recombination energy must be substantially larger than the heat of formation required to form defects. (5) An energy-to-momentum conversion must exist and compete favorably with other excitation decay modes (Hobbs 1979) .

Both radiolytic and knock-on damage occur in 3.5 MeV proton irradiation of YBCO. Figure 1.4 provides insight to the defect size distribution. The lower energy primary recoils (< 100 eV) generate point defects, while small defect cascades are formed by the larger recoils (> 10 keV). The bulk (80%) of the damage appears to be point defects; however, it is likely that some point defects migrate and coalesce to form larger defects. Since oxygen and copper point defect are the primary diffusing species at room temperature, the larger defects found experimentally could be copper oxide precipitates. Figure 1.4 should be used semi-quantitatively at best, due to the difficulties in simulating the interaction of YBCO with an energetic particle. Two of these difficulties are modeling the crystal with accurate displacement energies for each atomic position and accounting for multiple collisions. Unlike proton irradiation, 50 keV Kr^+ irradiation results primarily in defect cascades, i.e., a small (2-5 nm) highly disordered volume. After the initial displacement process (10^{-13} s), the atoms in the cascade core

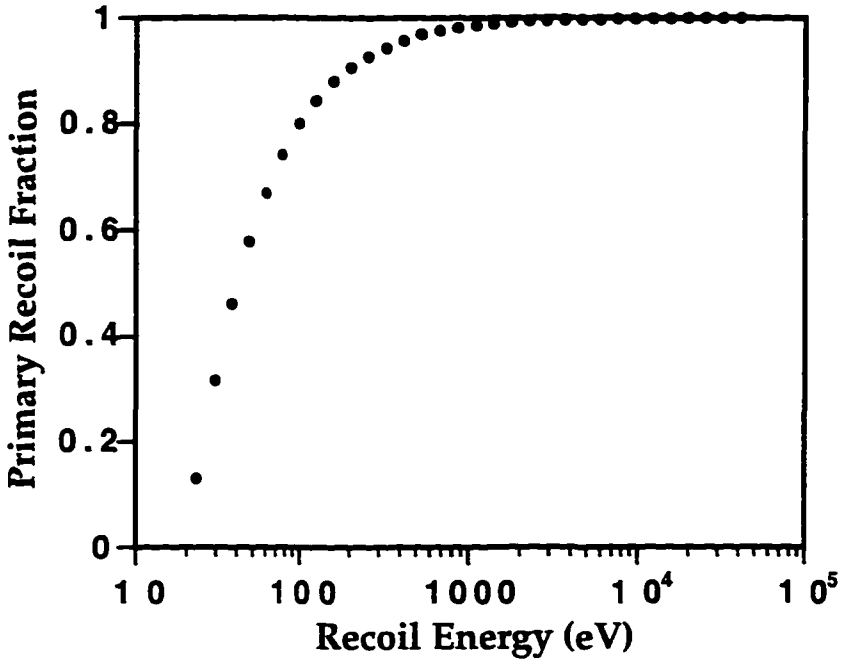

Figure 1.4 Integral recoil fraction as a function of recoil energy for 3.5 MeV protons in YBCO.

are highly energetic and are essentially in a molten state, this is referred to as a thermal spike (Brinkman 1954; Diaz de la Rubia et al. 1987; Seitz and Koehler 1956). The energy is dissipated primarily as heat; hence, the cooling or quenching rate is controlled by the thermal conductivity which in YBCO is highly anisotropic. This anisotropy may control the final shape of a defect cascade (see Chap. 4).

1.3.3 TEM Induced Damage

Point defects are primarily generated by 100-400 keV (operating voltage range in a TEM) electrons. By changing the accelerating voltage of the electrons, different atomic sub-lattices in YBCO can be displaced. Experimental evidence (Basu et al. 1989; Kirk et al. 1988) and molecular

dynamic simulations (Kirsanov, Musin, and Shamarina 1994; Kirsanov, Musin, and Shamarina 1992) indicate that 100 keV electrons are below all knock-on damage threshold energies, except one planar oxygen site (O2) when the electron beam is near the a, b, or c axes. Considering that the experimental work, mentioned above, did not observe any basal plane oxygen disordering with time while at 100 keV (the author's observations concur), radiolytic damage is also negligible. Therefore, unless higher resolution is required, one should not operate the electron microscope above 100 keV when studying YBCO.

The previous paragraph is in regard to a perfect YBCO structure. Defects, however, have a much lower threshold for irradiation damage and point defects can migrate under certain irradiation conditions. It was a concern in this project that the very act of observing the point defect clusters with an electron probe would alter their structure. To combat this problem, diffraction patterns and images were often obtained at the start of a session so that if changes in the defect structures occurred they could be seen with time.

Chapter 2 EXPERIMENTAL TECHNIQUES

2.1 Crystal Growth

2.1.1 $YBa_2Cu_3O_{7-x}$ Single Crystals

The flux melting technique (Kaiser et al. 1987) was used by Dr. Veal to grow YBCO single crystals, typically 1x1x0.05 mm^3 in size. The crystals were grown in a Au crucible resulting in the substitution of Au for Cu(1) at approximately 1 Au atom per 10 unit cells, see Chap. 3 for further details. Oxygenation was accomplished by slowly cooling the crystals from the growth conditions to 480 °C in oxygen and then annealing for a few days. They were further cooled to about 420 °C, annealed for a few more days, and finally furnace cooled to room temperature; the crystals were stored in open air. Fully oxygenated crystals of the proper size were then selected. Numerous twins ensure an orthorhombic structure and are visible with the aid of a low power light microscope. Crystals with unremovable flux must be avoided for two reasons: it will screen the crystal from the proton irradiation and it will contaminate the surface of the TEM sample. A few YBCO crystals were grown in ZrO_2 crucibles by Dr. Giapintzakis at the University of Illinois at Urbana Champaign. There is very little Zr substitution (typically 1-2 ppm); the crystals, however, are often an order of magnitude smaller in volume.

2.1.2 $Hg_{1-x}M_x(Ba,Sr)_2Ca_{n-1}Cu_nO_{4+\delta}$ Powder

Mercury based superconducting powders were prepared by Dr. Chmaissem at ANL. Both $HgSr_2CuO_{4+\delta}$ and $HgBa_2CuO_{4+\delta}$ powders were prepared with Cr partially substituted for Hg. HgO, Cr_2O_3, $Sr(NO_3)_2$, and CuO powders were mixed to provide an overall composition of $Hg_{0.7}Cr_{0.3}Sr_2CuO_{4+\delta}$ (Chmaissem et al. 1995; Chmaissem, Deng, and Sheng 1995).

To prepare the compound containing Ba, the same procedure as for the Sr compound was used but with $Ba(NO_3)_2$ instead of $Sr(NO_3)_2$ (Chmaissem et al. 1996). Several batches of powder were prepared with different nominal doping levels of Cr in $Hg_{1-x}Cr_xBa_2CuO_{4+\delta}$ where the values of x include: 0.1, 0.2, 0.3, and 0.4. As will be shown in Chap. 6 a saturation limit of $x \approx 0.35$ was found based on energy dispersive x-ray spectroscopy (EDS). As a side note, it was found that the Sr material could be successfully crushed in methanol while the Ba material reacted rather rapidly.

2.2 *TEM Sample Preparation*

Preparing materials for TEM evaluation is an art form and is recognized as difficult. The damage resulting from the method employed, however, is often either overlooked or ignored. A thin (10-100 nm) crystal must be obtained in order to perform the TEM experiments. This was accomplished by mechanically crushing the crystals in anhydrous methanol. Crushing was chosen over ion milling as small irradiation defects are being investigated; the large number of point defects generated by ion milling may

react with the irradiation defects and eliminate them. The high level of surface contamination resulting from chemical or electropolishing makes these poor alternatives for generating thin regions of the sample. Crushing has the advantage of quick sample preparation time but a disadvantage in the extra microscope time required to find a thin crystal with the proper orientation.

A reliable method for crushing very small brittle crystals was established by Drs. Kirk and Frischherz at ANL while investigating neutron irradiation damage in YBCO. The idea is to take a glass tube, with an inner diameter of ~3 mm, and round off one end to create a mortar. The end of a 2.5 mm diameter glass rod is then rounded to match the rounded bottom of the tube, creating the pestle (see Fig. 2.1). It is critical that the rounded end of the glass rod fits into the end of the tube without gaps. This enables one to gently crush a small crystal in just a few drops of liquid. After the crystal is crushed, the powder, suspended in fresh anhydrous methanol, is extracted via a pipette and dispersed onto a clean 1000 mesh TEM grid. As new TEM grids are often rather dirty, it is necessary to clean them. This can be accomplished by suspending a new grid with self-closing anti-capillary tweezers in a beaker of methanol and ultrasonically cleaning it for at least one minute. All the other components should also be ultrasonically cleaned in methanol for 5-10 minutes and dusted off with compressed air. The entire operation should be performed over a lint free, cleanable surface, e.g., glass or preferably a large sheet of Teflon. This procedure for crushing reduces sample damage compared to ion-milling or chemical polishing (St. Louis-Weber, Dravid, and Balachandran 1995) and limits the exposure to the

deleterious effects of water (Marks et al. 1988; van Tendeloo and Amelinckx 1988).

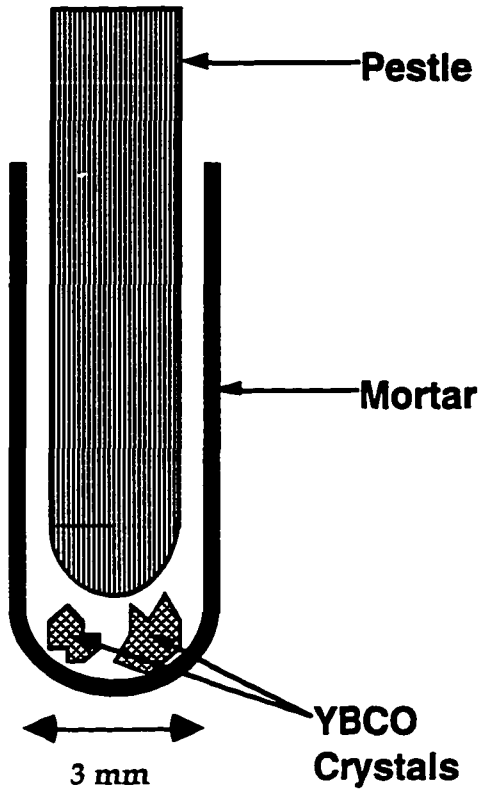

Figure 2.1 Schematic of the system for crushing small single crystals.

The Hg-based superconducting powders were also crushed. They tended to react, however, with methanol as well as other solvents; hence, they were dry crushed between two clean glass slides. The crushed powder was simply placed onto holey carbon thin films supported by 400 mesh Cu or Mo TEM grids. The Mo grids were used during EDS analysis of the Cu stoichiometry.

2.3 Storage of TEM Samples

The TEM samples were stored in a glass bell jar with a lid that enabled the jar to be evacuated. The vacuum was obtained with a sorption pump (no oil contamination or vibration), and the system was flushed out several times with oxygen or nitrogen. If nitrogen gas is used, it is advisable to run the gas line though a liquid nitrogen bath in order to remove impurities, namely, water and carbon dioxide. The final state is static oxygen or dry nitrogen at about 0.5 atm. This system keeps carbon dioxide and water vapor from reacting with the sample. TEM samples stored in this manner were successfully reused several months later.

2.4 Ion Irradiation Damage

Irradiation induced magnetic flux pinning defects were created only in YBCO, although several oxygen stoichiometries as well as Au-doped material were used. All irradiations were performed at room temperature. Both 50 keV Kr^+ and 3.5 MeV protons were used; experimental details for each are described in the following two subsections. For a discussion of the damage mechanisms and defect production refer to 1.3.

2.4.1 3.5 MeV Protons

Crystals less than 50 microns in thickness (c-axis) were selected and cleaned in anhydrous methanol. 3.5 MeV protons can penetrate up to 50 microns in YBCO and maintain uniform damage rates, see Fig. 2.2; hence, crystals thicker than 50 microns are to be avoided. Prior to the proton irradiation the crystals were mounted on aluminum stubs with silver epoxy.

The epoxy must not cover the top of the crystal as this would screen the crystal from the protons. Good thermal contact between the stub and the crystal is required to prevent heating during the irradiation. Dr. Baldo performed the irradiations at room temperature in the HVEM-Tandem facility (Allen et al. 1989) at ANL with 3.5 MeV protons to fluences of: 0.6, 1, 2, and $3x10^{16}$ $H^{+}\cdot cm^{-2}$. To avoid channeling effects the proton beam was aligned 10° off of the c-axis. Methanol was used to dissolve the silver epoxy in order to remove the crystals from the Al stub.

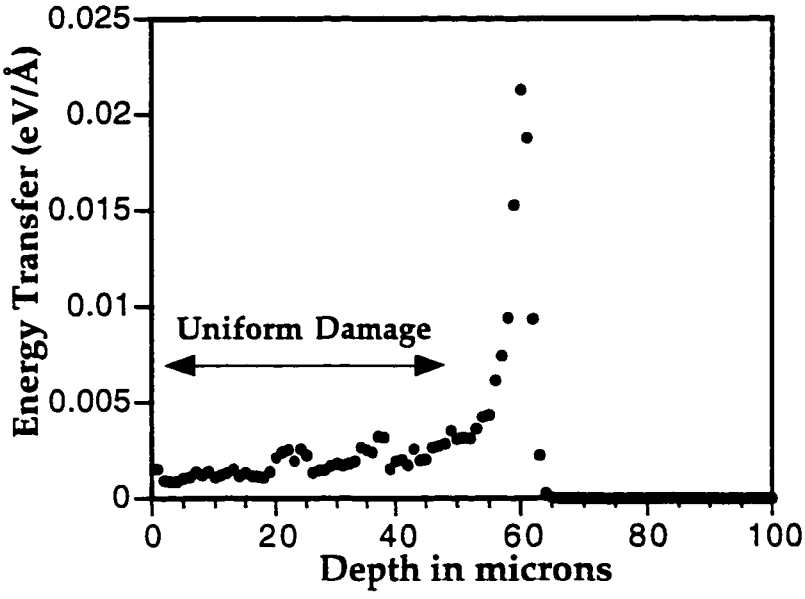

Figure 2.2 Energy transferred by 3.5 MeV protons as function of penetration depth in YBCO.

2.4.2 50 keV Krypton Ions

Unlike the proton irradiation, the Kr^{+} irradiation was performed on TEM samples. This is because while the protons penetrate 50 microns, Kr^{+} travels at most 35 nm before stopping. Prior to irradiating the crushed YBCO

crystals, a region of the TEM grid containing thin clean crystals with favorable orientations was located. The irradiation was performed in the HVEM-Tandem facility (Allen et al. 1989) at ANL with the ion beam centered on the aforementioned region. Dosimetry was done with a Faraday cup which had been calibrated earlier (Vetrano 1990). A National Electronics Corporation ion implanter delivered 50 keV Kr^+ through an ion beam interface into the sample area of the high voltage electron microscope. A fluence of $2x10^{11}$ ions·cm^{-2} was used so that the defect density would be sizable but without significant overlap.

2.5 TEM Analysis

Nearly all of the TEM data were collected at 100 keV which is below all knock-on damage threshold energies, except one planar oxygen site (O2) when the electron beam is near the a, b, or c axes (Basu et al. 1989; Kirk et al. 1988; Kirsanov, Musin, and Shamarina 1994; Kirsanov, Musin, and Shamarina 1992). High-resolution electron microscopy (HREM) was performed on a Hitachi H-9000 at Northwestern University, while most of the conventional electron microscopy was performed at ANL with a Philips CM30. An Optronics P1000 densitometer was used to digitize the negatives to eight bits with a linear distribution of optical densities. The images were then processed with SEMPER 6 software on Apollo and Hewlett-Packard workstations. A Wiener filter was used to remove the shot noise from the images. This was done by estimating the noise in the power spectrum and removing it from the amplitude component of the Fourier transform (Marks 1996).

2.5.1 Strain Contrast TEM

Conventional TEM is a broad term that includes three powerful techniques, namely: bright-field imaging (BF), dark-field imaging (DF), and selected area diffraction (SAD). The manner in which each of these techniques was employed is described below.

In order to image the irradiation induced defect clusters or defect cascades (2-5 nm in size), weak dynamic two-beam dark-field imaging was performed, typically with the (200), (020), or (006) reflection. The term weak dynamic condition refers to a range of tilts between (**g**, 1.1**g**) and (**g**, 2**g**). For the (200) beam at 100 keV this translates into a range in the excitation error of $5x10^{-3}$ nm^{-1} to $5x10^{-2}$ nm^{-1}. Generally the excitation error should be greater than 0.2 nm^{-1} (in this case (**g**, 4**g**)) for weak beam imaging or highly kinematic conditions. The tilt orthogonal to **g** was usually 7-10° so that a systematic row of reflections along **g** was obtained. Tilts of only 3-5° resulted in several non-systematic reflections with strong intensities, while tilts greater than 10° started to enter other poles as well as create large parallax problems when relating specific areas of a dark-field image to other images obtained using another **g**, e.g., (200) vs. (020). The size of the objective aperture is important and usually the smallest aperture is too small. The aperture should be about 2-3 times the size of the imaging reflection when the illumination is set up for imaging. As a side note, the appearance in dark-field of small Moiré fringe patches (often only 2 short fringes) is a good indication that oxides are forming on the sample surface. This is the result of either a poor vacuum or a dirty surface.

Bright field imaging had very limited application in this work and was used only to observe twin boundaries and place the selected area (SA) aperture on a single twin lamella.

Electron diffraction had two primary uses in this work. The first was to simply locate crystals oriented near the pole of interest and align them to the desired orientation. The other use was to investigate the ordering of point defects by observing the extremely weak diffuse scattering. In order to take a picture of diffuse intensity that is 10^5-10^6 times less intense than the bulk reflections, one must spread the illumination out until the transmitted beam and few of the stronger reflections are just visible on the phosphorescent screen and then take a through exposure series, e.g., 30, 60, 120, 240, and 300 seconds. It is also important that the intermediate lens astigmatism is eliminated, the sample height is properly adjusted, and the objective lens is well focused in the SA mode.

2.5.2 Phase Contrast TEM

High resolution electron microscopy (HREM) is actually phase contrast imaging in which the objective aperture is removed from the beam (a very large aperture may also be used). This allows many beams to interfere and form the final image. The theory regarding electron sample interaction and the affect of both coherent and incoherent aberrations on the final image is well studied and is explained in several books. An attempt to explain these topics will not be made here and the reader is referred to several references (Buseck, Cowley, and Eyring 1988; Reimer 1993; Spence 1988).

The actual technique of HREM requires expertise in minimizing objective astigmatism, beam tilt, crystal tilt, and producing a clean, stable, thin crystal. Conventional HREM, in which the sample is oriented so that the electron beam is parallel to a major crystallographic axis, was used in this project. One could be concerned, however, that the undamaged crystal above and below a defect will obscure the defect's information in the final image. This is a common problem experienced by those who use HREM to image surface reconstructions (Xu et al. 1993). The method employed is to tilt the sample so that the bulk reflections in the diffraction pattern are diminished; thus, the information in the final image of the bulk crystal is also diminished. Defects can be imaged in this manner because the defect's reciprocal space extent is much greater than the bulk lattice's reciprocal space extent, this is due to the defect's small real space dimensions. This enhanced reciprocal space extent allows the defect to intercept the Ewald sphere over a greater range of tilt than the bulk reflections. The problem of using off-zone HREM lies in interpreting and simulating the image.

Note that at voltages above 150 keV there is a time constraint in observing a particular region due to an increase in the electron beam knock-on damage of a defect in YBCO and subsequent surface degradation. Dr. Kirk, while working at Oxford University, noted that in the JEOL 4000 EX at 400 keV some defects were present for only a few minutes before vanishing.

2.5.3 Energy Dispersive Spectroscopy

Energy dispersive x-ray spectroscopy (EDS) analysis was performed in both a Hitachi 570 SEM with a Tracor Northern EDS system and a Phillips

CM30 TEM with an EDAX EDS system. The SEM samples were either powder or single crystals and placed on a carbon stub; no conductive coating was applied. The TEM samples were crushed powder dispersed on a variety of TEM grids including Cu, Au, and Mo depending upon the elements being analyzed.

The concentration of Au in YBCO single crystals was determined semi-quantitatively by using the *k* factors built into the commercial program and allowing the program to calculate the Au concentration. A more rigorous approach was used to determine x in $Hg_{1-x}Cr_xBa_2CuO_{4+\delta}$. Specifically, the undoped compound, for which the structure and composition are known, was used to obtain the *k* factors. A thin film approximation was made and the Cliff-Lorimer equation (Cliff and Lorimer 1975) was used to determine the Hg stoichiometry in the Cr-doped compounds. The Cr stoichiometry is one minus the Hg stoichiometry, provided the site is fully occupied and contains only Cr and Hg atoms.

2.5.4 In-situ Stages

In this work two in-situ stages were used. A Gatan double-tilt heating stage was used to investigate the annealing of cluster defects in proton irradiated YBCO. A Gatan double-tilt liquid nitrogen stage was used to show that diffuse scattering in as-grown Au-doped YBCO was due to small point defect clusters and not thermal scattering of the electrons. Both stages were found to work well by not only reaching the desired temperature rapidly but the sample was also quickly free of drift.

2.6 *Magnetic Measurements*

Research on the magnetic properties of proton irradiated YBCO was performed at ANL by Dr. Viswanathan as a graduate student with Dr. Kirk. An important result of this research was that the defects have an anisotropic pinning force (Viswanathan et al. 1996), which may correspond to the defect's structural anisotropy.

Most of the YBCO single crystals used in this work had their T_C's measured, by Dr. Kostic, in a low-field SQUID magnetometer. The onset of superconductivity was typically over 90.5 K with a transition width of less than 1 K. The high T_C and narrow transition width indicate the crystals were optimally and homogeneously oxygenated.

2.7 *Image Simulations*

Simulations of the high resolution images and diffraction patterns were performed at Northwestern University on Apollo work stations using Northwestern University Multislice Image Simulation software (NUMIS). This software generates simulated images using non-linear imaging theory, provided the crystal structure and the microscope operating conditions are given.

The multislice algorithm requires the unit cell to be broken into slices (≈0.2 nm thick) and sequenced such that a thick crystal can be generated by repeating a sequence (or set of sequences) many times. A small defect may be sliced up and its sequence slipped in the bulk crystal sequence at the desired depth. The atomic potential of each slice is projected into a two-dimensional plane. The electrons interact or diffract off of each slice and the diffracted

beams are Fresnel propagated to the next slice or projected potential. After the final slice the exit wave is stored; this wave is then imaged for different microscope parameters.

The microscope parameters at the time of the exposure must be provided for meaningful simulations. The most important parameters needed are objective defocus and crystal thickness; therefore, most simulations are done for a large range of both defocus and thickness. Other parameters of importance are accelerating voltage, beam tilt, spherical aberration, astigmatism, crystal tilt, focal spread, and the incoherent convergence angle. The voltage is readily known and the astigmatism, beam tilt, and crystal tilt are minimized by the operator and must be near zero to easily interpret the images. The incoherent convergence angle is obtained from the diameter of the diffraction spots under the imaging illumination conditions. The spherical aberration (C_S) was measured by tilting the electron beam a known amount and recording the magnitude of the image displacement in the direction of the beam tilt. This technique is described by Spence (Spence 1988). The results for the Hitachi H-9000 at Northwestern University operated at 100 keV are provided in Fig. 2.3. A C_S of 1.75 mm was determined and used for the image simulations.

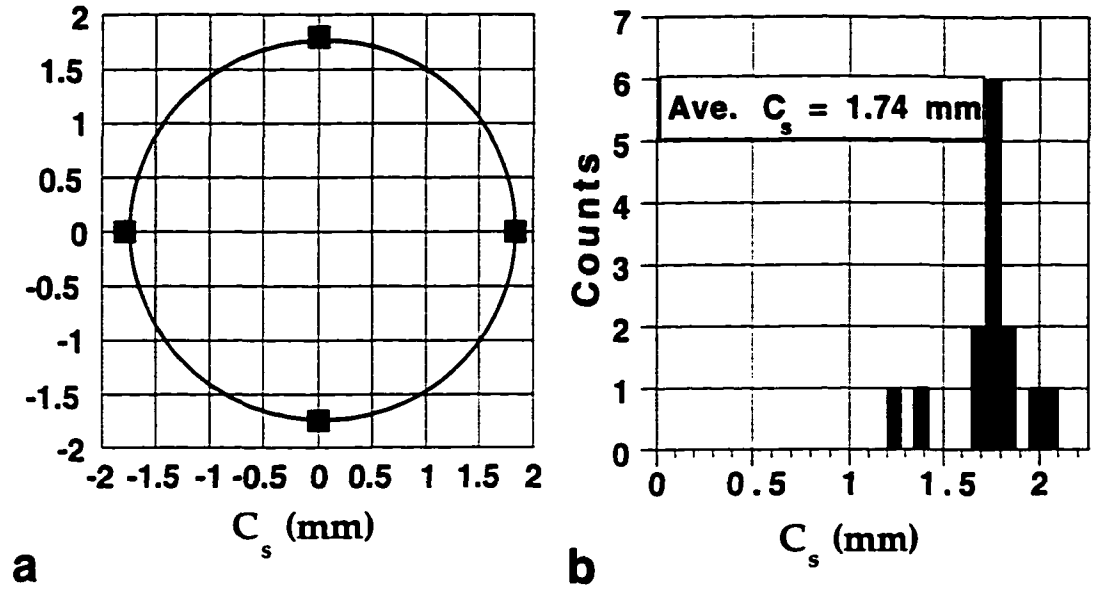

Figure 2.3 Results for the C_S calibration of the Hitachi H-9000 at Northwestern University operated at 100 keV. (a) plots four measurements made under the same microscope alignment with four orthogonal tilts. All four points lie on a circle of radius 1.75 mm with the center very near the origin. The radius equals the C_S and any offset of the circle's center from the origin is either the residual beam tilt from an imperfect alignment or the tilt due to the misalignment of the upper and lower pole pieces. (b) plots all of the measurements made and the average C_S is 1.74 mm.

2.8 Matching Experiment with Simulation

No attempt to quantitatively match the image simulations with experimental images was made. There seems to be no straightforward manner to match image simulations of point defect models with experiment, the random nature of these defects precludes a direct match between the simulation and the real image. Instead a rigorous best-fit by the eye approach was used, and is outlined below.

A spot in the power spectrum corresponding to a known spacing in the experimental image was used to accurately calibrate the nanometers per

pixel. The experimental image was then rescaled so that it matched the magnification of the simulation, typically 0.025 nm per pixel.

The mean intensity, calculated from a region of the experimental image of the same size as the simulated image, was multiplied by the simulated image, which originally had a mean intensity of one. This resulted in the simulated image having the same mean as the local area of the experimental image into which it was pasted.

The effect of vibration is very important in trying to match simulated and experimental images. A convolution of the simulated image and a Gaussian peak was performed to model a small isotropic vibration, e.g., 0.05 to 0.1 nm. This convolution does not affect the mean intensity but definitely alters the minimum and maximum values, i.e., the contrast. It also removes high frequencies in the image and brings out previously invisible defects. A small vibration must be modeled, but with great care.

Finally, an exact position must be found into which the simulation is to be pasted. This was obtained by performing a cross correlation of the simulated image with the local area of the experimental image. If all has been done properly and the model is correct, the inserted simulation should not be easily discerned in the experimental image. This blending of the simulation was the primary criteria for a best-fit by the eye.

Chapter 3 | Point Defects in As-Grown $YBa_2Cu_3O_{6.9}$ Single Crystals

3.1 Introduction

A great deal of attention has been directed towards determining the native defect structures present in YBCO, most of which has been concerned with the long range ordering in highly O deficient samples [theoretical predictions (de Fontaine, Ceder, and Asta 1990) and experimental evidence (Beyers et al. 1989; Werder et al. 1988)]. Little has been done, however, to determine the structure of O vacancy and cation impurity clusters or the role of such defects as weak magnetic flux pinning centers in crystals near full oxygenation. Reyes-Gasga did observe weak diffuse streaks in electron diffraction patterns from sintered samples near full oxygenation and proposed a 2-4 O vacancy clustering model (Reyes-Gasga et al. 1989). Unfortunately there was no discussion of possible cation impurities, and there were no simulations of the proposed defect model.

A large portion of impurities in single crystals results from the environment in which they are grown. A common method for growing YBCO single crystals is the self-flux method in Au crucibles (Kaiser et al. 1987). Neutron and x-ray diffraction experiments show that at elevated temperatures Au exclusively substitutes for Cu(1) in the CuO chain plane up to 3 wt. % (10 at. % per formula unit), after which Au precipitates begin to form (Cieplak et al. 1990). Neutron activation analysis on crystals grown at ANL revealed Au concentrations to be typically 2.5 wt. % (Frischherz 1993).

There are two main advantages to growing YBCO in Au crucibles: an increase in T_C of ≈ 1 K and larger crystals (Cava et al. 1990). Thus a lot of attention was given to Au-doped materials as all other cation doping leads to a decrease in T_C. Most of this attention, however, was directed towards the unit cell distortion and to the valence variation of Au and Cu as a function of O content (Eibschütz et al. 1993).

This chapter provides a comparison of HREM images and diffraction patterns of YBCO with corresponding simulations for several point defect cluster models. The best model has randomly distributed rod like defects consisting of Au^+ and O vacancies along [010] and Au^{3+} and O interstitials along [100]. Other point defect cluster models are presented and shown to be inadequate. The existence of these defects is supported by magnetic flux pinning data which reported a higher critical current in Au-doped YBCO crystals than in pure YBCO (Viswanathan et al. 1996). This implies a magnetic flux pinning site which maybe related to the presence of Au; I will return to this later.

3.2 Evidence for Point Defect Clustering

Single crystals of YBCO were grown in Au crucibles at ANL as described in 2.1.1 and TEM samples were prepared by crushing in methanol, see 2.2.1. A low-field SQUID magnetometer was used to determine T_C values, which were over 90.5 K with a transition width of less than 1 K. EDS analysis, performed in both a SEM and TEM, verified a 2.5 wt. % Au content which agrees with the results from neutron activation.

The first evidence I obtained for defect clustering in Au-doped YBCO was diffuse streaks in long exposure electron diffraction patterns. Figures 3.1(a) and (b) are [001] zone axis diffraction patterns from the same area of a region without twin boundaries at room temperature and 88 K respectively. Extremely weak diffuse streaks of intensity along the [100] and [010] directions are evident. The streaks persist at low temperatures thereby eliminating thermal diffuse scattering as their source. These diffraction patterns are from an untwinned region; hence, the defects must lie along both the [100] and [010] directions. The streaks are also maintained upon tilting the crystal 7° off the [001] zone axis as shown in Fig. 3.1(c), therefore, they must be thick walls of diffuse intensity in reciprocal space resulting from short rod-like defects in real space. An intensity profile along the straight line indicated in Fig. 3.1(c) clearly shows the presence of the aforementioned streaks.

A typical high resolution image, see for instance Fig. 3.2, shows a very local aperiodic variation in intensity that would not be seen in an image of a perfect crystalline material. Figure 3.2 was taken approximately 50 nm from the edge of the sample, therefore, the intensity variation is not due to a high ratio of amorphous carbon to sample thickness. This variation in intensity was used to match against the simulated images of different point defect cluster models. These models, presented in 3.3, assume the defects are randomly positioned and are of a high enough density such that they will overlap in the image; consequently, individual defects cannot be discerned.

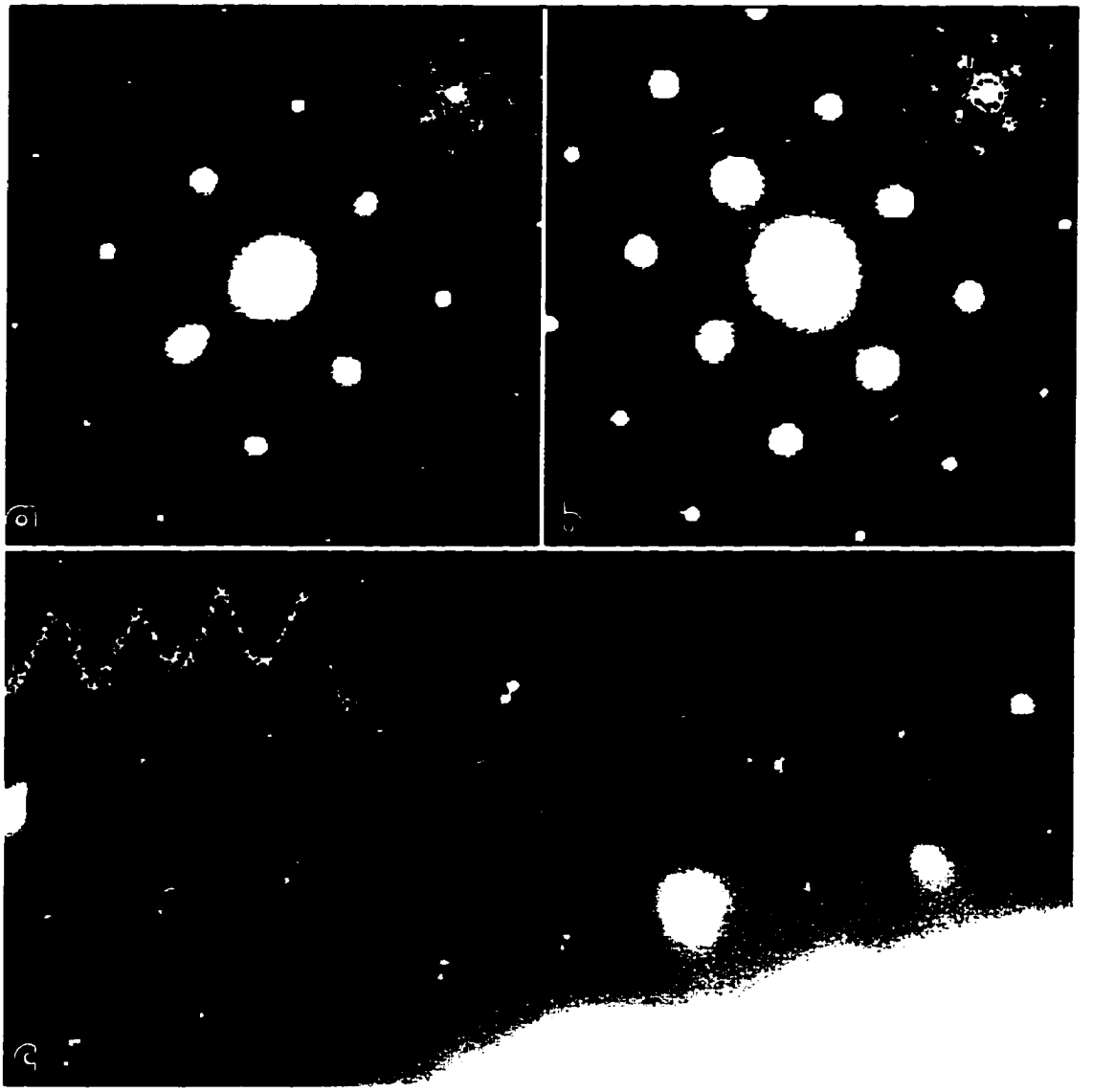

Figure 3.1 Electron diffraction patterns down the [001] axis from the same area of a single twin lamella: (a) room temperature (b) 88 K. There are diffuse streaks along [010] and [100] at both temperatures. The insets show constant intensity contour plots. (c) is of a different region taken at room temperature and is tilted approximately 8° from the [001] axis. Note that the diffuse streaks persist at large tilts indicting a diffuse wall of intensity in reciprocal space. The inset shows the intensity profile along the line in the figure.

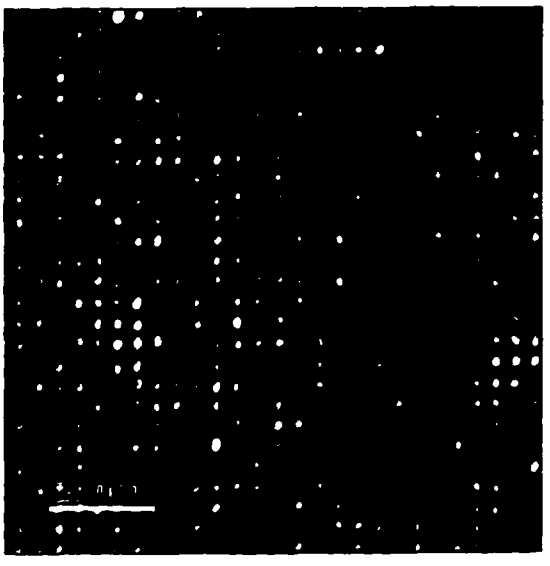

Figure 3.2 HREM image of $YBa_2Cu_3O_{6.9}$ down the [001] zone axis. Observe the non-uniform variation in intensity over very short ranges. This variation would not be present in a prefect crystalline material.

3.3 Defect Models and Image Simulations

Many different types of defects were modeled and simulated for comparison with the experimental images and diffraction patterns. The defects were randomly distributed in an 8x8x12 array of unit cells with a thickness of 14 nm or twelve unit cells along [001]. An x-ray diffraction study indicated that Au substitutes exclusively on the Cu(1) site (Cieplak et al. 1990), as such, defects were restricted to the CuO chain plane. Figure 3.3 shows one of the twelve different CuO chain planes for each of the five models presented. In describing the defect models, the nomenclature for atom sites in the YBCO unit cell given by Jorgensen et al. is used, see Fig. 1.1. Several assumptions were made in the defect models: O vacancies were on the O(1) chain site, Au substituted for the Cu(1) chain position, Au concentration was 3% of the total Cu or 1 Au/11 unit cells, and the O vacancy concentration was 1 vacancy/10 unit cells, i.e., x = 0.1.

The defect models primarily consider small rod-like defects and not square or triangular shaped defect clusters. This is based on the Fourier transform of a 2-D projection of defects randomly positioned in 3-D. The number of defects per unit area in a 2-D projection is simply a function of the thickness along the projected direction and the defect density. By combining a defect size of a few unit cells, based on the width of the diffuse streaks in the electron diffraction patterns, and an O stoichiometry of x = 0.1, an appropriate defect density can be calculated. Defects of intensity value equal to one were randomly added to an image of an original value equal to zero and portions of defects that overlapped were summed. After the

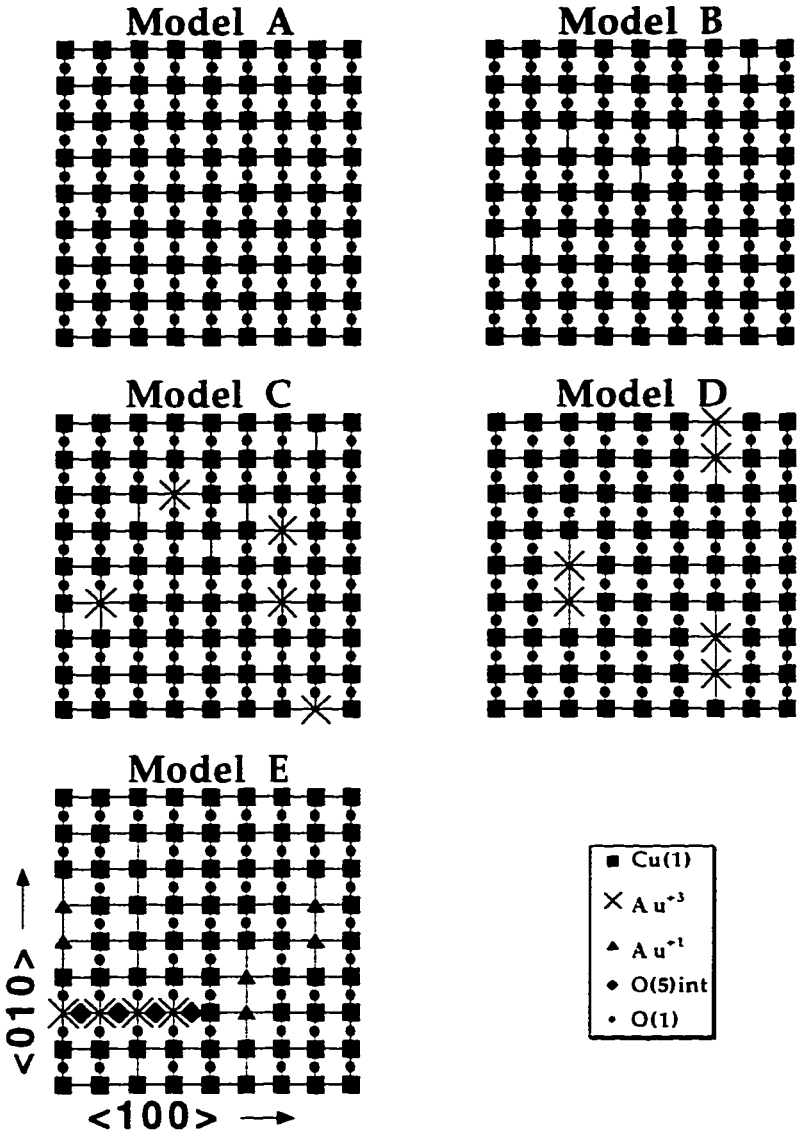

Figure 3.3 Array of 8x8 unit cells showing one of the 12 CuO chain planes used for each of the five models presented. The defects are randomly distributed in three dimensions and thus the stoichiometry is determined over all 12 layers and not by the single planes shown.

correct number of defects had been generated, a Fourier transform was performed. A variety of defect shapes and orientations were attempted and the Fourier transform results are as follows: point defects yielded a homogenous diffuse background, small square defect clusters yielded decaying Bessel functions perpendicular to the defect edges, and rod-like defects gave weak streaks similar to those in the diffraction patterns. It is based upon this analysis that a rod-like shape was chosen for the defect modeling.

As mentioned, five simulated models are provided for comparison with the experimental images. Model A represents a fully oxygenated defect free YBCO crystal and shows the perfectly repetitive nature of the image intensity. Model B has random single O vacancies and no Au, while Model C takes the same O vacancies as in model B and randomly substitutes Au on the Cu(1) site. Models B and C represent widely accepted models of YBCO. Model D combines Au and O vacancies into short rods along the [010] direction.

Model E, found to fit the experimental data best, combines three types of defects. The main feature is Au rods along the [010] and [100] directions. The association of Au with O vacancies or O interstitials is based on the need to balance the local charge. According to Eibschütz, Au is completely trivalent in a fully oxygenated sample and completely monovalent in samples where $x = 1$, with a portion of each state intermediate (Eibschütz et al. 1993). They reported that for $x = 0.1$ there should be approximately 60% Au^{3+} and 40% Au^{+}. It was also stated that Au^{3+} attracts O into the structure due to the combination of the higher charge of Au^{3+} compared with Cu^{2+}

and the similar radius of Au^{3+} compared to Cu^{2+} (0.073 and 0.085 nm respectively). Thus an O interstitial may preferentially sit next to an Au^{3+}, while O vacancies would tend to sit next to the much larger (radius 0.137 nm) Au^{+}. This led to a model of trivalent Au sharing O interstitials in the normally vacant O(5) site and monovalent Au sharing O vacancies in the O(1) site.

The samples analyzed had a thin coverage of amorphous material; consequently, the possibility that this contamination was the reason for the intensity variation in the HREM images had to be tested. The width of the amorphous material at the sample's edge was approximately 3 nm, therefore three thicknesses: 0.78, 1.95, and 3.9 nm of amorphous carbon were added to the top and bottom surfaces of the simulations of models A, C, and E. Following a technique by Paciornik et al., carbon atoms were positioned randomly in 0.385 nm boxes with the only restriction that no two carbon atoms could be closer than the carbon atom's diameter (Paciornik, Kilaas, and Dahmen 1993) .

The objective defocus, required for image simulations, was determined from power spectra of the sample's small amorphous edge. The defocus step was determined by plotting the defocus as determined by the power spectra vs. the negative number, see Fig. 3.4. Note that the slope (defocus step) is 19.5 nm, which is in excellent agreement with the nominal defocus step of 20 nm. The other microscope parameters used were: C_S = 1.75 mm (see 2.7), convergence = 1.5 mRad, energy spread = 8 nm, isotropic vibration ≈ 0.1 nm, and an electron energy of 100 keV. Multislice simulations were performed on Apollo workstations using NUMIS

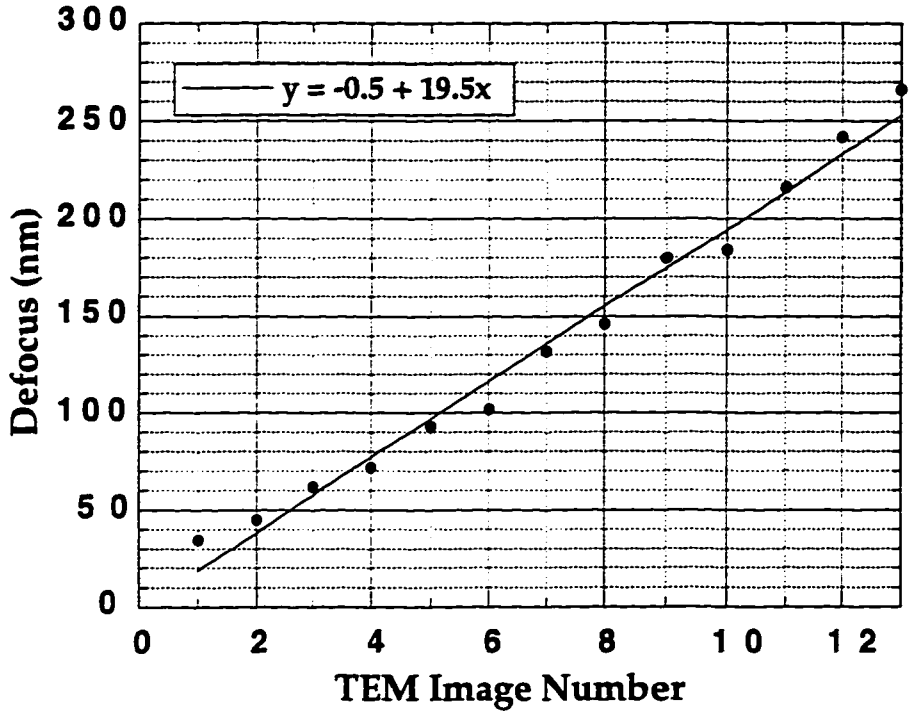

Figure 3.4 Plot of the objective defocus as determined from power spectra vs. the TEM image number. The nominal defocus step was 20 nm and the slope of the line is 19.5 nm which is an excellent agreement. Note that the defocus presented here is an under defocus, i.e., Scherzer defocus is positive in this format.

Software and the simulated images were pasted onto the experimental images using SEMPER software, see 2.8 for further details.

3.4 Comparison of Simulation with Experiment

Three members of a through focal series, Figs. 3.5 to 3.7, are presented as I feel that at least this many are required to match experimental to simulated images. Multislice image simulations of the five models (A-E) are inserted into each experimental image. Note that models A, C, and E are simulated with: 0, 0.78, 1.95, and 3.9 nm of amorphous carbon added to the top and bottom surfaces.

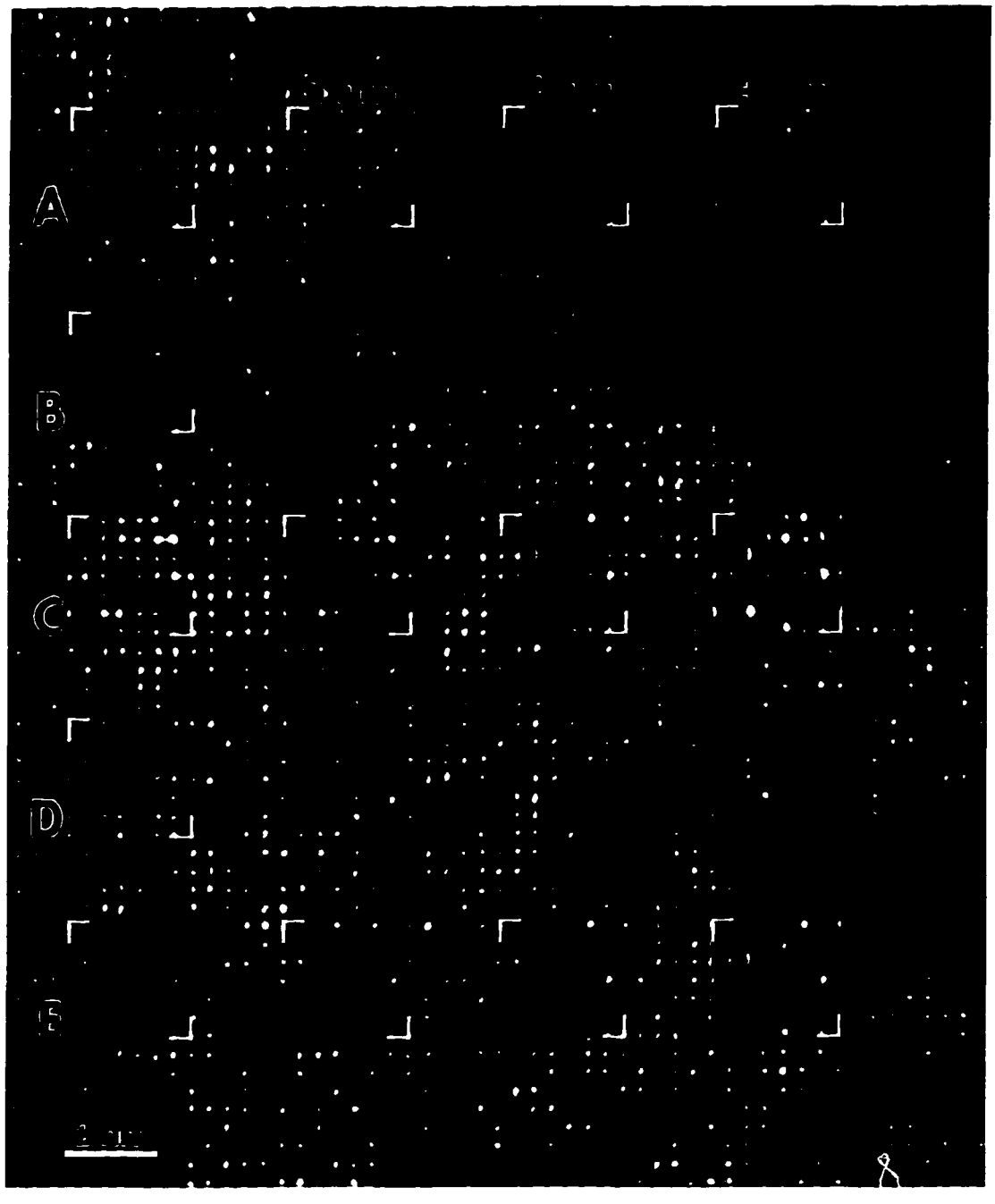

Figure 3.5 HREM image (100 nm underfocus) down the [001] zone axis with simulations of defect models A-E inserted. Models A, C and E have four simulations in row representing: 0, 1, 2, and 4 nm of amorphous carbon added to the top and bottom surfaces of the simulated material. Note the directionality of the dark streaks in the simulation of model D, this is not found experimentally.

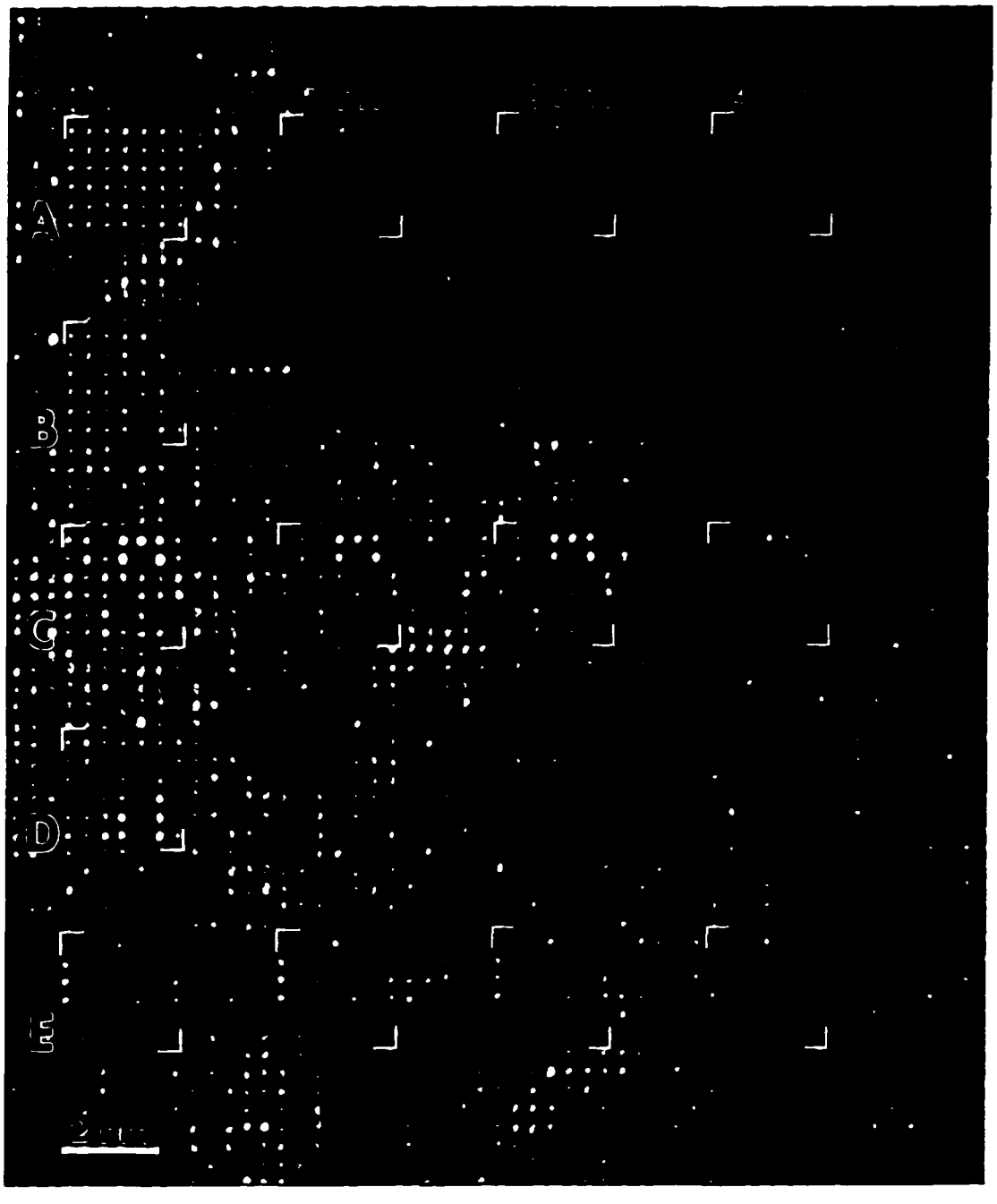

Figure 3.6 HREM image (132 nm underfocus) down the [001] zone axis with simulations of defect models A-E inserted. Models A, C and E have amorphous carbon added to the top and bottom surfaces as explained in the caption for Fig. 3.5.

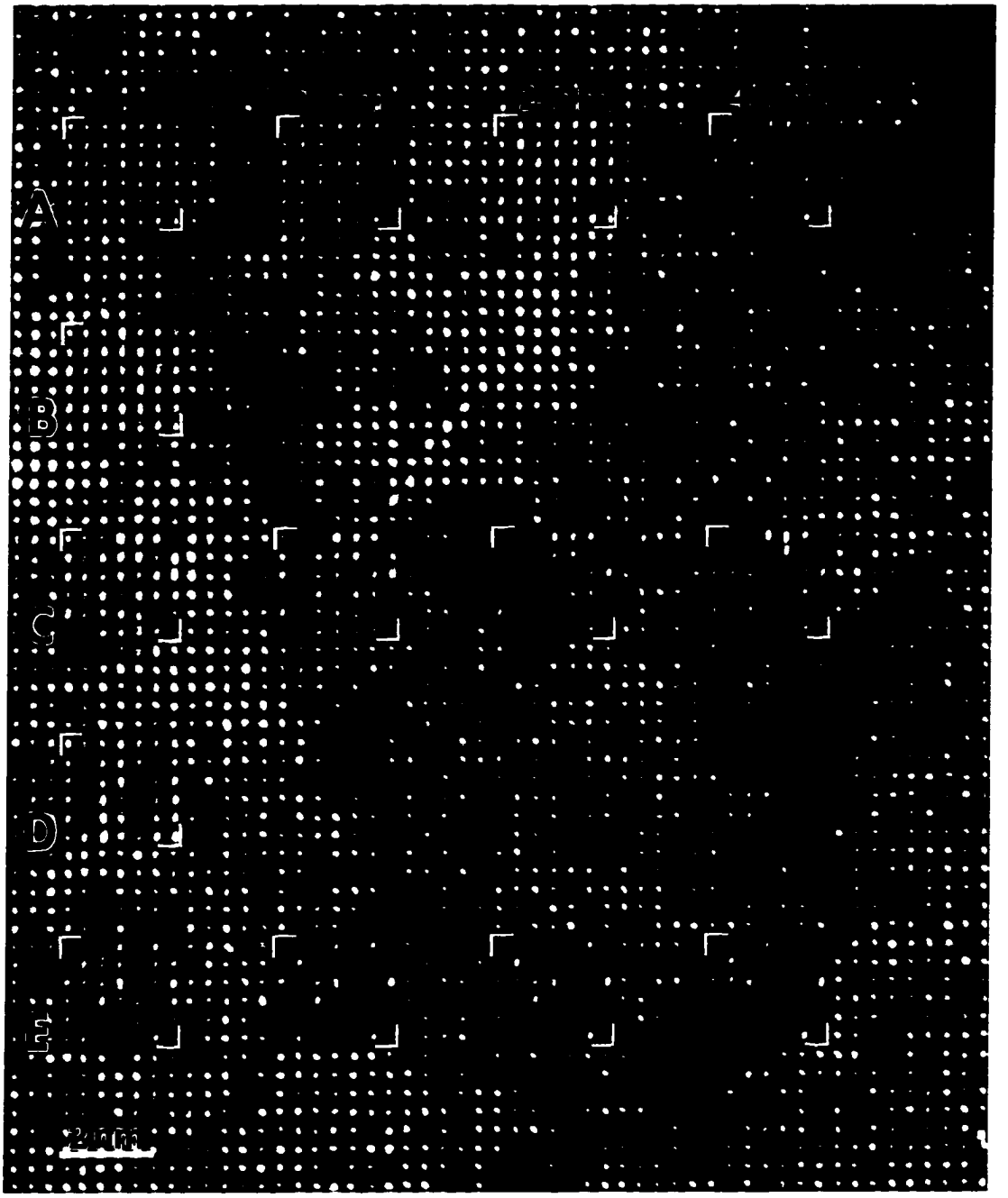

Figure 3.7 HREM image (214 nm underfocus) down the <001> zone axis with simulations of defect models A-E inserted. Models A, C, and E have amorphous carbon added to the top and bottom surfaces as explained in the caption for Fig. 3.5. Note that with increasing amorphous carbon there is an increasingly evident periodic dark contrast not seen in the experimental image.

The top row (model A) of simulations is of the fully oxygenated Au free model and shows the uniform contrast variation in a perfect crystal with no amorphous coating. This model does show some variation in the contrast similar to that seen in the experimental image as an increasing amount (left to right) of carbon is added. To generate a comparable intensity variation at least 2 nm of carbon is required; this amount of carbon starts to introduce systematic contrast variations in the image that do not match the experimental image at certain defoci, see for instance Fig. 3.7. Therefore, carbon alone cannot explain the contrast variation.

The second row (model B) represents random single O vacancies and still no Au doping. This simulation also fails to generate the required contrast variation. Although a reasonable match was never achieved, many attempts were made to simulate the contrast variation observed by using O vacancy clusters of different size and shape. It is understandable that the simulations of models based solely on oxygen vacancy defects do not fit the experimental images, as the EDS analysis showed a consistent presence of ≈2.5 wt. % Au. Therefore, as Au has a much higher scattering factor for electrons than Cu, any proper model must include Au.

The bottom three rows of simulations in Figs. 3.5 to 3.7 represent defect models C-E and each combines O defects and Au atoms. All defect models containing Au produced a significant variation in contrast. Many of these models, however, generated a directional contrast variation that did not match the experimental images as evidenced by the simulation in the fourth row (model D). This model had defect rods only along [010]; thus, the intensity tends to vary along [100] differently than along [010]. Simulations

in the third row (model C) represent single O vacancies not associated with the single Au atoms and fit the experimental images reasonably well. However, as shown in the diffraction simulations, Figs. 3.8(a) and (b), model C does not generate the diffuse streaking. The fifth row (model E) best fits both the images and the diffraction patterns. Notice the image simulations of models C and E do not require carbon contamination layers to obtain a good fit.

Diffraction pattern simulations, Figs. 3.8(a) and (b), are needed to distinguish whether model C or E is correct. It is important to realize that the mean level of each pattern is the same. The pattern for model C shows a homogeneous spread in the diffuse intensity while the simulation for model E has the required streaks along both the [100] and [010]. The diffuse intensity in the simulated streaks is 5-6 orders of magnitude less than the bulk reflections, and this explains the very weak intensity in the experimental electron diffraction patterns. Electron diffraction patterns were simulated for the other models including many not presented here; diffraction simulations of models containing rods of O vacancies without any Au did produce the required diffuse streaks. The diffuse intensity of these streaks was 7-8 orders of magnitude less than the bulk reflections and is probably too weak to obtain in an experimental electron diffraction pattern.

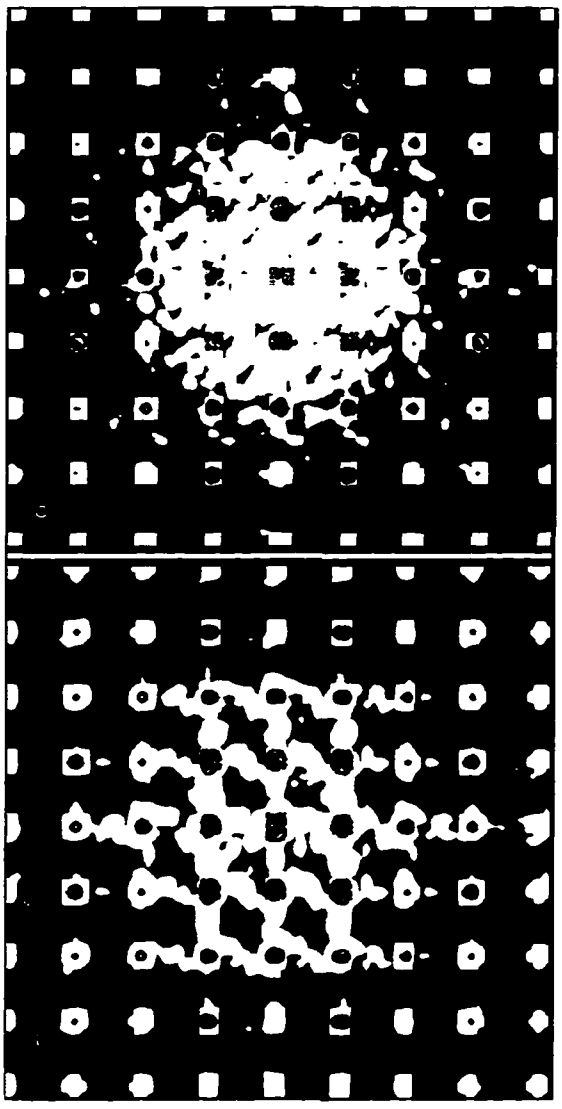

Figure 3.8 Simulated electron micro-diffraction patterns for (a) Model C and (b) Model E. Note that the diffuse intensity is homogenous in Model C but is streaked in Model E. By comparing these streaks to those in the experimental diffraction patterns shown in Fig. 1(c) it is evident that model E remains plausible while model C fails.

3.5 Discussion

The use of TEM to investigate the nature of point defect clusters has been mostly ignored. Multislice simulations, however, show that random clusters, of sufficient density and scattering power, should be observable in both HREM images and diffraction patterns. Regrettably, this technique of combining HREM and electron diffraction cannot reliably discriminate between model E and a similar model (not presented) in which the O interstitials on the O(5) site between Au^{3+} are removed. The later model would then have short Au rods along both [100] and [010] without any O between the Au atoms. The reason for including O defects in the Au rods is for local charge balance. As mentioned previously, Eibschütz et al. reported the presence of Au^{3+} and Au^{+} on Cu^{2+} sites with a Au^{3+}:Au^{+} dependence on O concentration. With Au^{+} being much larger and more negative than Cu^{2+}, it stands to reason that an O vacancy may sit next to Au^{+}; similarly, Au^{3+} is about the same size and is more positive than Cu^{2+} and an O interstitial may sit next to Au^{3+}.

The defects proposed here must be considered as possible flux pinning sites in as-grown Au-doped YBCO, even though they lie in the CuO chain plane and not the CuO_2 plane. This is supported by the work of Viswanathan et al. which compared crystals grown in Au versus ZrO_2 crucibles (Viswanathan et al. 1996). They showed a flux pinning difference suggesting the existence of as-grown defects in the Au-doped YBCO crystals. The ZrO_2 grown crystals are almost free of cation doping as Zr is much less invasive in YBCO than Au, and had consistently lower critical currents as a result of fewer flux pinning defects. In this study, they irradiated the crystals

with 3.5 MeV protons to a fluence of $1x10^{16}$ $H^{+}\cdot cm^{-2}$ and found that the Au-doped crystals then had the lower critical currents. These results can be explained by an as-grown defect acting prior to irradiation as a flux pinning center and during irradiation to prohibit the formation of larger irradiation defects by inhibiting the coalescence of the irradiation damage induced point defects.

3.6 Conclusion

The combination of careful diffraction analysis, high resolution imaging, and multislice image simulations allows the investigation of randomly distributed small clusters of point defects. This holds true even for clusters dispersed in a heavy cation matrix, and in the case of YBCO single crystals grown in Au crucibles yields a model for the clustering of Au substituted for Cu(1) and O point defects into 1 nm rods in the CuO chain plane. Oxygen interstitials, O(5) site, combine with Au^{3+} along the [100], while O vacancies combine with Au^{+} along the [010].

The defects proposed here are possible flux pinning sites in as-grown Au-doped YBCO crystals. It would be of interest to investigate the flux pinning dependence on variable Au doping of YBCO crystals grown in ZrO_2 crucibles. This would solidify the hypothesis that the Au is responsible for the flux pinning. Chapter 7 contains further details regarding this possible future work.

The advantages of YBCO grown in Au crucibles are increased crystal size, higher T_c, and improved flux pinning. These benefits must be balanced against the knowledge that the Au does form O related defects and does not

remain inert in the system. Therefore, research on the basic properties of YBCO should not be performed on Au-doped YBCO unless it is certain that the effects of Au can be taken into account.

Chapter 4 | Structural Features of Defect Cascades in $YBa_2Cu_3O_{7-x}$

4.1 Introduction

As discussed in Chap. 2 defects which are on the size scale of 2ξ (3-5 nm in the a-b plane for YBCO) are optimal for enhancing J_C. This chapter investigates irradiation induced defect cascades which are in this size regime. A defect cascade in YBCO is produced when the bombarding particle rapidly dissipates a lot of energy thereby creating a thermal spike, locally melting a small spherical volume inside the crystal. This melt typically quenches into a highly disordered or even an amorphous state. In high-T_C superconductors a defect cascade has a much lower superconducting order parameter, indeed it is usually an insulator, and is of the optimum size to be a highly effective magnetic flux pinning site. Given that neutron irradiation of YBCO primarily results in defect cascades and neutrons have a large penetration depth in YBCO, this provides a method of significantly enhancing J_C in large single crystals.

Intragrain flux pinning measurements made on fast neutron irradiated YBCO ceramics for both the 60 and 90 K T_C phases ($x = 0.4$ and $x = 0.1$ respectively) revealed a difference in J_C enhancement between these phases (Wisniewski et al. 1994). The natural question this difference raises involves the defect cascade size distribution in each phase. An assumption that the defect cascade size was larger in the more oxygen deficient phase (60 K T_C) was coupled with the differences in ξ between the two phases and with

the differences in ξ at different measuring temperatures to explain the flux pinning data. This assumption of cascade size differences was based on theoretical work involving low energy ion recoils in YBCO (Kirsanov, Musin, and Wisniewski 1993).

The previously mentioned theoretical work involved molecular dynamic calculations for 100-300 eV O, Cu, Y, and Ba ion damage in $YBa_2Cu_3O_{7-x}$ predict an increase in defect cascade size with decreasing oxygen concentration (Kirsanov et al. 1993). Oxygen stoichiometries: $x = 0$, 0.5, and 1.0 were studied and average defect cascade sizes of 2.7, 3.8, and 6.0 nm were calculated respectively. This size variation was attributed to oxygen atoms acting as a viscous medium to reduce the lengths of replacement collision sequences. It was proposed that the smaller cascades with more localized damage, produced in the crystals with a higher oxygen concentration, are more effective pinning centers.

While many types of irradiation have been attempted in hopes of enhancing Jc, the size and density of the defects created are always of interest. One of the most promising forms of irradiation is high-energy heavy-ions which create tracks of damage. Direct size measurements, using HREM, of amorphous tracks resulting from 300 MeV Au^{+24} irradiation show a size anisotropy in YBCO (Zhu et al. 1993). The cross section of the tracks along the c-axis is smaller than that of tracks along the a-axis. Also the tracks along the c-axis are circular while the tracks along the a-axis are elliptical with the major axis along the [010] direction. This was explained to the first approximation by a thermal spike model coupled with the anisotropy of the thermal conductivity in YBCO (Hagen, Wang, and Ong 1989; Shao-Chun et

al. 1991). The aspect ratio, however, was 1.6 for the a- to c-axis dimensions; this is much less than the ratio of 3-5 predicted by the thermal conductivity anisotropy. While this chapter addresses defect cascades and not tracks, there are some useful conclusions that can be made by comparing track damage with defect cascade damage (I will return to this later).

A thorough TEM study of the defect cascade microstructure resulting from 50 and 85 keV Kr^+ and Xe^+ irradiation in the 90 K phase (x=0.1) of YBCO has been reported (Frischherz et al. 1993). It was found that the defect cascades produced had a cross section approximately 3.5 nm in diameter. Recrystallization of cascades was suggested due to a 50% yield of defect cascades per incident ion and apparent lattice fringes in the center of a HREM image of a defect cascade (lattice fringes were found in 3 of 5 cascades observed). This study did not evaluate the size distribution of defect cascades in YBCO as a function of oxygen stoichiometry.

This chapter addresses the size distribution, shape, and structure of 50 keV Kr^+ irradiation induced defect cascades as a function of oxygen stoichiometry. $YBa_2Cu_3O_{7-x}$ single crystals of varying oxygen stoichiometry were irradiated with 50 keV Kr^+ to create defect cascades similar to those resulting from fast neutron irradiation.

4.2. Experimental Details

Optimally oxygenated single crystals of YBCO were grown in Au crucibles according to the procedure outlined in 2.1.1. Several crystals were reoxygenated to obtain a range of oxygen concentrations. To determine the values of T_c, magnetization measurements against temperature were made

using a low-field superconducting quantum interference device (SQUID). The data, Fig. 4.1, show very sharp transitions, typically less than 2 K, which indicate single phase crystals with near uniform oxygen stoichiometry. A relationship between T_c and oxygen stoichiometry has been established (Jorgensen et al. 1990) and the four values of x are: 0.1, 0.3, 0.45, and ≈ 0.65. It is very difficult to obtain a sharp transition in the $x \approx 0.65$ sample; hence, the oxygen content in this sample is a rough estimate.

The details for TEM sample preparation and Kr^+ irradiation are provided in 2.2 and 2.4 respectively. To avoid confusion the following notation for ion direction and size measurement direction will be used: ion direction will be near the a, b, or c axis and size measurements will be $[010]_a$, $[001]_a$, $[010]_c$, and $[100]_c$, where the subscript indicates the incident ion direction. In this notation the b-axis or [010] is coincident with the CuO chains and the c-axis or [001] is in the long (1.185 nm) unit cell dimension

4.3. Experimental Results

4.3.1 Defect Cascade Size

Dark-field imaging in weak dynamic conditions, usually (**g**, 1.25 **g**), was used to image the Kr^+ defect cascades, see for instance Fig. 4.2. The (200), (020), and (006) reflections from the a and c zone axes were used for DF imaging, enabling size measurements in the $[100]_c$, $[010]_c$, $[010]_a$, and $[001]_a$ directions. The defect cascade size was measured by viewing digitized dark-field negatives at a magnification of 1.5 million (this magnification was determined by knowing that a pixel on the computer monitor was equal to

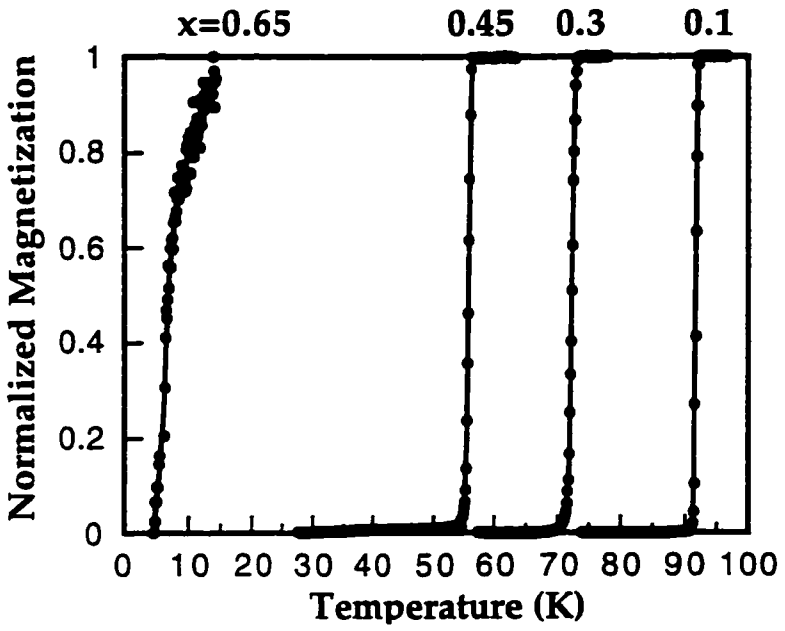

Figure 4.1 Low-field DC SQUID magnetization curves of the four $YBa_2Cu_3O_{7-x}$ single crystals used in this chapter. The transition temperature is determined by the average oxygen deficiency, indicated above each curve.

0.15 nm and simply placing a ruler on the monitor to obtain the number of pixels·cm^{-1}). This magnification is reported here only to provide reader with sense of the procedure, and it important to realize that the size was measured by counting the number of pixels across a defect. The line of no contrast (black/white interface) was taken as the diameter for cascades showing black/white contrast (Ashby and Brown 1963); while the width perpendicular to **g** was measured for cascades showing black dot contrast (Wilkens 1970). The length of the black/white interface is only weakly dependent on the deviation from the exact Bragg condition (Saldin, Stathopoulos, and Whelan 1979). Simultaneous 95% confidence intervals were generated according to Scheffé's procedure to determine any trends present, see Table 4.1. Except for the larger $[010]_a$ size measured with the (006) reflection, the means all lie

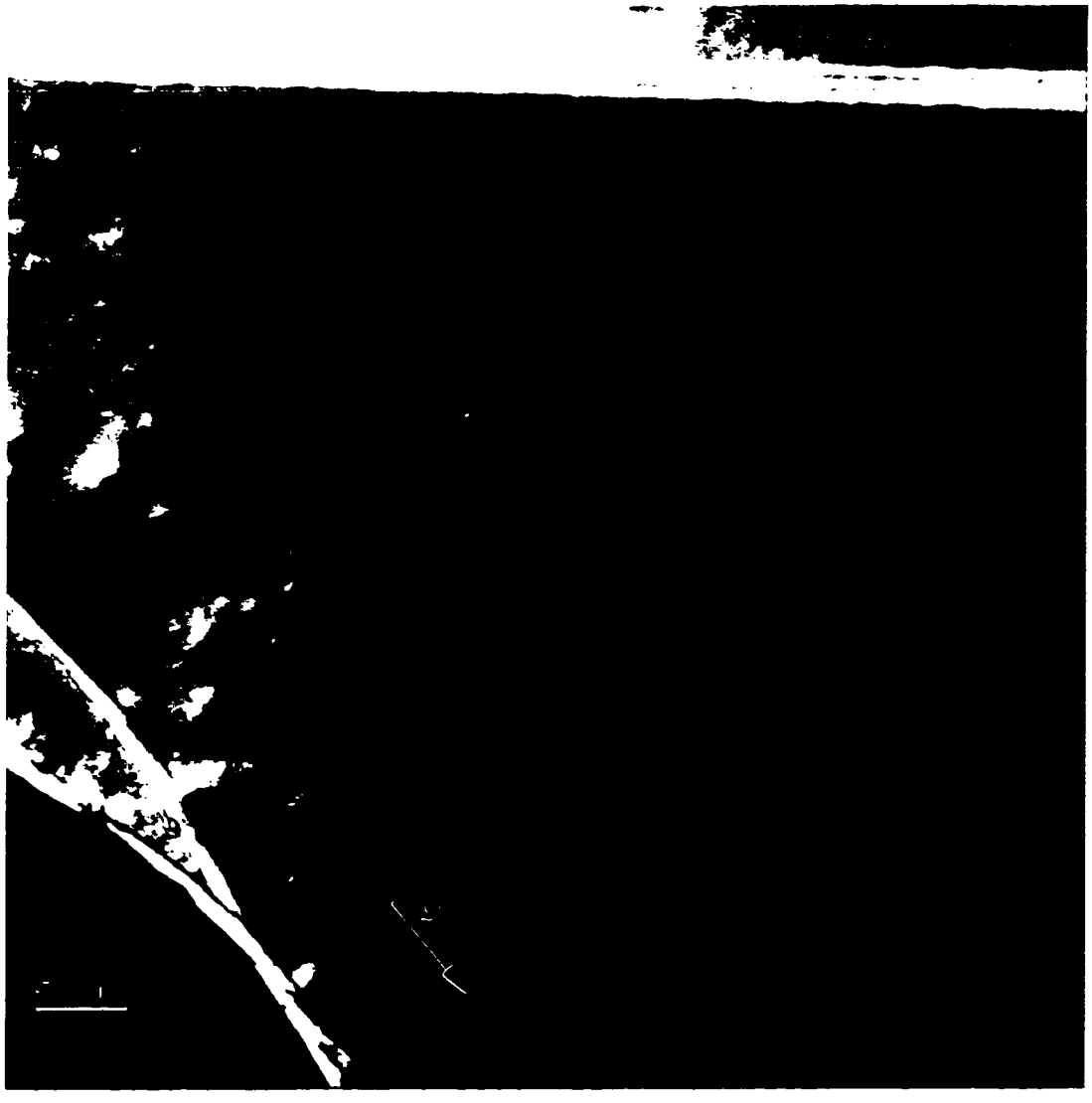

Figure 4.2 Typical dark-field TEM image showing defect cascades produced by 50 keV Kr^+ in YBCO. The defect cascades are imaged as either black/white contrast parallel to **g** or as black dot features. The length of the black/white interface or the diameter of the black dot is equal to the cascade diameter.

within 0.8 nm. A difference of at least 0.2 nm between any two means is statistically significant at the 95% confidence level. Note the $[010]_a$ size was measured only for the x = 0.1 sample and its mean size was much greater than the other sizes.

When plotted, Fig. 4.3, the data for x = 0.1 show the size distribution in all three directions for the two zone axes studied (one direction is common to both zone axes). The defect cascades produced from ions incident near the c-axis have a circular cross section, while an elliptical cross section was found for ions incident near the a-axis. The plots in Fig. 4.4 show the $[010]_c$ size distribution in each of the four oxygen stoichiometries studied and demonstrate that the defect cascade size is independent of oxygen content. Similarly, the size distributions for $[100]_c$ and $[001]_a$, not shown, have the same overall shape and mean as those in Fig. 4.4. As each defect size measurement was made, a record was kept as to whether the defect showed black/white or black dot contrast. The combined data for all size directions and oxygen stoichiometries, excluding the larger $[010]_a$ data, for the black/white and black dot contrast is shown in Fig. 4.5. The overall shape of the distributions is nearly identical and the shift in peaks is small (0.3 nm); therefore, defects showing either black/white or black dot contrast were sized to improve the statistics.

Table 4.1 Statistics for the defect cascade size distribution in $YBa_2Cu_3O_{7-x}$ resulting from 50 keV Kr^+ irradiation. The subscript on the Miller indices for the size direction indicates the approximate direction of the incident ions.

Oxygen Content	Size Direction	Counts	Mean (nm)	Std. Error (nm)
6.35	$[100]_c$	132	3.75	0.11
6.35	$[010]_c$	154	3.98	0.14
6.35	$[001]_a$	188	3.80	0.09
6.55	$[100]_c$	112	3.32	0.09
6.55	$[010]_c$	129	3.72	0.11
6.55	$[001]_a$	99	3.66	0.10
6.7	$[100]_c$	56	3.12	0.12
6.7	$[010]_c$	62	3.16	0.15
6.7	$[001]_a$	100	3.28	0.09
6.9	$[100]_c$	192	3.26	0.09
6.9	$[010]_c$	183	3.67	0.10
6.9	[001]a	103	3.77	0.11
6.9	$[010]_a$	160	5.26	0.12

A HREM image of a typical defect cascade is shown in Fig. 4.6. Other defects were located near the thin edge and also were found to have diameters between 2.5 and 4 nm. This is consistent with the data obtained from the dark-field measurements. The defocus of the image in Fig. 4.6 is approximately -140 nm, as determined from the power spectrum taken from the sample's amorphous edge. It is important to be aware of the effect of image delocalization and to take images at the overlap defoci so that image interpretation is intuitive. Refer to appendix A for a further discussion.

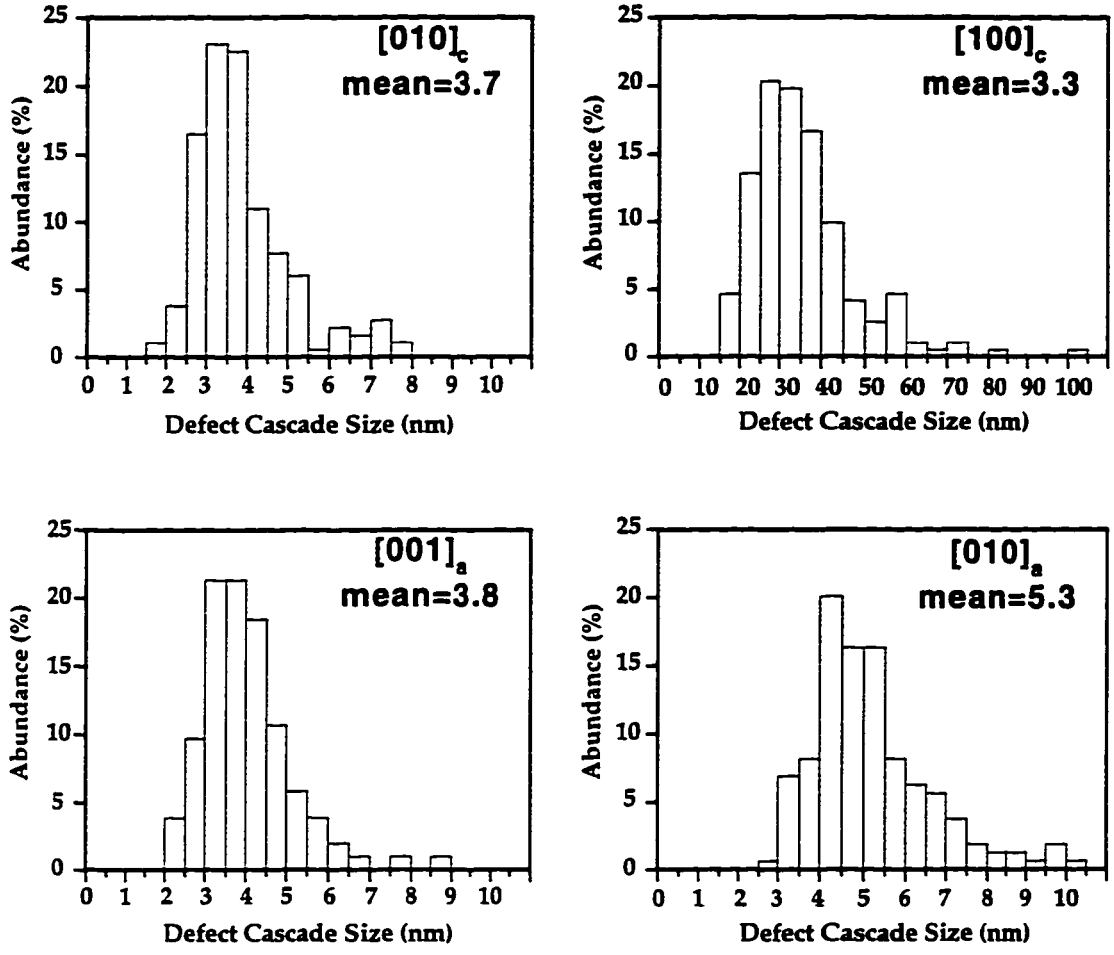

Figure 4.3 Defect cascade size distributions for the four different directions measured, holding the oxygen content at x = 0.1. Miller indices provide the measurement direction and the subscript indicates the axis near the irradiation direction. The $[100]_c$ and $[010]_c$ means are nearly the same, indicating a circular cross section for cascades produced by irradiation near the c-axis. The ratio of the $[010]_a$ and $[001]_a$ means is 1.6, indicating an elliptical cross section for cascades produced by irradiation near the a-axis.

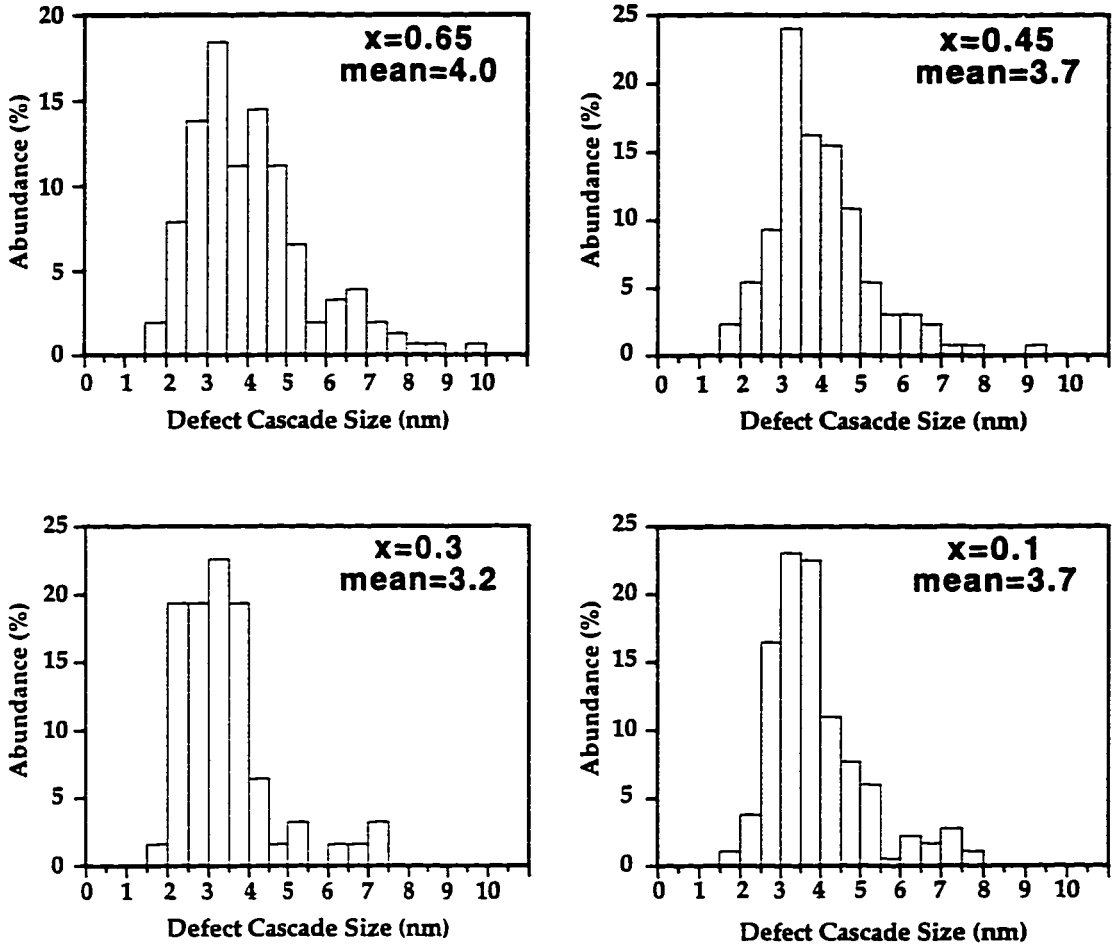

Figure 4.4 Defect cascade size distribution for the four different oxygen levels. All four distributions are for irradiation with 50 keV Kr^+ near the c-axis in $YBa_2Cu_3O_{7-x}$ and measured in the [010] direction. The mean size is similar over this range of oxygen stoichiometry, which implies that the defect cascade size is independent of oxygen concentration.

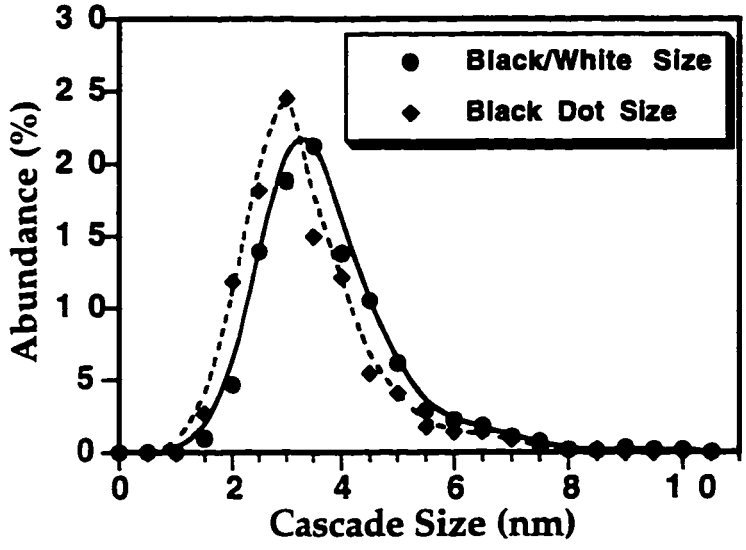

Figure 4.5 Size measurements were made on both black/white and black dot images of the defect cascades. The combined data for all four oxygen levels and all measurement directions, except $[010]_a$, are plotted for the black dot and black/white sizes. This was done to insure that there was not a large effect on either the mean value or the shape of the distribution by measuring cascade sizes with one or the other type of image contrast. Both distributions are very similar in both mean and shape.

4.3.2 Size and Nature of the Strain Field

The strain field size is possibly more important than the actual defect size in regard to magnetic flux pinning; hence, the strain field's extent was measured and found to be roughly twice the diameter of the defect cascade. The strain field size is measured parallel to **g**; unfortunately, this measurement is somewhat arbitrary as the contrast from the defect cascade gradually blends into the background. The endpoints were chosen at about a 70% drop in the intensity of defect contrast and this was then compared to the actual size for that particular defect cascade. It is important to realize that there is not a simple relationship between the decay of the strain field and

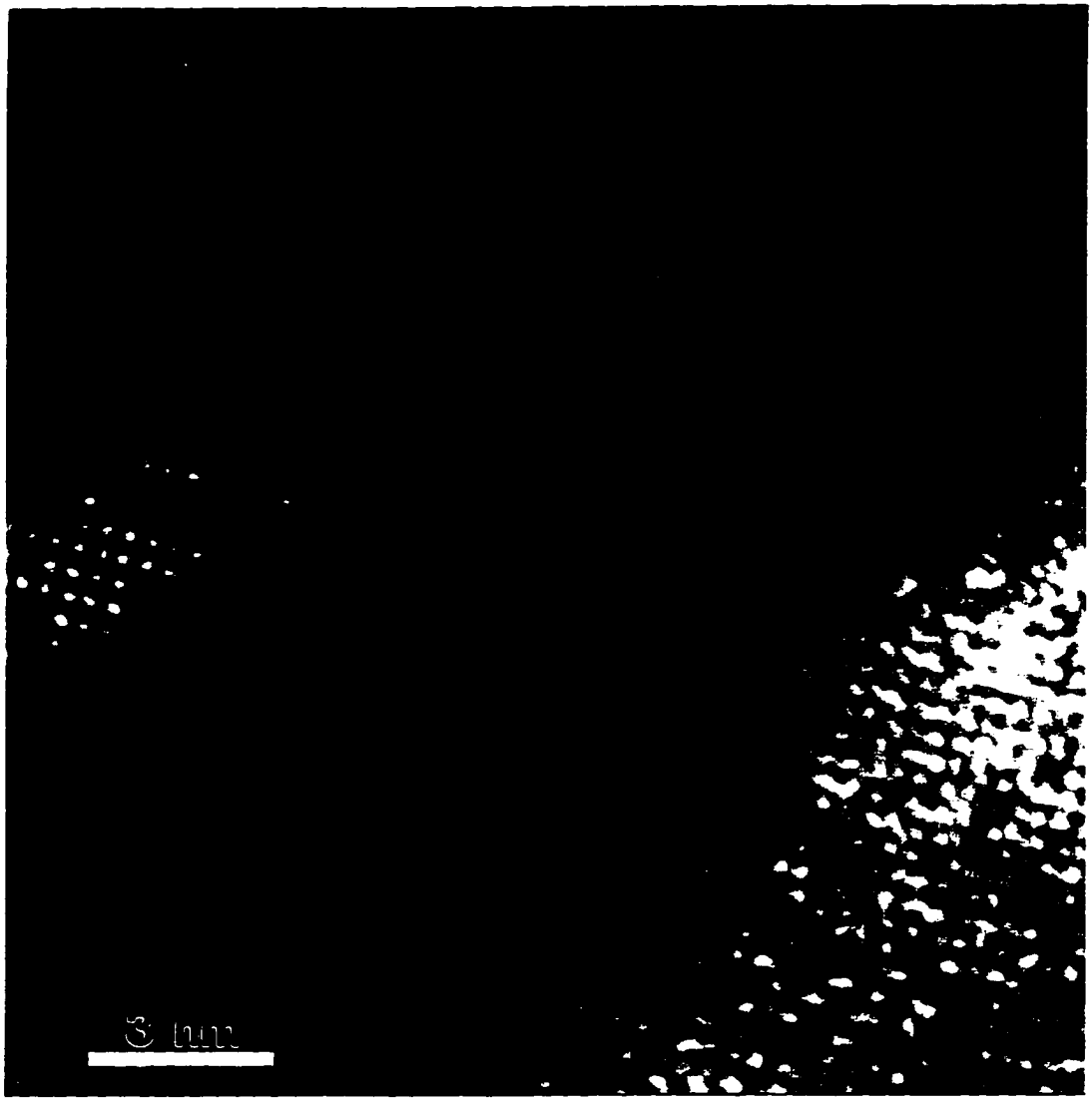

Figure 4.6 HREM image down the c-axis of a 50 keV Kr^+ defect cascade in $YBa_2Cu_3O_{6.35}$. The irradiation direction was near the c-axis and as the graphs in Figs. 4.3 and 4.4 predict the cascade cross section is circular with a diameter of 3.5 nm. The objective defocus is about 140 nm underfocus, which is close to the overlap defocus (160 nm) for the 0.385 nm fringes at 100 keV and a C_S of 1.75 mm.

the decay of the intensity in the image of that strain field; hence, the 70% drop used here does not correlate to a 70% decay in the actual strain field. The endpoints for the actual size, measured perpendicular to **g**, are easier to determine as the contrast change in this direction is abrupt. The strain to actual size ratio was consistently found to be two, and this held true for different oxygen contents, irradiation directions, and **g**'s used to form the dark-field image. Only defect cascades showing good black/white contrast from strong two-beam conditions were selected for strain field measurement.

Of less importance to magnetic flux pinning is the nature of the strain field, i.e., inwards or vacancy vs. outwards or interstitial. The defect cascades were determined to be interstitial. Unfortunately, in this case it turned out to be a very difficult determination to make and not much trust should be placed in this result. The method used here for determining the nature of the strain field is outlined below.

TRIM (Ziegler, Biersack, and Littmark 1985), a Monte Carlo program to simulate irradiation damage, was modified (Frischherz et al. 1993) to calculate the depth of the defect cascade's center of mass, and the calculated depth profile for 50 keV Kr^+ in YBCO is shown in Fig. 4.7.

The contrast in a DF image, created by a defect, depends upon the depth of the defect and the extinction distance ($\xi_{\mathbf{g}}$). Note that $\xi_{\mathbf{g}}$ is very sensitive to the deviation parameter, as illustrated for the (200) beam in Fig. 4.8. If the defect has a nearly spherical strain field, the contrast will either be a black dot or two connected lobes of opposite contrast, i.e., a figure eight shape with a one half black and the other half white. There are three

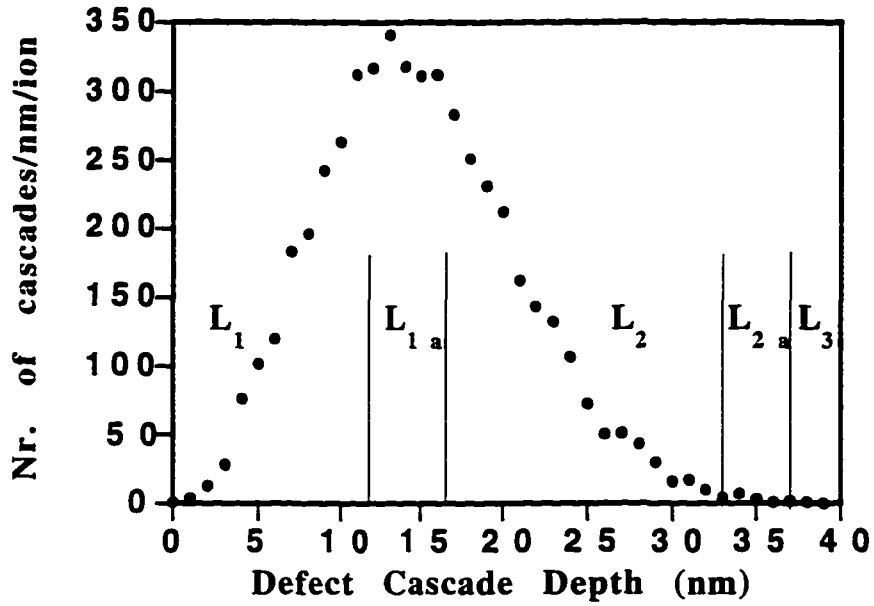

Figure 4.7 Defect cascade depth distribution for 50 keV Kr^+ in YBCO as determined using a modified version of TRIM. The positions for the three imaging layers are indicated (see Fig. 4.9).

imaging layers at the top and bottom of the TEM sample. The black to white vector (ℓ) for a particular type of defect reverses as it passes from one layer to the next. A reversal of ℓ is also observed if the direction of the strain field is reversed, e.g., interstitial vs. vacancy. A schematic (Fig. 4.9) of these rules for the contrast of a defect at different depths, in terms of ξ_g, is presented for defects of either a vacancy or interstitial nature.

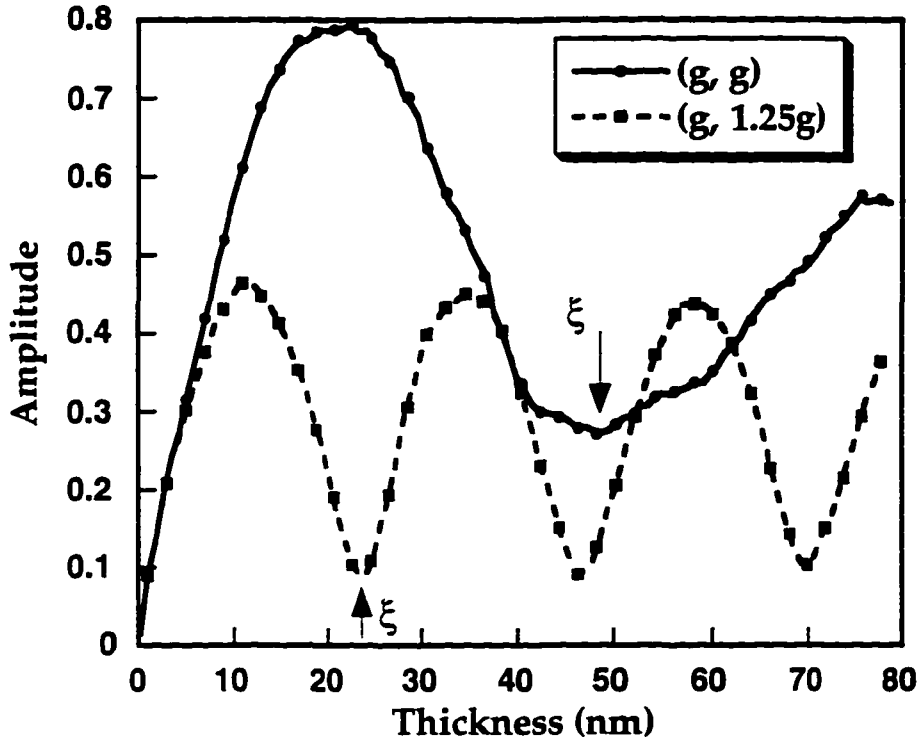

Figure 4.8 Plot of the (200) beam's amplitude as the electrons propagate through YBCO for (g, g) and (g, 1.25g).

By combining the last three figures it is possible to generate Fig. 4.10, which shows the range of allowed crystal tilt in which a majority of the defects will be in the second imaging layer. Images should be taken in this range and the direction ℓ, i.e., black to white vector, for each defect showing unambiguous black/white contrast recorded. The majority direction of ℓ is from defects in the second layer, and the nature of the strain field can be determined as follows: a majority direction parallel to **g** is interstitial while anti-parallel to **g** is vacancy. The problem in this case arises from the depth profile of the defect cascades, recall Fig. 4.7; they are tightly distributed around the boundary of the first and second layer. Hence, two complications arise:

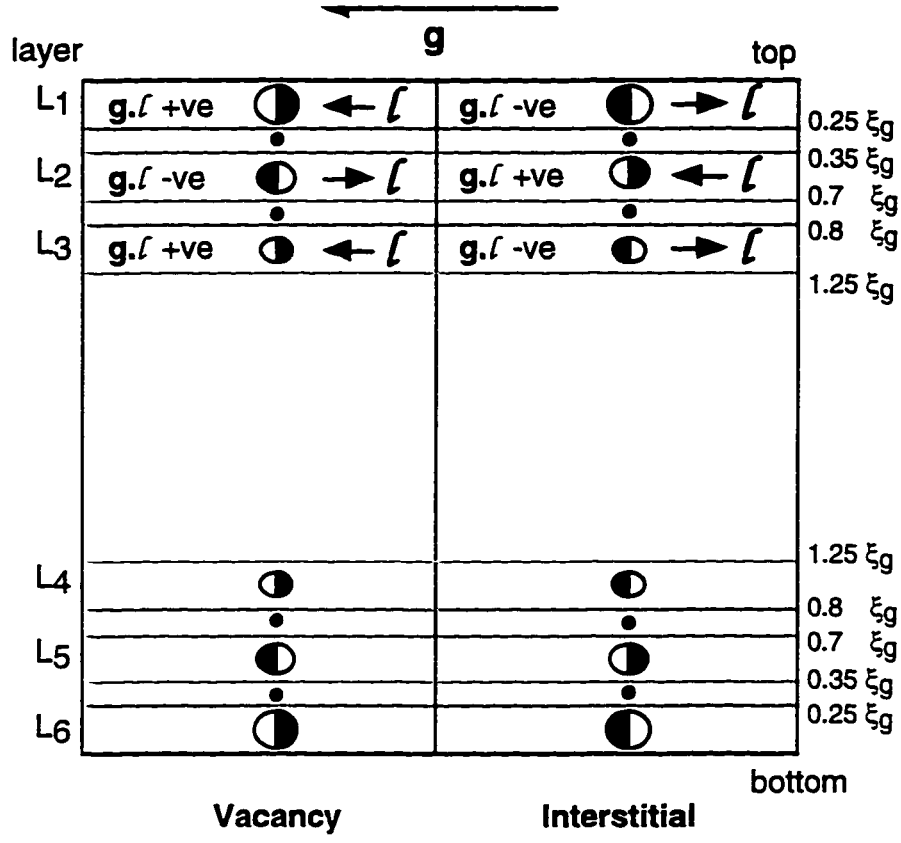

Figure 4.9 Schematic of the black/white contrast direction for defects residing in each of the three layers at either the top or bottom of the TEM sample. The left side is for the case of a vacancy strain field while the right side is for an interstitial strain field.

L_1 defects are more easily imaged and thus preferentially counted, secondly a large portion of defects close to the L_1 to L_2 boundary show up as black dot contrast. At certain crystal tilts, these combine to create instances were a majority direction might constitute only 55%, and given the error in these measurements this is dangerously close to incorrectly determining the majority direction. Note that there is an error not only in making the direction measurements but also in the depth profiles generated by TRIM.

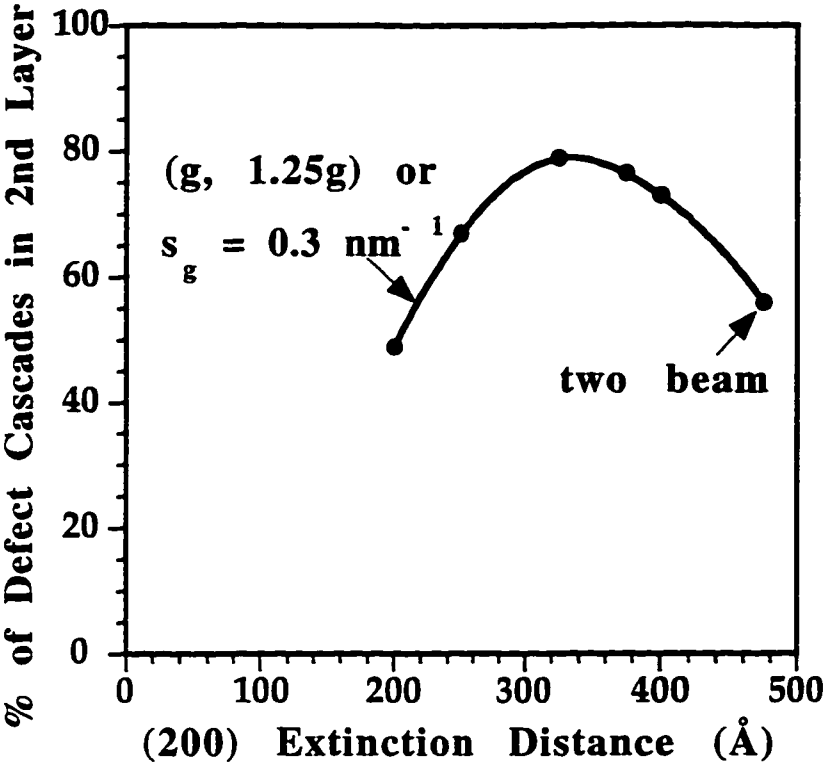

Figure 4.10 Plot of the defect fraction in L_2 as a function of ξ_g . In order to have a majority of the defects imaged in L_2 the sample should be tilted between (g, g) and (g, 1.25g), in the case of the (200) beam.

4.3.3 Yield of Defect Cascades per Ion

Measuring the defect cascade density was achieved by printing the dark-field negatives to a total magnification of 500,000 and selecting an area with good defect contrast. The cascades clearly showing black/white contrast were counted as one and cascades with less pronounced black/white or black dot contrast as one-half (Frischherz et al. 1993). This is due to the difficulty in distinguishing between surface artifacts and cascades showing weak contrast. The total error was assigned as one-half the black dot density plus a 10% error in the ion fluence (Vetrano 1990).

The yield of defect cascades per incident ion was 50±10% which is comparable with a previous study (Frischherz et al. 1993). Based on TRIM calculations, again recall Fig. 4.7, nearly every ion will make a cascade in the first 35 nm, raising the question of what happened to the other half of the defect cascades produced. Previous work showed a HREM image of a defect cascade suggesting partial recrystallization (Frischherz et al. 1993). This leads to the suggestion that about half the defect cascades may have fully recrystallized and thus are invisible in a strain contrast image.

4.4 Discussion

Defect cascade sizes produced by ions incident near the c-axis in YBCO are relatively isotropic and independent of oxygen stoichiometry. For ions incident near the a-axis the $[001]_a$ size was the same as the diameter of cascades produced by ions incident near c-axis. For only the x = 0.1 sample, the size along the $[010]_a$ direction was measured and was found to be 5.5 nm. This same combination of an elliptical cross section for ions incident near the a-axis and circular cross section for ions incident near the c-axis was reported for high-energy heavy ion track damage in YBCO thin films and ceramics (Zhu et al. 1993). The fact that similar elliptical cross sections are found in both types of damage, suggest that an explanation based on a highly anisotropic thermal conductivity in these directions (a or b vs. c) is likely, as suggested by Zhu (Zhu et al. 1993). That is, the defect size anisotropy is not related to the atomic recoil mechanisms (far different between the nuclear stopping at 50 keV and the electronic stopping at several hundred MeV) but to the dissipation of energy or cooling mechanism. In contrast to a different

report by Zhu that the diameter of heavy ion track damage does vary with oxygen (Zhu et al. 1993), I found the defect cascade size to be independent of O content.

A statistical analysis was performed on all the data to find any trends present. The standard error, i.e., the standard deviation divided by the square root of the counts, is presented in Table 4.1 and a few trends are evident. If the crystallographic direction is held constant, then there is a 10±5% increase in the mean from x = 0.1 to x = 0.65; this holds true for all three directions measured. A slight size anisotropy, $[100]_C \leq [010]_C$, can be seen by holding the oxygen stoichiometry constant. To confirm these trends, simultaneous 95% confidence intervals using Scheffé's procedure were determined. This procedure verified that any set of means different by at least 0.20 nm can be considered statistically significant in their difference. While these differences in the means are significant from a statistical point of view, the magnitudes of the absolute differences are about 0.5 nm; thus, there is little implication in regard to the magnetic flux pinning properties.

The near uniform size of the defect cascades as a function of oxygen calls into question the explanation by Wisniewski et al. regarding the difference in magnetic flux pinning between the 60 and 90 K phases that had undergone neutron irradiation (Wisniewski et al. 1994). They assumed a large cascade size difference (50%) between the two phases based on the theoretical work using low energy (100-300 eV) ions (Kirsanov, Musin, and Wisniewski 1993). Considering that the defect cascades produced by the 50 keV Kr^+ irradiation should be similar to those produced by neutron irradiation coupled with our uniform cascade size results, an explanation of

the magnetic flux pinning behavior for neutron irradiation of samples with different oxygen stoichiometries should not be attributed to a variation in cascade size. The strain field size was nearly twice the cascade size for all oxygen contents. Thus, if one considers the strain field as the magnetic flux pinner then the size is still not a function of the oxygen concentration.

4.5 Conclusion

Single crystals of $YBa_2Cu_3O_{7-x}$, of varying oxygen stoichiometry, were irradiated with 50 keV Kr^+ to create defect cascades similar to those resulting from fast neutron irradiation. Two-beam dark-field TEM in weak dynamic conditions was used to measure the defect cascade size distribution in the principal axes for four different oxygen stoichiometries; HREM was used to verify the mean size of these cascades.

The mean size of the defect cascades generated was independent of oxygen stoichiometry over $x = 0.65$ to $x = 0.1$, which indicates that magnetic flux pinning does not vary due to any association between the oxygen concentration and the cascade size. This contradicts the interpretation by Wisniewski in which a size variation in defect cascade size was assumed to explain flux pinning behavior in neutron irradiated 60 and 90 K phase YBCO (Wisniewski et al. 1994).

For Kr^+ incident near the c-axis the defect cascades have on average a 3.5 nm diameter circular cross section perpendicular to the ion beam, while an elliptical cross section was found for ions incident near the a-axis. The minor axis (3.5 nm) was in the [001] direction and the major axis (5.5 nm) was in the [010] direction. This aspect ratio of 1.6 matches that found for

high-energy heavy ion track damage in $YBa_2Cu_3O_{7-x}$, which implies that the shape is determined not by the recoil damage mechanism, but by the cooling or relaxation stage where the anisotropy in thermal conductivity determines the final defect shape.

Chapter 5 PROTON IRRADIATION OF $YBa_2Cu_3O_{6.9}$

5.1 Introduction

As discussed in 2.3, proton irradiation of YBCO generates point defects on all sub-lattices as well as creates a few small defect cascades. It has been proposed that these point defects, specifically Cu and O interstitials migrate and coalesce into platelets on the b-c plane and that these platelets are the primary flux pinning defects at 70 K (Kirk 1993). Another flux pinning study suggests instead that the point defects themselves are primarily responsible for the magnetic flux pinning and the larger platelet defects have a more subdued affect on the enhancement of J_C (Civale et al. 1990). This chapter presents new experimental evidence regarding these two hypotheses and it also confirms previously reported defect information. While it remains unclear as to which defects are significant in enhancing Jc, the information presented is an important key and can be used in suggesting new experiments.

By using TRIM it is possible to calculate the number of Frenkel pairs (FP) generated per proton over a given depth. Approximately 6 FP are generated per proton over a penetration depth of 30 microns, typical single crystal thickness (Civale et al. 1990). If the proton fluence is $1x10^{16}$ $H^+ \cdot cm^{-2}$, this results in 0.0035 FP per unit cell or 1 FP per 288 unit cells. Given that the damage rate is uniform over the first 30 microns (see Fig. 2.2) and that a typical region suitable for HREM imaging on a fragment of the crushed

single crystal is 10 nm thick, then there are 0.2 FP/nm^2 in a HREM image. These calculations assume that recombination of the FP does not occur; hence, these numbers could be even lower. Table 5.1 presents the FP densities for three of the proton fluences investigated.

Table 5.1 Density of Frenkel pairs (FP) generated by 3.5 MeV proton irradiation in YBCO for three different fluences. 10 nm thickness is assumed for HREM.

	$6x10^{15}$ $H^+ \cdot cm^{-2}$	$1x10^{16}$ $H^+ \cdot cm^{-2}$	$3x10^{16}$ $H^+ \cdot cm^{-2}$
FP/unit cell	0.0021	0.0035	0.010
FP/nm^2 in HREM	0.12	0.20	0.60

Heavier elements have a much higher scattering power for electrons, as such, the Y and Ba interstitials are the primary point defects evident in the HREM images. This is the same concept discussed in Chap. 3 in which models containing only O related defects could not reproduce the contrast variations seen in the HREM images, while the simulations of models containing the much heavier Au substitutional atoms matched the experimental images. If one assumes that 3.5 MeV protons generate point defects equally on all atomic positions, the combined Y and Ba FP density is approximately one-quarter of the densities given in Table 5.1. Note that as these defects are probably less mobile than Cu and O, they would be less likely to recombine.

This chapter, more so than the other chapters, represents a work in progress with three main components, i.e., three different types of defects are presented in the order they were found. The first defect (5.4) is a platelet in

the b-c plane most likely comprised of irradiation induced Cu and O interstitials which have migrated and coalesced. The second type of defect (5.5) is point defects, i.e., Frenkel pairs, and while HREM of these defects was attempted the results were hampered by a lack of samples and contamination problems. Fortunately some information about the point defects was also obtained from electron diffraction patterns taken at different electron energies; specifically, the point defects were found to order under a high energy electron beam. The final defect (5.6) is believed to be extrinsic stacking faults which are 10-100 nm in diameter and located in the basal plane; these were found only in YBCO crystals grown in ZrO_2 crucibles after irradiation. Unfortunately the unirradiated material was not carefully investigated for the presence of these stacking faults; hence, they may occur in the as-grown crystals, i.e., they are not the result of irradiation damage.

5.2 Experimental Details

YBCO single crystals were grown in both ZrO_2 and Au crucibles as discussed in 2.1.1. The ZrO_2 grown crystals are nearly free of any cation doping, as opposed to the crystals grown in Au crucibles. It is useful to have crystals as nearly perfect as possible prior to the proton irradiation, so that only the post-irradiation defects are studied. YBCO crystals grown in ZrO_2 crucibles were irradiated to fluences of 0.6 or $3x10^{16}$ $H^+ \cdot cm^{-2}$ (see 2.4.1 for details about the irradiation procedure), also crystals grown in a Au crucible were irradiated to either 1 or $2x10^{16}$ $H^+ \cdot cm^{-2}$.

The T_c curves (see 2.6 for the details about Tc measurement) for three crystals grown in ZrO_2 crucibles were measured before and after irradiation;

the results are plotted in Fig. 5.1. The curves prior to irradiation are very sharp and the onset T_c is about 93 K. This indicates the crystals are single phase and optimally oxygenated. The T_c drops about 0.5 K for the $6x10^{15}$ $H^+ \cdot cm^{-2}$ dose and 2.75 K for the $3x10^{16}$ $H^+ \cdot cm^{-2}$ dose. The shapes of the magnetization curves before and after irradiation are nearly identical, as evidenced in Fig. 5.2 for the fluence of $3x10^{16}$ $H^+ \cdot cm^{-2}$. The post-irradiation curve has been shifted up by 2.75 K without altering the shape, and the overlap implies that the irradiation damage, which produces the degradation in T_c, is uniform throughout the crystal.

5.3 The Unirradiated Case

In order to demonstrate the presence and behavior of irradiation induced defects, it is useful to show the defect free case, i.e., an unirradiated YBCO crystal grown in a ZrO_2 crucible. Such a crystal with a T_c of 93 K was crushed and TEM was performed. Extremely long (up to 5 min.) electron diffraction patterns were taken to determine the presence or in this case absence of diffuse streaks. Recall that in Chap. 3 very weak diffuse streaks were evident in c-axis diffraction patterns as a result of the Au substitutional atoms ordering into short rods. Many attempts were made to observe the presence of such streaks, for instance see Fig. 5.3, but none were found. While this does not preclude the presence of individual point defects it does suggest that there are few if any small clusters of point defects. For reasons that will be clear later, diffraction patterns were taken at 100, 200, and 300 keV after one hour of exposure with a focused electron probe at each voltage; no change in the patterns occurred.

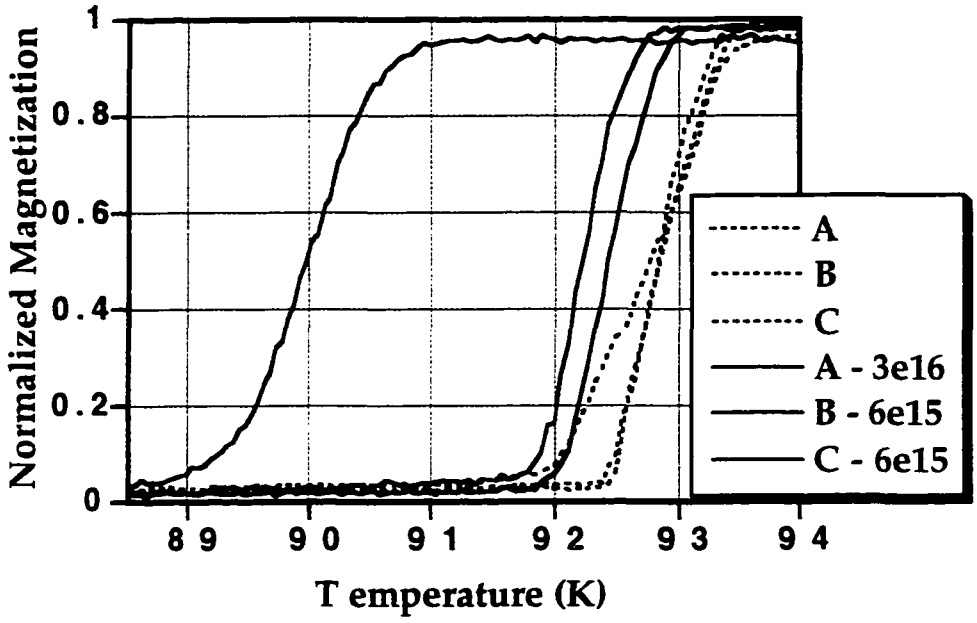

Figure 5.1 Tc curves before and after proton irradiation: crystal A was irradiated to $3x10^{16}$ $H^+ \cdot cm^{-2}$ and crystals B and C to $6x10^{16}$ $H^+ \cdot cm^{-2}$.

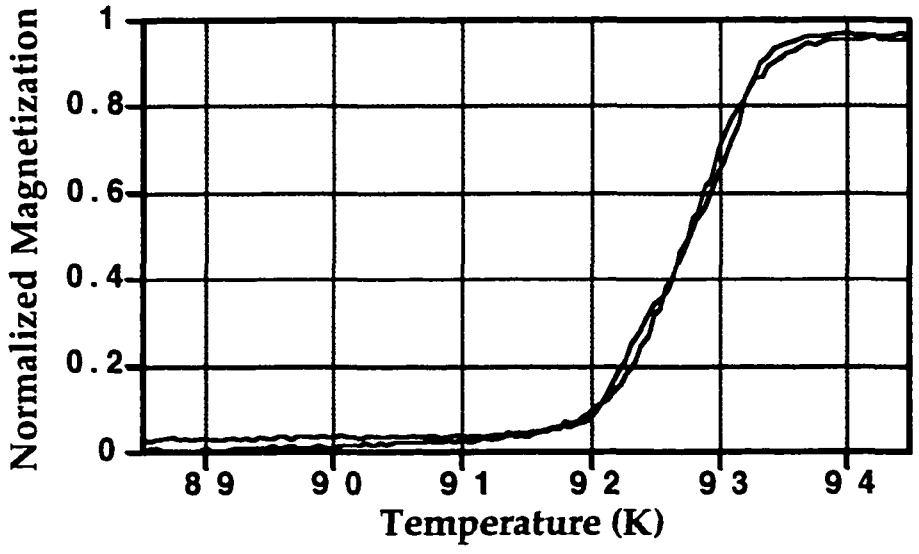

Figure 5.2 T_C curves for crystal A in Fig. 5.1. The post-irradiation curve (red) has been shifted up 2.75 K to illustrate the similar shape of the curves before and after irradiation.

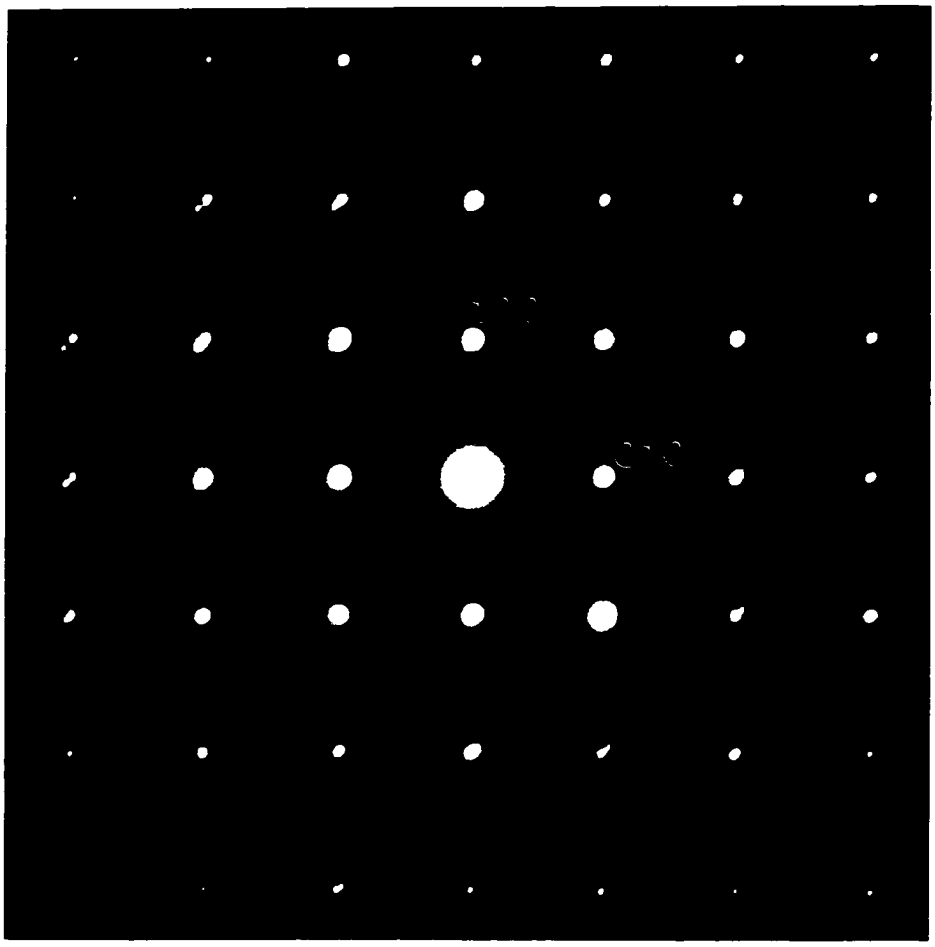

Figure 5.3 Electron diffraction pattern of an unirradiated YBCO crystal grown in a ZrO_2 crucible. The absence of any streaks or extra reflections indicates the lack of defects.

Attempts were made to obtain a HREM image down the c-axis that showed the perfect repetition in contrast generated by a defect free crystal. Due to severe carbon contamination and limited supply of these exceedingly small crystals, this image was never satisfactorily obtained.

5.4 Platelet Defects

Except where stated this section deals only with YBCO single crystals grown in Au crucibles and irradiated to a fluence of $2x10^{16}$ $H^{+}{\cdot}cm^{-2}$. All of the results presented here, e.g., size, strain field, and thermal stability, were obtained using dark-field TEM. (See Chap. 4 for a detailed discussion regarding the imaging of small defects using dark-field TEM.) Originally it had been hoped to ascertain the atomic structure of these defects, but unfortunately this proved to be rather difficult due to rapid electron damage at the high energies required to image the structure with sufficient resolution. The defects presented in this section show up in dark-field images with a black/white contrast, as such, these defects will henceforth be referred to as B/W defects.

5.4.1 Strain Field Determination

Dark-field TEM was used to image the B/W defects to determine any anisotropy in the strain field. It was found that the defects are readily visible using the (200) reflection, for instance see Fig. 5.4, while the (020) reflection did not image the defects very well, if at all. This indicates that the strain field is highly anisotropic in the a-b plane. Attempts to image the defects with c-axis reflections, namely the (006), also proved to be difficult. This

Figure 5.4 (200) dark-field images of 3.5 MeV proton irradiated YBCO [ZrO_2 crucibles used for the crystal growth in (a) and (c)] showing the B/W defect density change for three different fluences (a) $6x10^{15}$ $H^+ \cdot cm^{-2}$, (b) $2x10^{16}$ $H^+ \cdot cm^{-2}$, and (c) $3x10^{16}$ $H^+ \cdot cm^{-2}$

implies that the main strain component lies along the a-axis, which could arise from a disk shaped or platelet defect in the b-c plane.

The density of B/W defects increases with an increase in proton fluence, see for instance Fig. 5.4. It is very difficult to make actual density measurements because the local crystal thickness is both unknown and changing. However, it is safe to make qualitative observations when the changes are this dramatic, e.g., there are hardly any defects in the low dose case while they are abundant in the high dose. This change in the B/W defect density with dose coupled with the absence of similar black/white contrast features in the dark-field images of unirradiated material demonstrates that these defects are created by the proton irradiation.

5.4.2 Size Measurements

The diameter of the B/W defects was measured from the dark-field TEM images. Chapter 4 discusses the manner in which a small defect may be sized in a strain contrast image. Over 150 defects were sized from (200) dark-field images, and the size distribution is plotted in Fig. 5.5. The mean size is 3.6 nm, which coincidentally is the same as the diameter of the 50 keV Kr^- defect cascades (see Chap. 4).

5.4.3 In-situ TEM Annealing Behavior

To associate the platelet defects, discussed in 5.4.1 and 5.4.2, with their possible influence on the overall enhancement of J_c, annealing experiments were carried out. Proton irradiated YBCO single crystals were annealed at

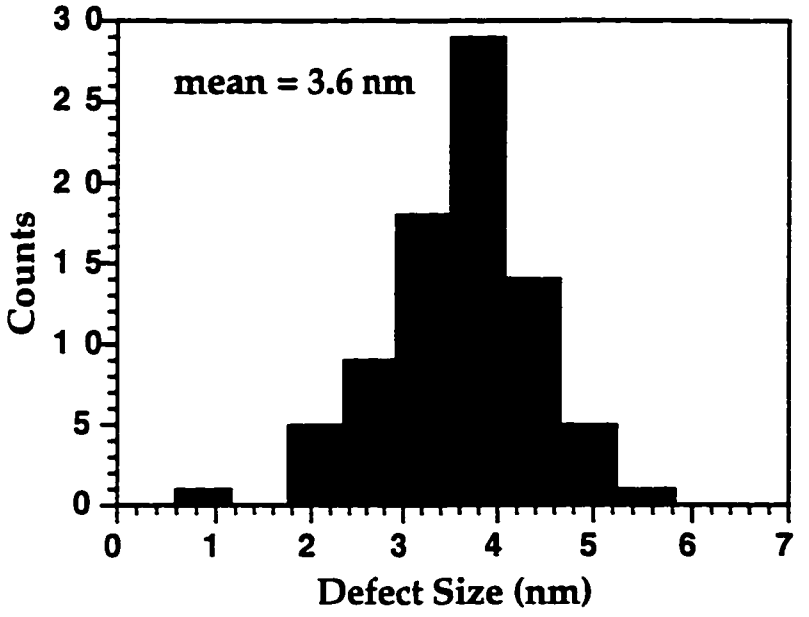

Figure 5.5 Size distribution along the [020] direction of the B/W defects created by 3.5 MeV proton irradiation of YBCO single crystals.

100, 200, 300, and 350°C for 8 hours at each temperature and the recovery of J_C to its pre-irradiated value was determined after each anneal (Viswanathan et al. 1996). Figure 5.6 shows this recovery (R) of J_C to its pre-irradiation value as a function of annealing, where R is defined as,

$$R = \frac{J_c^{Irr} - J_c^{Ann}}{J_c^{Irr} - J_c^{Unirr}}. \qquad 5.1$$

In order to determine which defects anneal out and thus their absence possibly responsible for the recovery of J_C, in-situ TEM anneals were performed at the same temperatures as the bulk anneals but for only 10 min. at each temperature. Dark-field images were recorded in the same area after each 10 min. anneal to monitor the presence of the B/W defects. The results

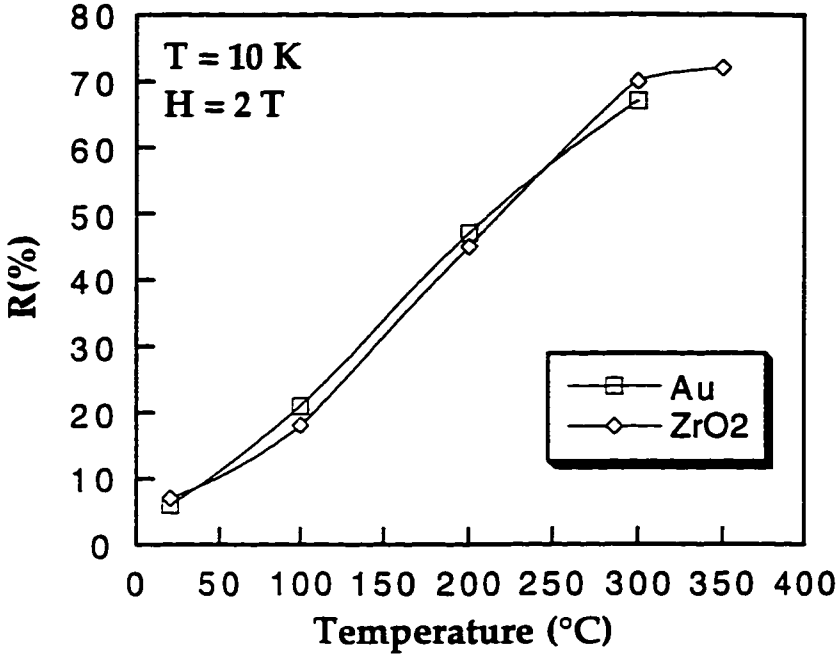

Figure 5.6 Recovery (R) of J_c to its pre-irradiation value vs. annealing temperature (Viswanathan et al. 1996). Two YBCO crystals one grown in a Au crucible the other in a ZrO_2 crucible, each irradiated with 3.5 MeV protons to a fluence of $1x10^{16}$ $H^+ \cdot cm^{-2}$, are presented.

are plotted in Fig. 5.7 and it is obvious that the B/W defects are disappearing. There are a few reasons for pause in regard to these results: (1) The 10 min. chosen for these anneals is not close to the 8 hours for the bulk anneals. (2) The effect of a thin foil vs. a bulk sample is unknown. (3) Individual point defects are mobile and hence will also recover, leading to an ambiguity in terms of whether the B/W or point defects are responsible for the change in J_c.

The results of annealing the proton irradiation induced defects is interesting because B/W defects in neutron irradiated YBCO, which are exclusively defect cascades, did not anneal out (Frischherz et al. 1994). The neutron annealing experiment was carried out in a very similar manner to

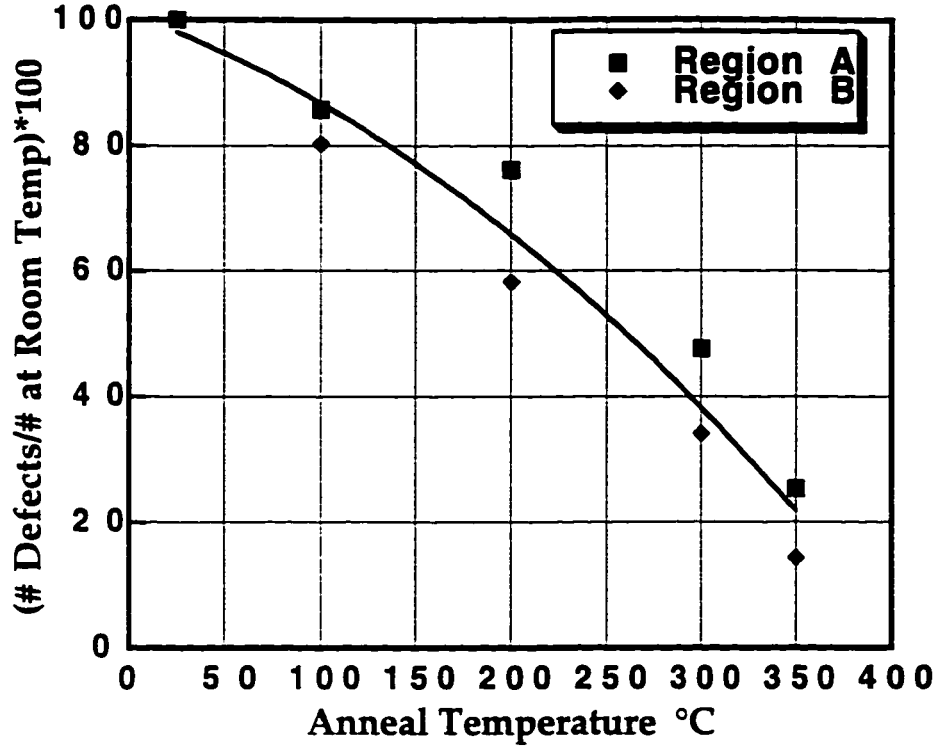

Figure 5.7 Percentage of B/W defects remaining after in-situ TEM anneals for 10 min. at each temperature. Note that approximately 40 defects were located at room temperature for each of the two regions investigated.

that used here and the defect cascades did not disappear. This lends support to the notion that protons generate a lot of point defects which migrate and coalesce into platelets. It is believed that the platelets are annealing out and the remaining 20-30% of the B/W defects are defect cascades. This is supported by TRIM calculations performed and interpreted by Dr. Kirk which suggest that about 25% of the B/W defects are defect cascades.

5.5 Clusterng of Point Defects

The previous section provided evidence for platelet defects that likely arise from the migration and coalescence of Cu and O interstitials. The

proton irradiation, however, generates point defects on all sublattices and this section reports on the less mobile heavier cation Frenkel pairs. As will be shown these point defects cluster when irradiated with 300 keV electrons. This leads to a Catch 22, namely, to image these point defects high-energy electrons are required for the necessary resolution but these same electrons alter the very defects being imaged. Note that Chap. 3 is exempt from this Catch 22 because not only is Au a stronger scatterer of electrons than Y or Ba making 100 keV electrons sufficient but the location of Au was also known and fixed. Still, attempts were made to obtain HREM images of the point defects, see for instance Fig. 5.8 which shows the comparison of a pre- vs. post-irradiated YBCO crystal grown in a Au crucible. Qualitatively it is very clear that there is a substantial amount of damage in the irradiated crystal. A conservative estimate of the point defect density in the irradiated crystal is one defect every five unit cells; this is based on the damage appearing in the HREM images being at least two times greater than that found in the Au grown crystals which had on average 1 Au atom per 10 unit cells. Note, this defect density is about two orders of magnitude greater than the densities predicted by TRIM leading to a discrepancy that is difficult to justify. Similar HREM images were not obtained for the other irradiation fluences investigated; this was primarily due to the limited supply of crystals grown in ZrO_2 crucibles.

While substantial information regarding the point defects was not obtained via HREM due to a lack of thin crystals, there were plenty of crystal fragments suitable for electron diffraction analysis. Crystals irradiated to proton fluences of 0.6 and $1x10^{16}$ $H^+ \cdot cm^{-2}$ generated streaks along the [200]

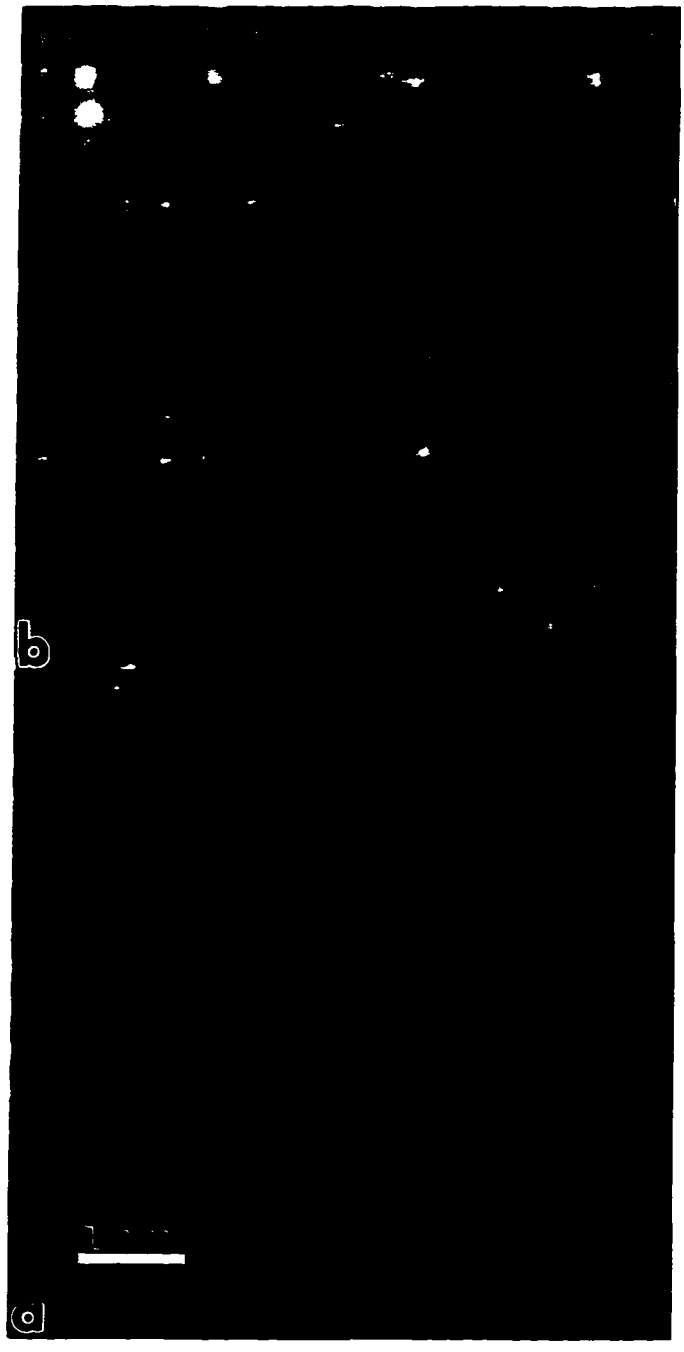

Figure 5.8 c-axis HREM images of YBCO crystals grown in Au crucibles (a) prior to and (b) after irradiation with 3.5 MeV protons to a fluence of $1x10^{16}$ $H^{+}\cdot cm^{-2}$.

direction in c-axis diffraction patterns after exposure to a 300 keV electron beam, Fig. 5.9 (a). Note that very long exposures at 100 and 200 keV did not generate these streaks and it was only after the 300 keV electron irradiation that the streaks were formed. Similar streaks, albeit very weak, were evident in 100 keV electron diffraction patterns for the high proton fluence case ($3x10^{16}$ $H^+ \cdot cm^{-2}$), see Fig. 5.9 (b), which suggests that the defects causing these streaks form in a heavily defected crystal without the aid of the electron beam.

In order to determine the reciprocal space extent of these streaks diffraction patterns were recorded at various crystal tilts up to 10° off the c-axis. Two such off-zone patterns are provided in Figs. 5.9 (c) and (d). The selected area for Fig. 5.9 (d) had been previously irradiated with 300 keV electrons for about 1.5 hr; the streaks at these long exposures begin to transform and are rather difficult to associate with a defect shape. Note that Fig. 5.9 (d) was obtained from an area with multiple twin lamellae; hence, the streaks are in two directions. Both the on-zone and off-zone diffraction patterns imply the streaks arise from the intersection of the Ewald's sphere with rod's of diffuse intensity lying in the [200] direction. This is because the streaks fade out in the on-zone patterns with increased reciprocal space extent and the off-zone patterns have streaks only when the Ewald's sphere intercepts the zero order Laue zone.

The defect's shape in real space is simply the Fourier transform of the reciprocal space rods; hence, the defects are discs with their surface normal parallel to the streaks, i.e., the discs lie within the b-c plane. The disc's diameter is evident in the width of the streaks in the diffraction patterns. To

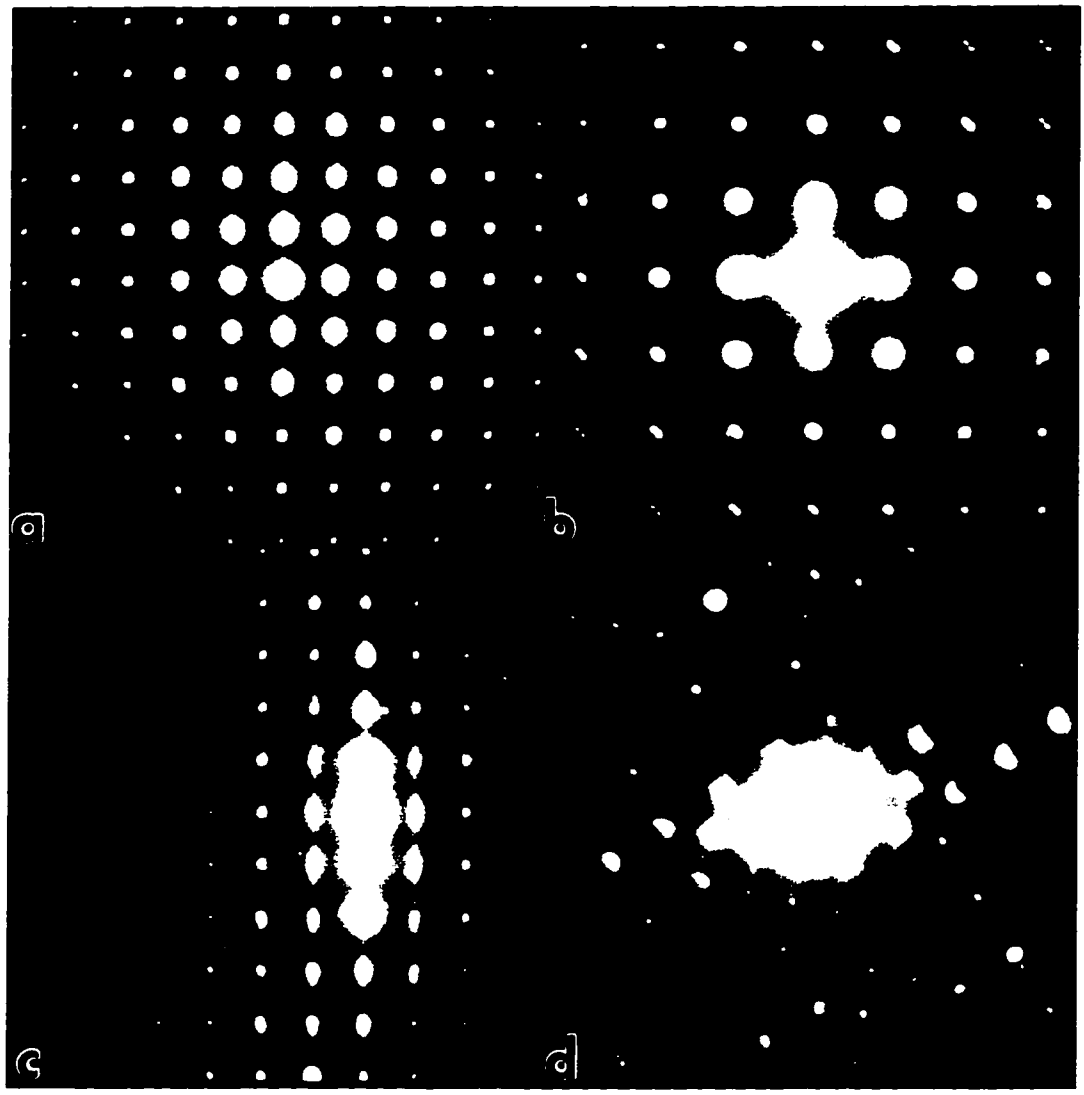

Figure 5.9 Electron diffraction patterns of 3.5 MeV proton irradiated YBCO crystals on or near the c-axis taken with various electron energies and proton fluences. (a) 0.5 hr at 300 keV and $1x10^{16}$ $H^+ \cdot cm^{-2}$ (b) 0.5 hr at 100 keV and $3x10^{16}$ $H^+ \cdot cm^{-2}$ (c) 0.75 hr at 300 keV and $3x10^{16}$ $H^+ \cdot cm^{-2}$ (d) 1.5 hr at 300 keV and $3x10^{16}$ $H^+ \cdot cm^{-2}$

a first approximation the width of the streaks is roughly 1/10 of $\mathbf{g}_{010}$; therefore the disc's diameter should be about 4 nm. The streaks are nearly continuous and thus the width of the disc must be less than 1 nm. Note the dimensions and orientations of these defects match the B/W defects presented in 5.4.

The fact that 100 and 200 keV electrons do not cluster the point defects indicates that there is a threshold energy to assist the migration of these point defects. Figure 5.10 plots the maximum recoil energies for electrons colliding with O, Cu, Y, and Ba as a function of electron energy. It is clear that the threshold energies required to cluster the cation defects are roughly between 5 and 15 eV. These thresholds are very large compared to the normal migration enthalpies of interstitials or vacancies in a metal, which are typically 0.1 eV and 1 eV respectively (Schilling 1994). This discrepancy in threshold energies might be explained by considering the difference of point defect migration in a close-packed metal vs. a highly anisotropic ionic structure. The fact that streaks were not evident in electron diffraction patterns from crystals annealed in-situ at 400 °C supports these high displacement energies as the thermal energy available at 400 °C is considerably less than 5 eV.

It is significant that streaks were never observed when the crystals were oriented with either the a- or b-axis parallel to the electron beam. This suggests that similar defect clustering does not occur in these zone axes. It might be possible that the recoil energies do not exceed the displacement threshold in these axes or conversely that they far exceed the threshold and the material rapidly damages into an altogether different structure. HREM

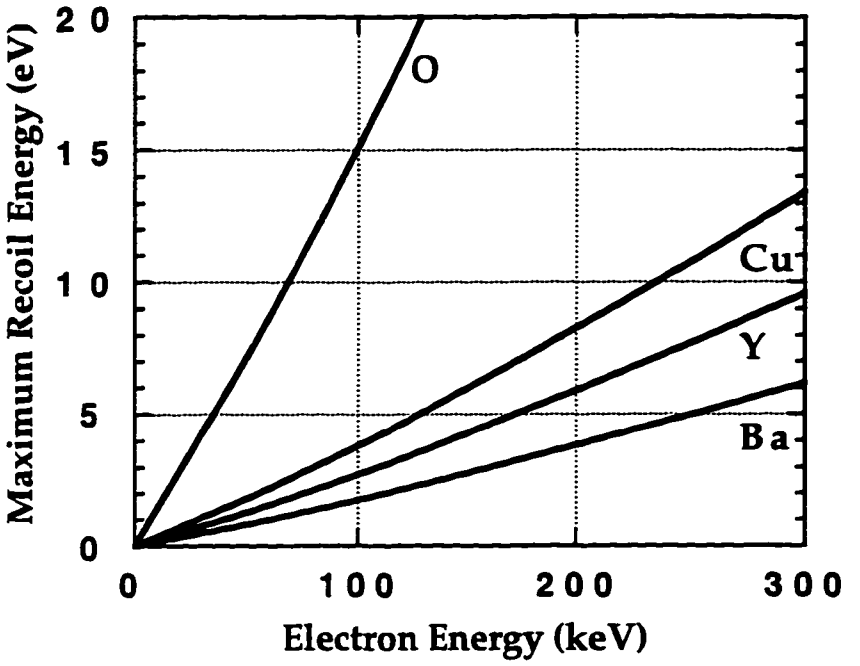

Figure 5.10 Recoil energies for the cations in YBCO at three electron energies. This plot is provided by Dr. Kirk.

images down a- or b-axis axes support the later, see for instance Fig. 5.11. The atomic structure seen in Fig. 5.11 is heavily distorted and the amorphous edge was growing into the crystal indicating the structure was amorphizing, this is a fingerprint for preferential oxygen loss at the edge of the crystal due to electron beam damage (Marks et al. 1988; Zandbergen, Gronsky, and Thomas 1988).

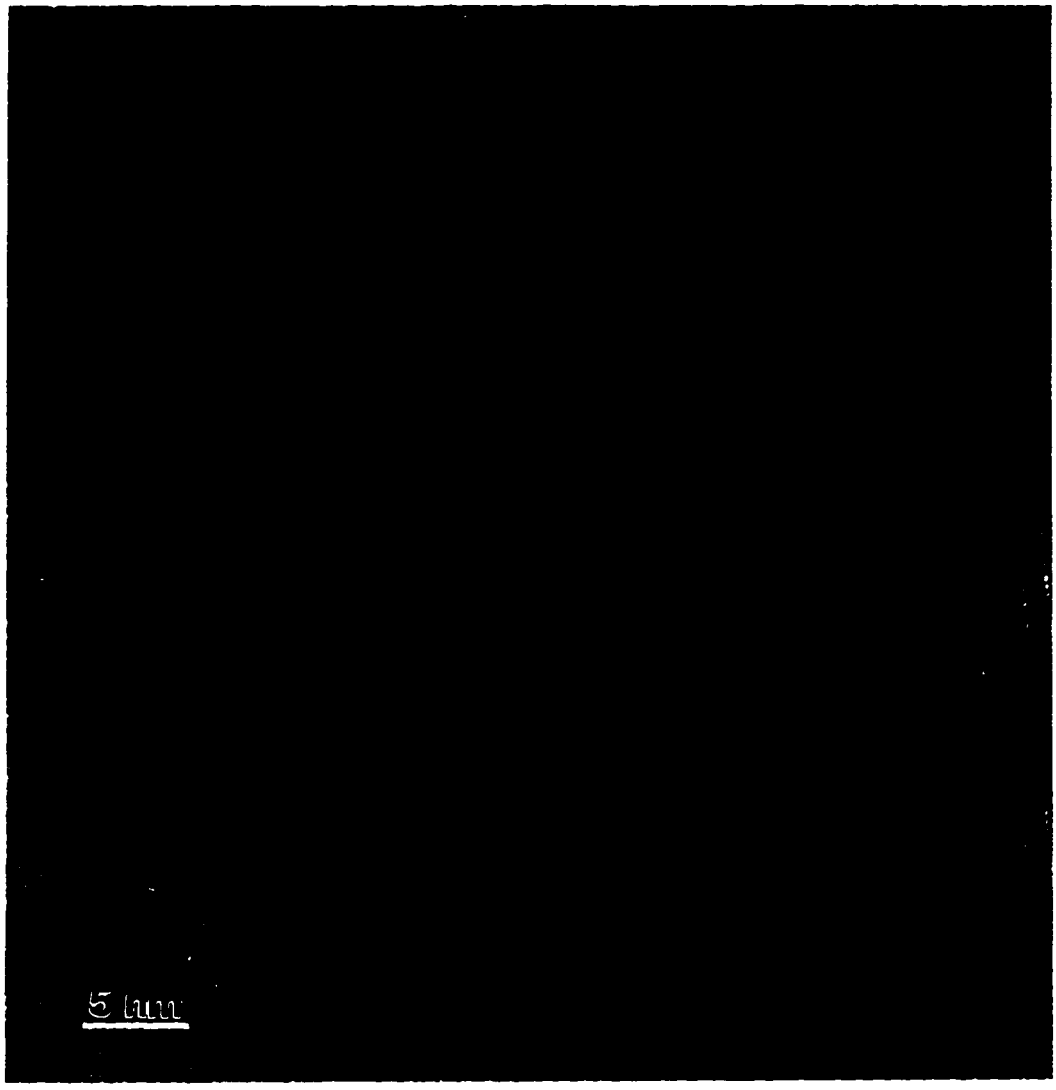

Figure 5.11 a-axis HREM image after brief exposure to 300 keV electrons showing a highly distorted structure and an amorphous edge which was growing into the material.

5.6 10 to 100 nm Stacking Faults

This section presents evidence for large (10 to 100 nm) defects which appear to be extrinsic stacking faults in the a-b plane. These stacking faults, see for instance Figs. 5.12 and 5.13, appeared only in proton irradiated YBCO crystals grown in ZrO_2 crucibles and only in c-axis strain contrast images. Stacking faults in YBCO typically are extrinsic, consisting of an extra CuO_2 plane parallel to the a-b plane (Li et al. 1988; Zandbergen et al. 1988).

There are several experimental clues regarding the faults reported in this section:

(1) They disappear under 300 keV electron irradiation but not 100 or 200 keV, see for instance Fig. 5.12.

(2) There are no extra spots in the c-axis electron diffraction patterns, although the streaks discussed in 5.5 are present.

(3) There are no B/W defects in these areas.

(4) The faults are visible in (200) and (020) dark-field images. However, there are two sets of faults; one set is visible using the (200) and invisible using the (020) and vice-versa for the other set. Both sets are visible in (110) dark-field images.

(5) The dark-field image contrast of some faults is unchanged when a twin boundary is crossed.

(6) These faults were not found in dark-field images down the a- or b-axes; this observation, however, is somewhat statistically limited.

(7) Both the densities and sizes of the faults are similar in the two proton fluences studied, namely, $6x10^{15}$ $H^+ \cdot cm^2$ and $3x10^{16}$ $H^+ \cdot cm^2$. The faults in the lower fluence, however, are slightly larger and more dense, which is

Figure 5.12 c-axis dark-field images of stacking faults in YBCO irradiated to a fluence of $3x10^{16}$ $H^{+}\cdot cm^{-2}$ with 3.5 MeV protons. (a) 100 keV electron energy (b) 300 keV after 1 hour. The faults disappeared with time at 300 keV.

Figure 5.13 (200) and (020) c-axis dark-field TEM images (100 keV electrons) of the same region of a YBCO crystal irradiated to a fluence of $6x10^{15}$ $H^{+}\cdot cm^{-2}$ with 3.5 MeV protons.

consistent with the electron irradiation destroying the faults [clue (1)], i.e., the higher proton dose may have partially destroyed the faults. This suggests the faults are as-grown structures.

(8) EDS analysis did not show the presence of any impurities, e.g., rare earth elements which are known to substitute onto the Y site with very little change in either the structure or properties (Fisk et al. 1987).

The electron diffraction patterns do not contain any extra reflections which indicates the structure of the defects is commensurate with YBCO (at least down the c-axis). This is consistent with the defect being a stacking fault. Recall that stacking faults were not found in YBCO crystals grown in Au crucibles. This may be the result of the Au impurity related defects (see Chap. 3) acting to prohibit the formation of stacking faults during crystal growth.

The existence of simple stacking fault structures in polycrystalline YBCO with fault displacement vectors of the type $\mathbf{R} = 1/6[301]$ has been reported (Tafto, Suenaga, and Sabatini 1988). HREM studies of such faults have demonstrated that these faults are extrinsic in nature, suggesting that the faults result from the insertion of an extra CuO_2 plane (Li et al. 1988; Zandbergen et al. 1988). This assumption was directly confirmed by a high-resolution Z-contrast imaging experiment in a scanning transmission electron microscope (Pennycook 1990) and further verified with EDS and EELS (Dravid et al. 1992). A report by Ringnalda et al. demonstrated that the faults are CuO_2 planes inserted with a half unit cell shift in either the a or the b direction and either adjacent to the CuO_2 superconducting plane or the CuO chain plane, referred to as type-1 and type-2 respectively (Ringnalda et

al. 1994). For type-1 faults [301] is equivalent to [031]; hence, **R** will switch across a twin boundary. Note that this symmetry does not hold true for type-2 faults. The visibility criteria in a dark-field image is that **g**·**R** does not equal zero; this explains experimental clues (4) and (5) listed above. First there were two sets of faults one visible with **g** = 020 and the other with **g** = 200 and both visible with **g** = 110. This is readily explained by inspection of **g**·**R** for each of these three imaging conditions. It also justifies faults which cross over twin boundaries without a change in the dark-field image contrast, as both **g** and **R** will switch across the boundary, e.g., (200) becomes (020) and 1/6[031] becomes 1/6[301], thereby maintaining the visibility criteria.

The possibility that the defects are surface artifacts had to be examined. This seems unlikely in light of a two experimental facts: (1) The gray level in the dark-field images of the different faults varies from black to white with many levels of gray in between, indicative of defects lying at different depths in the thin foil; (2) Moiré patches are seen overlapping the faults. It is generally assumed that the Moiré fringes result from surface decomposition into various oxides; hence, if the surface has these oxides then the faults must lie beneath the surface.

It is not clear if these faults are as-grown or formed under the proton irradiation. The absence of B/W defects could be explained under either scenario. If as-grown, then the faults act as sinks for the irradiation induced Cu and O interstitials. If formed under the proton irradiation, then the faults may simply be much larger agglomerates of the irradiation induced point defects and hence include the defects that otherwise would have formed the B/W defects. The quantity of point defects produced by proton

irradiation should be insufficient to create stacking faults this large and locally dense, refer to Table 5.1, which supports the notion that the defects are an as-grown structure.

5.7 Discussion

This chapter presented some new and interesting data regarding the defects found in proton irradiated YBCO. While there are several new experiments that still need to be performed as well as obtaining more observations of the phenomena presented in this chapter, the author was unable to pursue them due to the rather limited supply of YBCO crystals grown in ZrO_2 crucibles, which was not under the author's control.

It would be interesting to understand the flux pinning discrepancy (both pre- and post-irradiation) between YBCO single crystals grown in Au crucibles versus ZrO_2 crucibles. In light of all the defects present, however, this seems a rather daunting task. The size of defects ranges from point defects to 100 nm stacking faults with a non-homogeneous distribution, and to further complicate matters, the type of defect can be dramatically altered by the electron beam. This makes it difficult to associate the magnetic flux pinning properties with a specific defect structure. It is very easy to hypothesize all sorts of models that fit with parts of the data. Unfortunately, there always seems to be a data point or two that is unexplained. It seems clear that many point defects are created by proton irradiation and may coalesce either over time at room temperature or under the influence of high energy electrons. A few of the defects seen are of the appropriate size and density to be considered as strong flux pinning defects.

The presence of stacking faults surprised the crystal growers sufficiently that they checked their records and found they had been slowly using a greater fraction copper in the melt so that larger crystals could be achieved. This explains the presence of the stacking faults, but unfortunately the flux pinning data on YBCO grown in ZrO_2 crucibles is from crystals grown from melts with a lower Cu concentration, and thus is not easily correlated to these Cu-rich YBCO crystals. The following paragraph is based on the speculation that the ZrO_2 grown YBCO has similar post-irradiation values of J_c regardless of the Cu concentration in the melt. This could be a very poor assumption and certainly warrants further investigation, see 7.4.

YBCO crystals grown in ZrO_2 crucibles with lower Cu concentrations in the melt exhibit superior post-irradiation flux pinning at 70 K over Au grown YBCO. In light of the defects observed (Cu-rich YBCO), this might support the hypothesis that point defect are the primary pinner. This is because there are no B/W defects in the regions containing stacking faults and only point defects. Note that the results of the annealing experiment, presented in 5.4.3, suggest that the defects responsible for the post-irradiation enhancement in J_c are thermally recovered at 100 to 300 °C. Both individual point defects as well as point defect clusters (B/W defects) are recovered; hence, this experiment does not differentiate between the two defect types, but it does support the theories that one of these two defect types or a combination of the two is responsible for the enhanced J_c.

5.8 Conclusion

The investigation of irradiation induced point defects, some species of which may migrate and coalesce into larger defects, is a very difficult task and in the presence of many pre-irradiation point defects and non-homogenous extended defects produces confusing and conflicting results. This chapter does not provide the final word on the defect structures in proton irradiated YBCO, but does present some new defects as well as confirm several aspects of defects previously reported.

Three types of defects were reported; 3-4 nm diameter platelets (possibly CuO) in the b-c plane, point defects which cluster under the influence of the electron beam at high voltages, and stacking faults probably extrinsic in nature and consisting of an extra CuO chain plane inserted parallel to the basal plane. The electron beam induced point defect clustering was found to be common to areas with either the platelets or the stacking faults, however, no region containing both stacking faults and platelets was found.

Chapter 6 | CHEMICAL DOPING OF Hg-BASED SUPERCONDUCTORS

A remarkable enhancement of flux pinning behavior achieved by chemical substitution in $HgBa_2Ca_{n-1}Cu_nO_{2n+2+\delta}$ compounds has recently been reported (Shimoyama et al. 1994). In earlier experiments it had been found that substitution of Cr (and later Re) on the Hg site enabled the synthesis of $(Hg,Cr)Sr_2CuO_{4+\delta}$, where all of the Ba had been replaced by the smaller Sr ion (Shimoyama et al. 1994). These new Sr-substituted compounds were initially of interest because of their improved chemical stability. It was later realized that these new materials exhibited better flux pinning properties than the Ba-containing compounds (Shimoyama et al. 1994). This behavior was attributed to the decrease in the interlayer distance, i.e., the thickness of the blocking layer between CuO_2 planes, resulting from smaller Sr ions. Decreasing this distance would be expected to increase flux pinning by increasing the coupling between pancake like vortices to form vortex lines (Gray and Kim 1991).

6.1 Chemical Modulation in $Hg_{1-x}Cr_xSr_2CuO_{4+\delta}$

In this section, the structure of an incommensurate chemical modulation in the solid-solution compound $Hg_{1-x}Cr_xSr_2CuO_{4+\delta}$ (for $x \approx 0.4$) is reported, as determined by neutron-powder-diffraction, electron diffraction, and lattice imaging. The local structures around Cr and Hg

atoms are sufficiently different that a refinement of the average structure provides a clear picture of the distortions resulting from the incorporation of Cr. Electron diffraction and HREM show how Cr- and Hg-rich regions order in all three crystallographic directions to form a supercell of approximate dimensions 5ax5ax2c. Cr is incorporated in the form of CrO_4 tetrahedra, resulting in a dramatic lengthening of the corresponding Cu-O apical bond to 0.313 nm. Thus the CrO_6 octahedra of the ideal $HgBa_2CuO_{4+\delta}$ structure are, in effect, replaced by CuO_5 pyramids that either point up or point down as dictated by the supercell ordering.

The work presented here is the result of an analysis based upon neutron diffraction, electron diffraction, and HREM, and is published elsewhere (Chmaissem et al. 1995). It should be noted that Dr. Jorgensen's group was responsible for the materials synthesis as well as the neutron-powder-diffraction analysis, while Prof. Marks' group was primarily responsible for the electron microscopy [excluding chemical analysis of the Sr containing compound (performed by Prof. Dravid's group)]. Both groups (Jorgensen and Marks), however, were equally involved in generating a structural model which works equally well for both the local- and long-range order found experimentally. Hence, while the neutron-powder-diffraction data and analysis were not performed by the author, they are included here as they are an integral part of the final model, which electron microscopy alone cannot explain.

6.1.1 Neutron Powder Diffraction

Neutron-powder-diffraction measurements were performed at ANL, and analyzed by the Rietveld technique over the d-spacing range 0.05-0.4 nm. Since no supercell reflections were visible in the neutron-powder-diffraction data, the average structure (i.e., superposition of cells containing either Cr or Hg) was refined, with partial occupancies for the sites associated with Cr and Hg local environments. This technique provides useful information in the present case because the local structures in the vicinity of Cr and Hg are sufficiently different to be resolved using the neutron-powder-diffraction data. $SrCuO_2$ and $SrHgO_2$, which appear in small concentrations, were included as impurity phases in the Rietveld refinement. Refined values of the widths of the diffraction lines were comparable to the instrument resolution, suggesting no significant strain or particle size broadening.

It was found that Cr substitutes for Hg (as expected), but the Cr atoms are displaced from the ideal (0,0,0) site along the <100> direction. This displacement allows the Cr atom to achieve a tetrahedral coordination to four oxygen-atom neighbors. Two of these neighbors are the original apical oxygen atoms [O(2)], see Fig. 6.1, which are displaced to a new (x,0,z) site O(2)′, to form the appropriate bonds to Cr. Interstitial oxygen [O(3)] provides the other two oxygen atoms for the tetrahedron around Cr. These O(3) oxygen atoms are also displaced from the ideal interstitial (1/2,1/2,0) site, along the <110> direction to an (x,x,0) site (with $x \approx 0.372$) to achieve appropriate bond lengths to Cr. Each Cr atom pulls enough interstitial oxygen [O(3)] into the structure to achieve tetrahedral coordination to oxygen. The fraction of displaced apical oxygen atoms, n[O(2)′], is nominally equal to the number of

interstitial oxygen atoms, n[O(3)]. One might expect n[O(3)] > n[O(2)'] since additional oxygen may be required to create carriers in the CuO_2 planes. Such a difference is observed, but the error bars are not small enough to assign any physical significance to this observation. The local structure around the Cr site is illustrated in Fig. 6.1.

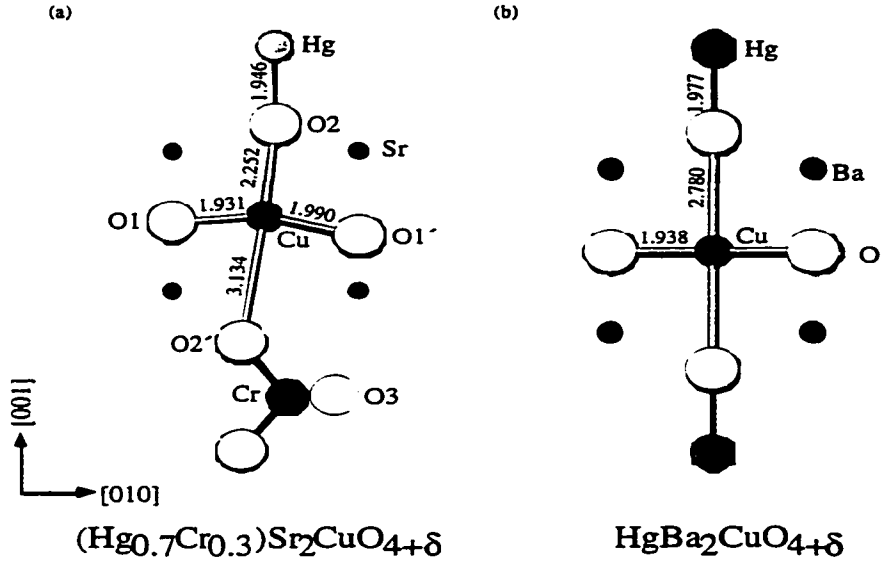

Figure 6.1 (a) Proposed local structure for $Hg_{1-x}Cr_xSr_2CuO_{4+\delta}$ based on the refinement of an average structure model of the fundamental cell dimensions using neutron-powder-diffraction data. Cr atoms achieve tetrahedral coordination by displacing the apical oxygen atoms to a new site [O(2)'] and incorporating two additional oxygen atoms per Cr atom at the in-plane site O(3). The coordinated tilting of CuO_6 octahedra and spatial constraints on the placement of O(3) atoms tends to produce the local Cr ordering shown. Bond lengths are in Å units. (b) The ideal structure of $HgBa_2CuO_{4+\delta}$ (Wagner et al. 1993) is shown for comparison.

In modeling a structure such as this, in which atoms are displaced from their ideal (high-symmetry) sites, multiple new sites are produced. In the actual structure only one of these sites can be occupied, since the multiple sites are typically too close together to allow simultaneous occupation. Thus the actual local structure violates the symmetry of the

average structure being used as a refinement model. A combination of Cr, O(2)′, and O(3) sites that defines a nearly perfect CrO_4 tetrahedron was selected, as shown in Fig. 6.2. This configuration together with the short Cr-O bond lengths suggest that Cr is in the +6 state.

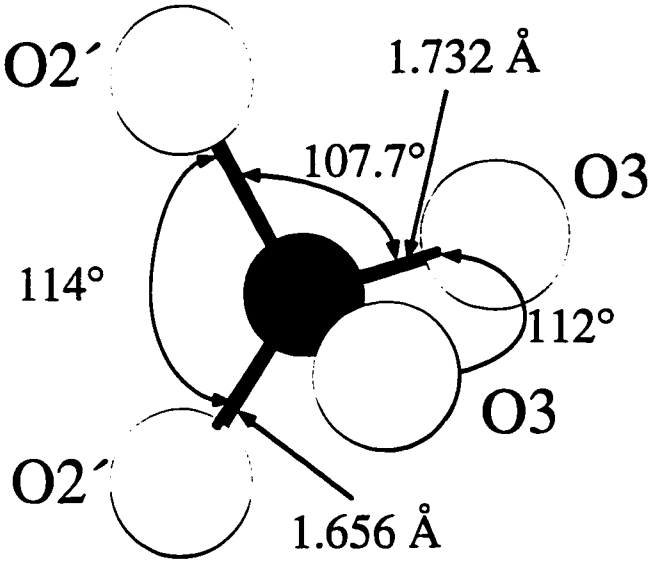

Figure 6.2 Bond lengths and angles between Cr and its surrounding oxygen atoms. A near perfect tetrahedron is formed.

6.1.2 HREM and Diffraction Results

Although the neutron-powder-diffraction data are analyzed in terms of the basic $HgBa_2CuO_{4+\delta}$ tetragonal unit cell, electron-diffraction measurements done on the same samples show that the actual structure is a supercell of approximate dimensions 5ax5ax2c. The supercell reflections are clearly defined in the electron-diffraction data and were always found in the diffraction patterns along the right zones (for instance, <110>, <111>, etc.). Hundreds of grains have been checked; no other superlattice was found. Even though these superlattice spots are not visible in the neutron-powder-diffraction data (signal to noise ratio is lower for neutron diffraction

compared to electron diffraction), a fairly detailed picture of the actual structure emerges by combining the electron diffraction results with what is learned about the local structure from neutron diffraction. Before continuing I would be remiss if I did not specifically acknowledge Dr. Zhang, for although I was integral in the TEM sample preparation, experimental microscopy, and image interpretation, she alone was responsible for the computer modeling of this large superstructure.

Electron diffraction patterns for the major zone axes: <001>, <100>, and <110> are shown in Fig. 6.3. All diffraction patterns will be indexed based on the unit cell. Sharp modulated reflections exist along $g_{1/5\ 1/5\ 1/2}$ and $g_{1/5\ -1/5\ 1/2}$ for all of the <110> patterns observed. The modulation was only found close to $g_{1/5\ 1/5\ 1/2}$ or $g_{1/5\ -1/5\ 1/2}$, as such it was also observed in the <301>, <112>, and <111> zone axes, but not in the <100> and <001> zone axes. The modulation is actually incommensurate with the reflections lying along $g_{1/4\,91/4\,91/2}$; for simplicity, $g_{1/5\,1/5\,1/2}$ will be used to approximate it. The presence of reflections along both $g_{1/5\ 1/5\ 1/2}$ and $g_{1/5\ -1/5\ 1/2}$ combined with the lack of a twin structure in <110> HREM images require the modulation to be in both directions.

Based on the neutron diffraction analysis, which showed a near 50% Cr doping for Hg, a chemical ordering was assumed in modeling the modulation. A 5ax5ax2c supercell was used to approximate the incommensurate modulation with a cosine squared wave to model the Cr occupancy:

$$\alpha\{\cos^2[2\pi(x+y)] + \cos^2(2\pi(x-y)]\} \qquad 6.1$$

$$1-\alpha\{\cos^2[2\pi(x+y)] + \cos^2[2\pi(x-y)]\} \qquad 6.2$$

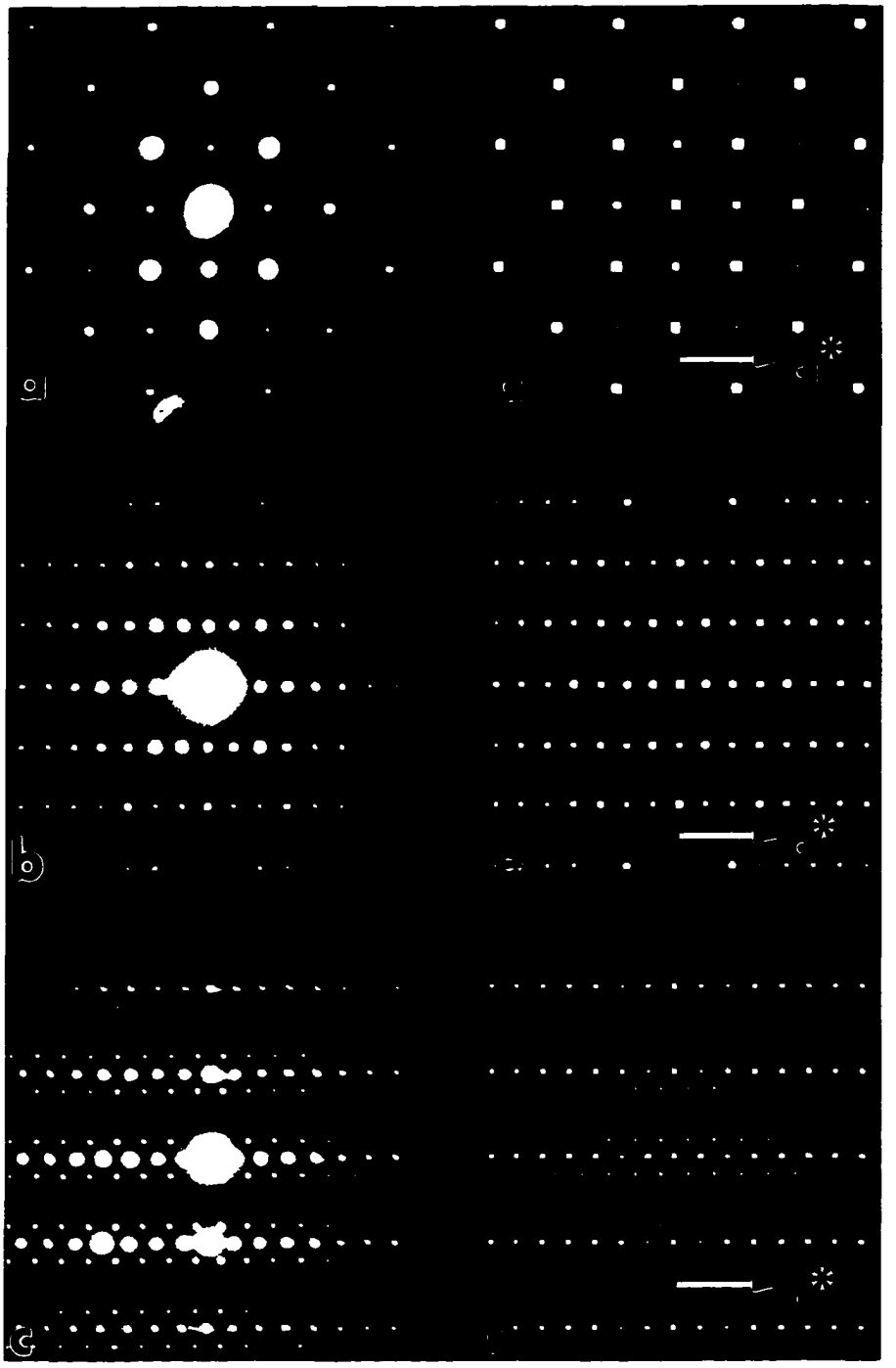

Figure 6.3 Experimental electron diffraction patterns for the <001>, <100>, and <110> zone axes (a)-(c). Corresponding multislice simulations of the model in Fig. 6.4. reflections due to the modulation are evident in the ,110 zone axis (c) and (f) and are forbidden in the <001> and <100> (a), (b), (d) and (e).

where x and y are along [100] and [010] respectively and α is one for 50% Cr.

A cosine squared wave is justified by the rapid dampening of the higher order modulated reflections in the diffraction patterns, see for instance, Fig. 6.3(c). The Cr and Hg compositions for the two different layers are illustrated in Fig. 6.4(a)-(b), where the Hg occupancy is one minus the Cr occupancy on any given cation site. While the neutron data provides detail regarding the oxygen ordering, no modeling was attempted as the small electron scattering factor of oxygen makes it difficult to detect. The shifting of the Cr, predicted by the neutron data analysis was also not modeled, instead a random Cr shift in <100> was approximated by a relatively large Debye-Waller term. Simulated electron diffraction patterns are shown in Figs. 6.3(d)-(f) for each of the experimental zone axes presented in Figs. 6.3(a)-(c); a good match was obtained for each.

Because there is little phase information in a diffraction pattern, any structural model constructed from diffraction patterns must be verified with HREM. Figure 6.5 shows a <110> HREM image with an inserted multislice simulation based on the model in Fig. 6.4. The simulation provides a good visual fit with the experimental image. Such a fit should generally be considered insufficient without strong supporting data, namely, the electron and neutron diffraction analysis. Simpler structures may be quantitatively refined for the atomic positions (Zhang et al. 1995); the modulation presented here, however, is currently too large and complicated for this method. The modulation is evident by the broad fringes in the (225) and (2-25) planes. HREM of the [100] and [001] axes show the basic undoped

structure, this is because the modulated reflections are forbidden in these zone-axes as the modulation is body-centered.

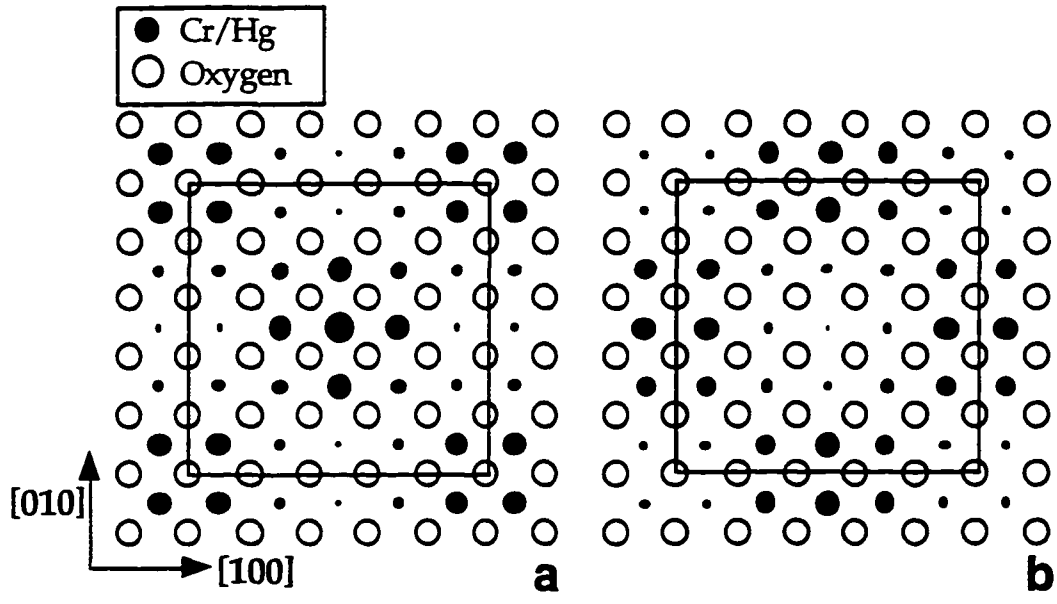

Figure 6.4 Average occupancy of Cr atoms at Hg sites for two alternating Hg-O planes along the [001] axis. The occupancies in (a) and (b) are determined by Eqs. 6.1 and 6.2 respectively. The sizes of the solid circles are proportional to the Cr fractional occupancies. The Hg occupancy is one minus the Cr occupancy.

Evidence for chemical disorder can be seen in the c-axis diffraction pattern, see Fig. 6.6. Although the modulated reflections are forbidden in the ZOLZ of the [001] zone axis, weak diffuse reflections are present at the Bragg locations of the modulation. The modulation has allowed Bragg reflections in the FOLZ and strong sharp reflections are evident. Calculations show the FOLZ to be 1.75 nm^{-1} along c* which clearly shows the doubling of the c-axis. Several other zone axes, e.g., [100], in which the modulated reflections are also forbidden show similar diffuse intensity resulting from the chemical disorder.

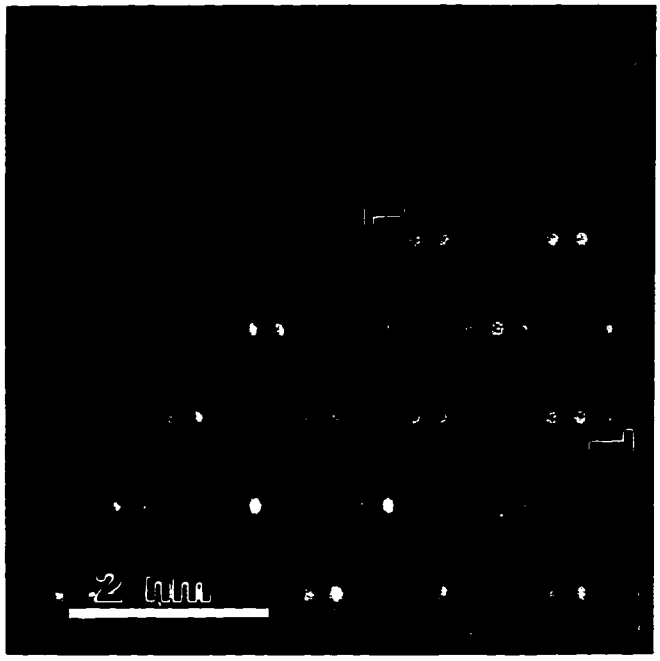

Figure 6.5 A <110> zone axis HREM image with an inserted multislice image simulation, based on the model presented in Fig. 6.4.

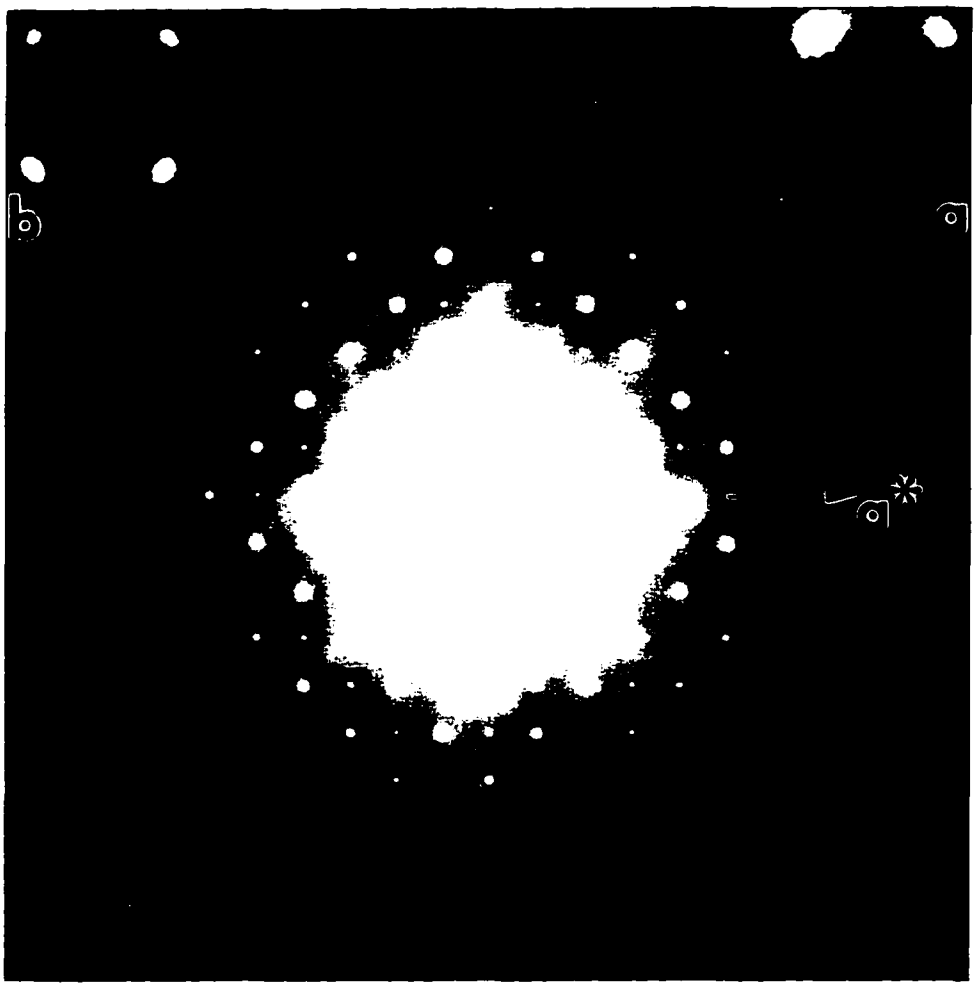

Figure 6.6 A much longer exposure of the <001> pattern in Fig. 6.3(a) shows diffuse intensity and the FOLZ. Chemical disorder is indicated by the presence of diffuse intensity at the forbidden Bragg locations for the modulation in the ZOLZ, inset (b). The Bragg reflections for the modulation are allowed in the FOLZ and are easily seen as sharp spots, inset (b).

Quantitative x-ray microanalysis in an analytical electron microscope (Hitachi HF-2000) was utilized in conjunction with standards for composition determination. Sensitivity factors (*k* factors) were obtained from $SrHgO_2$, $SrCuO_2$, and $SrCrO_4$ compounds. The overall cation composition is indicated in Table 6.1. These measurements indicate a Cr concentration of 0.38(3) atoms per formula unit. This is consistent with the observation of $SrCuO_2$ and $SrHgO_2$ as minor impurity phases, suggesting a Cr concentration higher than the starting composition (0.3). Site occupancies obtained from the Rietveld refinement of neutron-powder-diffraction data can also be used to estimate the Cr concentration, but these can be subject to systematic errors when nonharmonic static displacements are present in the structure [as is certainly true for the Hg and O(2) atoms]. The average of Cr, O(2)′, and O(3) occupancies from the refinement suggest a Cr content of about 0.42, in reasonable agreement with the x-ray microanalysis. We conclude that the Cr content is near 0.4. Unsuccessful attempts to form other compositions with different Cr concentrations suggest that Cr may not form a continuous solid-solution in the compound.

Table 6.1 Quantitative x-ray microanalysis of $Hg_{1-x}Sr_2CuO_{4+\delta}$. The numbers are normalized to two Sr atoms per unit cell.

Element	Nominal composition	Chemical analysis
Hg	0.7	0.73(3)
Cr	0.3	0.38(3)
Sr	2	2
Cu	1	1.04(8)

6.1.3 Discussion and Conclusion

A simplified picture of the supercell structure is that Cr-rich regions of dimensions 2.5ax2.5ax1c (0.96x0.96x0.87 nm^3) alternate in all three dimensions with the Hg-rich regions (which have a nearly normal $HgBa_2CuO_{4+\delta}$ structure except for the shortened Cu-O apical bond). Perpendicular to the <001> axis, distorted CuO_2 planes mark the boundaries between these regions. Because the apical Cu-O bond in the direction of Cr is elongated to 0.313 nm while that in the direction of Hg is shortened to 0.225 nm, the conduction plane is best viewed as consisting of CuO_5 pyramids (pointing towards Hg) rather than CuO_6 octahedra. These pyramids point up or down in accordance with the supercell.

The local structure, obtained from neutron-powder-diffraction, provides important insight concerning why the superstructure forms. The cell doubling along the c-axis occurs because of the tendency for Hg and Cr to alternate along this direction. A local structure in which Cr is present both above and below the same Cu atom is energetically unfavorable because it requires the Cu atom to be in square planar coordination (nominally Cu^{+3}) rather than pyramidal or octahedral coordination. The size of Cr clusters in the a-b plane is limited by frustration effects involving O(3) oxygen atoms, as illustrated in Fig. 6.7. Each Cr atom is bonded to two O(3) atoms in the plane. This places constraints on the orientation of CrO_4 units as the size of the cluster grows. At a cluster size of two or three fundamental unit cell dimensions, it is no longer possible to add additional CrO_4 units. Figure 6.7 shows only one layer, but the problem becomes even more constrained when the next layer along the c-axis is considered, where, for 50% Cr content,

CrO_4 units are located above Hg atoms in the first layer. From these considerations we can see that frustration in the orientation of CrO_4 units limits the cluster size to about 2.5 cell dimensions, in agreement with the supercell observed by electron diffraction. Additionally, we can conclude that the solubility for Cr is likely to be less than 50%. We also see that considerable disorder, resulting from different ways to orient individual CrO_4 units, will be present in the supercell.

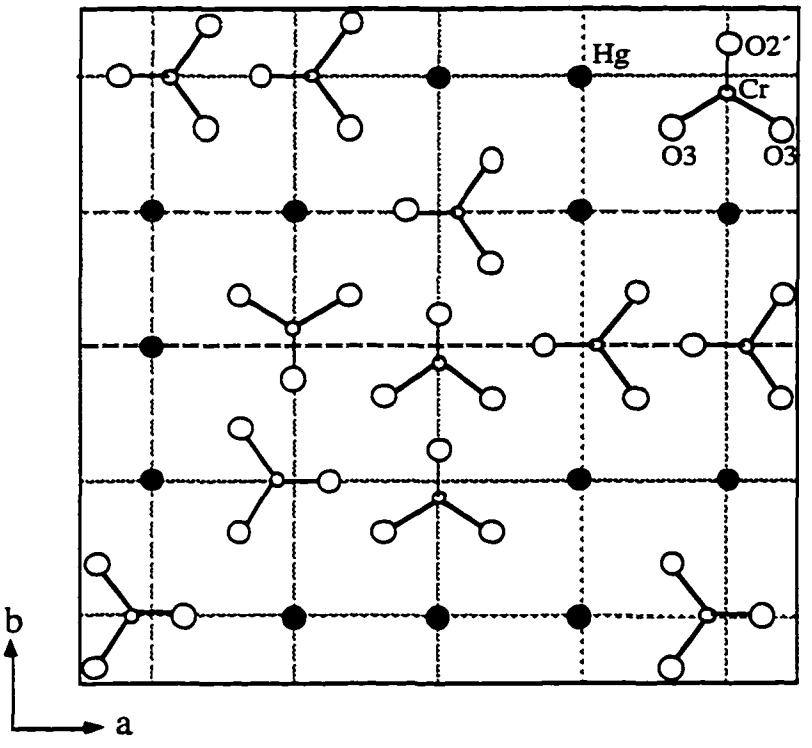

Figure 6.7 Representation of one layer of the a-b plane of $Hg_{1-x}Cr_xSr_2CuO_{4+\delta}$ showing a possible arrangement of CrO_4 units on the available sites to form a cluster that agrees with the probability illustrated Fig. 6.4(b). Frustration of the orientation of CrO_4 units requires disorder in the cluster and limits cluster size.

From the structural features determined in this study, it is not clear why this solid-solution compound should exhibit enhanced magnetic flux

pinning. The Cr- and Hg-rich regions are smaller than typical magnetic vortex dimensions and are regularly arranged in the crystal. Thus the average superstructure does not define any strongly preferred location for a vortex. If extended defect formation contributes to flux pinning, it must involve defects in the superstructure. Since the supercell is necessarily disordered, extended defect formation is likely. Such defects, however, were not evident in this work.

The ability to enhance magnetic flux pinning by chemical substitution could have important consequences for the application of copper-oxide superconductors. The results of this study suggest that structural modifications in which clustering and extended defects occur should be investigated. A troublesome side effect is that such defects can significantly distort the CuO_2 plane and may substantially lower T_c. The highest T_c's are thought to be achieved for flat CuO_2 planes and long Cu-O apical bonds, as are present in the $HgBa_2Ca_{n-1}Cu_nO_{2n+2+\delta}$ compounds (Radaelli et al. 1993; Wagner et al. 1995; Wagner et al. 1993). The effect of distortions of the CuO_2 plane have been studied in $La_{2-x}M_xCuO_4$ (M=Sr, etc.) compounds, where Tc decreases systematically as the tilt angle of the CuO_6 octahedra increases (Takahashi et al. 1994). One would like to enhance flux pinning as much as possible while minimizing the decrease in T_c caused by the chemical substitution. Thus, in future work, it will be important to investigate the structural effects of different chemical substitutions and the effects of varying the defect concentration, especially in the dilute limit.

6.2 Chemical Analysis of $Hg_{1-x}Cr_xBa_2CuO_{4+\delta}$

This section is included even though the author's involvement was limited to performing the EDS analysis (using a Philips CM30 at ANL) and to determining the absence of any chemical modulation [unlike the case for Cr doping of the Sr-containing compound (see 6.1)]. Given the author's minimal involvement, this section contains only the direct results obtained by the author and the corresponding compositions as determined by neutron-powder-diffraction. For further details regarding this work, the reader is referred elsewhere (Chmaissem et al. 1996).

Quantitative EDS was used to determine the amount of Cr in $Hg_{1-x}Cr_xBa_2CuO_{4+\delta}$, where the nominal values of x include: 0.1, 0.2, 0.3, and 0.4. There are many factors that one must consider to ensure that an accurate spectrum is collected; several of these details are mentioned below, for further information see (Joy, Romig, and Goldstein 1986). (1) The count rate was typically between 500 and 2000 counts per second yielding a low (10-30%) dead time. (2) A holey-carbon film on a Mo TEM grid was used to support the sample particles. While this ensures that the Cu signal is not from the grid there are other sources of Cu in a TEM and these must be accounted for as well. Fortunately, there were various oxide particles that did not contain any Cu but had similar densities to $Hg_{1-x}Cr_xBa_2CuO_{4+\delta}$. These particles did not show the presence of Cu, indicating the spectra of interest were free of spurious Cu x-rays. (3) The total collection time was approximately 150 live seconds, which produced about 5000 counts under the FWHM for the peaks of interest. Under these circumstances, the relative counting error is 2.8% at

the 95% confidence level (Joy, Romig, and Goldstein 1986). A typical EDS spectrum is presented in Fig. 6.8.

An undoped, i.e., Cr free, sample was used to determine the *k* factor for the Hg L_1 to Cu K_α peak. The *k* factor was obtained by collecting several spectra from the Cr free compound and applying the Cliff-Lorimer relation (Cliff and Lorimer 1975):

$$\frac{C_{Hg}}{C_{Cu}} = k_{HgCu}\left(\frac{I_{Hg}}{I_{Cu}}\right) \qquad 6.3$$

where C is the composition and I is the total intensity under the FWHM of the characteristic x-ray peak. Note that Eq. 6.3 is for a thin film approximation, i.e., absorption and fluorescence are negligible; the use of this approximation is called into question later. For the standard sample C_{Hg} = C_{Cu} = 1; hence k_{HgCu} is simply I_{Cu} divided by I_{Hg}. A mean value from several crystals was obtained, and the standard error (standard deviation divided by the square root of the number of measurements) was used as an error on the mean value of k_{HgCu}. Similarly, k_{HgBa}, k_{CuBa}, and k_{BaCu} were determined.

Approximately ten crystals were sampled for each Cr stoichiometry so that an average Hg to Cu intensity ratio could be obtained. Assuming C_{Cu} to be one, then C_{Hg} is simply k_{HgCu} times the average intensity ratio. The standard error for the product of two averages is determined as follows:

$$Std.Error = \left(\frac{\bar{X}^2\sigma_Y^2}{N_Y} + \frac{\bar{Y}^2\sigma_X^2}{N_X} + \frac{\sigma_X^2\sigma_Y^2}{N_X N_Y}\right)^{1/2} \qquad 6.4$$

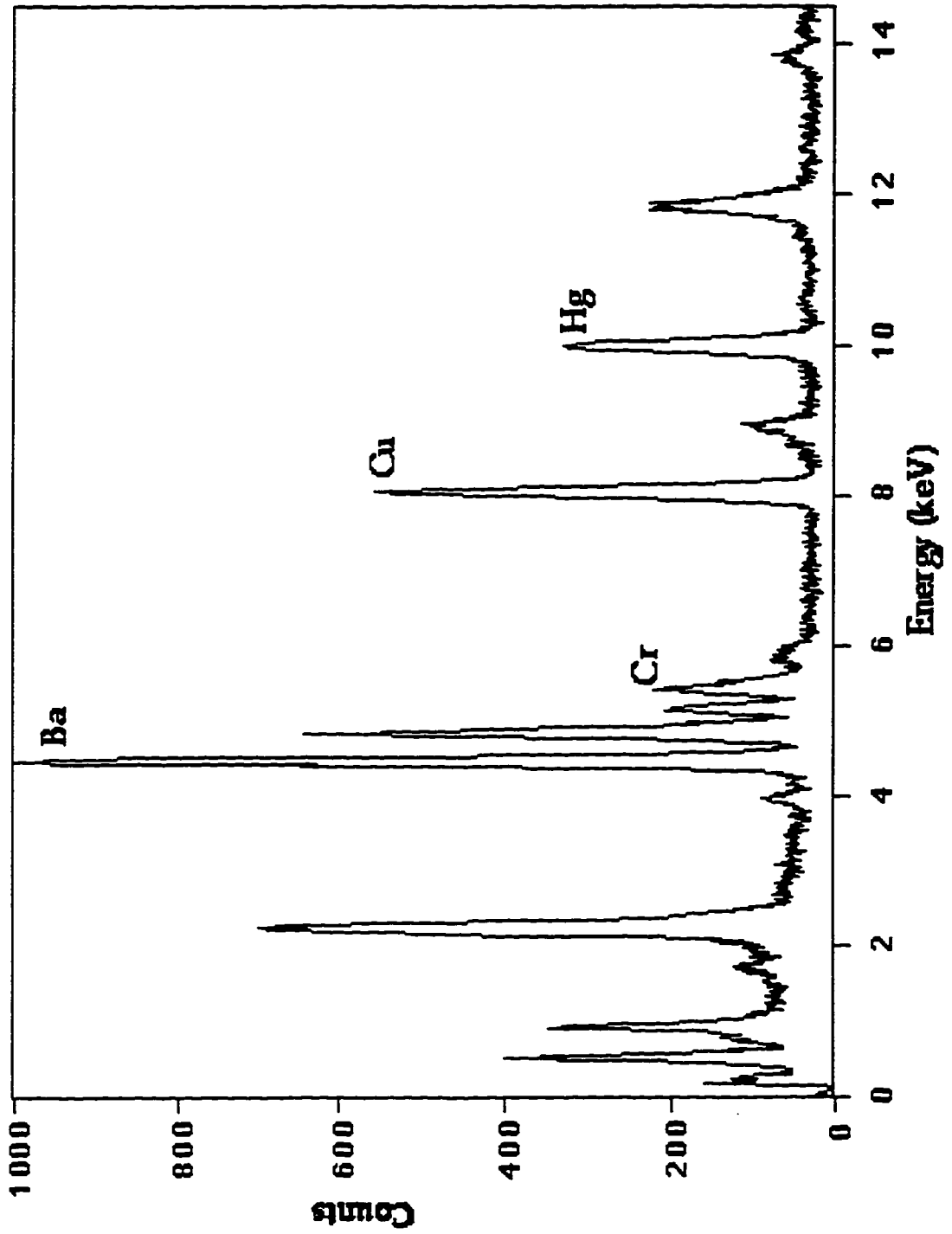

Figure 6.8 Typical EDS spectrum for the nominal doping of 0.4 Cr atoms per unit cell in $Hg_{1-x}Cr_xBa_2CuO_{4+\delta}$. The peaks used for the quantitative analysis are labeled.

where X and Y represent the two distributions, σ is the standard deviation, and N is the total number of counts. The standard error relates to the confidence of a mean value for a distribution. The results for this analysis are presented in Tables 6.2 and 6.3; the data in Table 6.2 is normalized to one Cu atom per unit cell and the data in Table 6.3 is normalized to two Ba atoms per unit cell. The two tables both show that the Cr composition increases to a solubility limit of 0.3 to 0.4 Cr atoms per unit cell. Note that the Cr composition is calculated as one minus the Hg composition, i.e., it is not measured directly. This is because the Cr Kα peak overlaps with one of the Ba L peaks.

Table 6.2 Quantitative x-ray microanalysis of $Hg_{1-x}Cr_xBa_2CuO_{4+\delta}$. The numbers are normalized to 1 Cu atom per unit cell.

	$Hg_{1-x}Cr_xBa_2CuO_{4+\delta}$ (nominal values of x = 0, 0.1, 0.2, 0.3, 0.4)				
Element	x = 0	x = 0.1	x = 0.2	x = 0.3	x = 0.4
Cr (= x)	0	0.20(2)	0.26(2)	0.31(2)	0.34(2)
Hg (= 1-x)	1	0.80(2)	0.74(2)	0.69(2)	0.66(2)
Cu	1	1	1	1	1
Ba	2	2.0(1)	2.3(1)	2.4(2)	2.3(1)

The problem with Table 6.2 is that Cu may be substituted on the Hg site, i.e., the standard may not be very reliable for Cu. This would push the Cu concentration up, and by normalizing to one Cu atom per unit cell the Hg stoichiometry (already low due to Cu substitution) would be forced lower. This results in the calculated Cr content (1-Hg) being larger than its actual

value. Similarly, the calculated Ba content would be expected to be less than two atoms per unit cell; however, it is larger than two for the larger Cr doping levels. This is explained by the Hg K_α x-rays fluorescing the Cu; hence, as Cr substitutes for Hg, less Cu is fluoresced and the intensity of the Ba, fluoresced by the Cr K_α x-rays, peak is enhanced relative to the Cu peak. This situation could arise if the crushed particle was very thick. Crushed powder tends to have extremely large wedge angles so that a slight sample drift might change the thickness to well over 100 nm. While fluorescence can explain the larger Ba content at higher Cr doping levels, the observed Ba content does not increase systematically with the Cr content.

Table 6.3 Quantitative x-ray microanalysis of $Hg_{1-x}Cr_xBa_2CuO_{4+\delta}$. The numbers are normalized to 2 Ba atoms per unit cell.

	$Hg_{1-x}Cr_xBa_2CuO_{4+\delta}$ (nominal values of x = 0, 0.1, 0.2, 0.3, 0.4)				
Element	x = 0	x = 0.1	x = 0.2	x = 0.3	x = 0.4
Cr (= x)	0	0.20(2)	0.36(2)	0.41(2)	0.41(2)
Hg (= 1-x)	1	0.80(2)	0.64(2)	0.59(2)	0.59(2)
Cu	1	1.00(2)	0.87(2)	0.86(3)	0.90(2)
Ba	2	2	2	2	2

The reason for generating Table 6.3 is that the Ba site is very likely to be fully occupied by only Ba; thus two Ba atoms per unit cell is a more reliable reference point than one Cu atom per unit cell. The decrease in Cu fluorescence coupled with the increased Ba fluorescence could explain the lowered Cu concentrations at higher Cr doping levels when in fact the Cu is possibly greater than one due to substitution on the Hg site.

The Cr compositions as determined by Reitveld refinement of the neutron-powder-diffraction data are provided in Table 6.4. Note that the Cr fraction per unit cell was determined by two methods. The first method was to hold the Hg plus Cr equal to one atom per unit cell. The other method was to infer the Cr from the interstitial oxygen concentration [O(3)]; two interstitial oxygen atoms were presumed to form a CrO_4 tetrahedron with two regular oxygen atoms.

Table 6.4 Cr compositions as determined by Rietveld refinement of neutron-powder-diffraction data (Chmaissem et al. 1996). Note that the following conditions were required in the refinement Ba = 2 and Cu = 1.

	$Hg_{1-x}Cr_xBa_2CuO_{4+\delta}$ (nominal values of x = 0.1, 0.2, 0.3, 0.4)			
	x = 0.1	x = 0.2	x = 0.3	x = 0.4
Cr if Cr+Hg = 1	0.215	0.352	0.431	0.420
Cr by O(3)	0.114	0.254	0.302	0.292

The Cr concentration was experimentally determined in five different manners. Four of these have been discussed (EDS with Cu = 1 or Ba = 2 and Reitveld refinement of neutron-powder-diffraction with Cr+Hg = 1 or Cr dependent on the interstitial oxygen concentration) the fifth was allowing the EDS software to use built in *k* factors to analyze the x-ray spectra. The results from these five methods are plotted in Fig. 6.9. It is clear that a saturation limit seems to be reached at a nominal composition of 0.3 Cr atoms per unit cell; the level of this saturation varies from 0.26 to 0.42. The quantitative EDS analysis with Ba = 2 produced nearly identical results with the Reitveld refinement in which Hg+Cr = 1. Coincidentally these two

methods also suggest a doping limit that matches the only Cr solubility obtainable in $HgSr_2CuO_{4+\delta}$ (see 6.1).

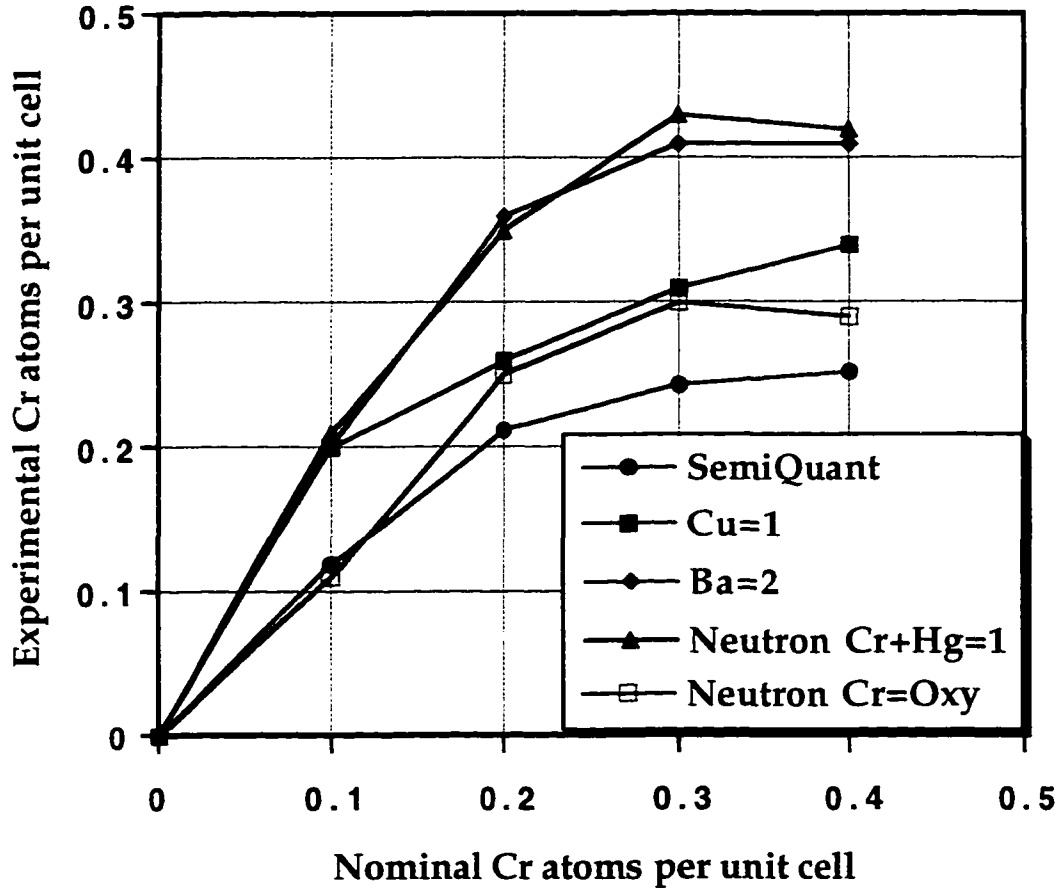

Figure 6.9 Cr concentration as determined in five different manners using both neutron-powder-diffraction (blue curves) and x-ray emission microanalysis (red curves). SemiQuant used the built in k factors, Cu = 1 and Ba = 2 utilized *k* factors determined from the undoped material and are normalized to Cu = 1 or Ba = 2.

Chapter 7 | Future Work

This thesis is no different than most in that it represents a work in progress. Several new paths are evident for future work; a few are described in the following pages.

7.1 Au-Doped YBCO

Chapter 3 showed that in YBCO Au forms small defect clusters with O vacancies or interstitials. Previous magnetic flux pinning work suggested that crystals doped with Au have an enhanced J_c compared to crystals free of cation doping. It would be of interest to dope pure YBCO single crystals with Au to various degrees and monitor J_c.

The undoped YBCO can be obtained by growing the single crystals in ZrO_2 crucibles; crystals grown in this manner have 1-2 ppm Zr substituted for Cu. Polycrystalline pellets can be doped up to 3 wt. % before the solubility limit is reached and Au precipitates form at the grain boundaries, while unproved, single crystals probably have a similar doping limit. Several concentrations of Au (at least up to 3 wt. %) should be attempted. The actual concentrations should be determined not only as a bulk average but also on local levels. Chemical analysis techniques that should be used include: neutron activation, EELS, EDS, and SIMS.

It will be very difficult to investigate the point defect clusters at low doping levels of Au, as it was rather difficult to do for 3 wt. %, see Chap. 3.

Indeed if the Au doping is very low there may be little or no clustering due to the long diffusion distances required. Off-zone electron diffraction patterns are probably the best way to look for evidence of point defect clusters.

7.2 Shape of Defect Cascades in YBCO

This project finds its audience not in the field of superconductivity, but rather, with those interested in the physics of irradiation damage. The idea here is to determine more precisely the shape of defect cascades in YBCO (or possibly other highly anisotropic materials) and correlate the shape with the anisotropic thermal conductivity. It seems likely that a model could be devised that would predict the shape of a defect cascade based on the thermal conductivity. Any model arrived at should be verified by irradiating a material with a different degree of anisotropy in thermal conductivity. There are a few areas of consideration; they are outlined below.

The irradiation direction in a given crystal must be known and controlled. This could be achieved by irradiating a large single crystal or thin film, i.e., not using a crushed, randomly dispersed sample. If the irradiation direction is not in the same direction as the imaging direction, then due to projection effects there will be a broadening in one direction as the defect cascade is elongated in the direction of the irradiation.

If a large thin area is obtained in the TEM sample, it would allow HREM to be used for the direct sizing of the defect cascades, which I believe is a more reliable method. More importantly, it provides unequivocally the aspect ratio for each defect cascade, as opposed to DF images which only yield

the size in one direction for a given imaging condition. Note that the HREM images should be taken near the optimal defocus so that image delocalization artifacts are avoided, see Appendix A.

In the modeling of the energy dissipation (cooling) the bulk thermal conductivity must be used for cooling that occurs very locally and over a 10^{-11} s time scale; this assumption may be highly inappropriate (I have no insight here). Estimation of the initial core temperature can be made; however, the initial radial temperature profile is more difficult.

7.3 Structure Surrounding a Defect Cascade

As a thermal spike cools, the disordered region recrystallizes. It is likely that this recrystallized material surrounding the amorphous defect cascade core contains a degree of disorder as well. If this is true then the relevant size of the magnetic flux pinning defect may be the diameter of this recrystallized region and not simply the amorphous core.

HREM might reveal the presence of a high point defect density surrounding the defect cascade. There may also be a significant degree of chemical disorder.

7.4 As-grown Stacking Faults in YBCO

If there are as-grown stacking faults in the YBCO crystals grown in ZrO_2 crucibles at UIUC, it would be quite interesting. First of all, these single crystals are assumed by many to be the best in the world and nearly free of even the smallest defects. As such many physics experiments probing the fundamentals of superconductivity are performed on these crystals under

the assumption that they are perfect. Secondly, much research is being done to create stacking faults (using both chemical and mechanical means) in high-temperature superconductors in hopes enhancing J_C. This might be ill-advised if there are stacking faults in these single crystals, because J_C is very low for these crystals. Finally, it appears that the stacking faults act as sinks for the point defects produced by proton irradiation damage; thereby prohibiting the migration and coalescence of the point defects. This alters the post-irradiation defect structure and consequently the flux-pinning enhancement.

The concentration of as-grown stacking faults should be controllable by the concentration of Cu used during the growth conditions. This could lead to a method of controlling whether the B/W defects (see Chap. 5) are present or not after irradiation, and by combining this with the corresponding J_C measurements, the pinning strength of the B/W defects might be discerned.

Appendix A | IMAGE DELOCALIZATION IN HREM IMAGES

It is important to be aware that in HREM images the apparent size of a small object is a function of defocus due to image delocalization (Marks 1984; Marks 1985). A through focal image simulation series of an amorphous region surrounded by a square lattice shows how the apparent size of a defect will change with defocus, Fig. A.1. This effect is particularly important in the study of small particles, defect cascades, interfaces, etc.

Periodicities in the sample with a certain frequency will be displaced from their true location in the image. The amount of image delocalization is equal to the gradient of the contrast transfer function (CTF).

$$\nabla X(u) = 2\pi\lambda(\Delta z u + C_S\lambda^2 u^3) \qquad \text{A.1}$$

where λ is the electron wavelength, u is a spatial frequency, C_S is the spherical aberration coefficient, and Δz is the objective defocus. The defocus at which there is no image delocalization is referred to as the overlap defocus, i.e., the image of the spacing in question overlaps it's true location in the image. The overlap defocus is found by setting Eq. A.1 equal to zero:

$$\Delta z = -\lambda^2 C_S u^2 \qquad \text{A.2}$$

The effect of delocalization is a major problem for defoci near 0 nm, indeed the structure of the defect may become extremely obscured, see for instance Fig. A.1 (b). Figure A.1 (b) to (i) were generated by applying a contrast transfer function using linear imaging theory to the sample or object in Fig. A.1 (a). Note the lattice fringes are not parallel to the edges of the image, so the effects seen are not aliasing artifacts. Besides the obvious fringes seen in the amorphous region there is also a curving of the lattice image towards the center. This could easily be seen in an experimental image and misinterpreted as an inwardly directed strain field, when it is merely an imaging artifact dependent on the defocus, e.g., it is not seen in Fig. A.1 (f).

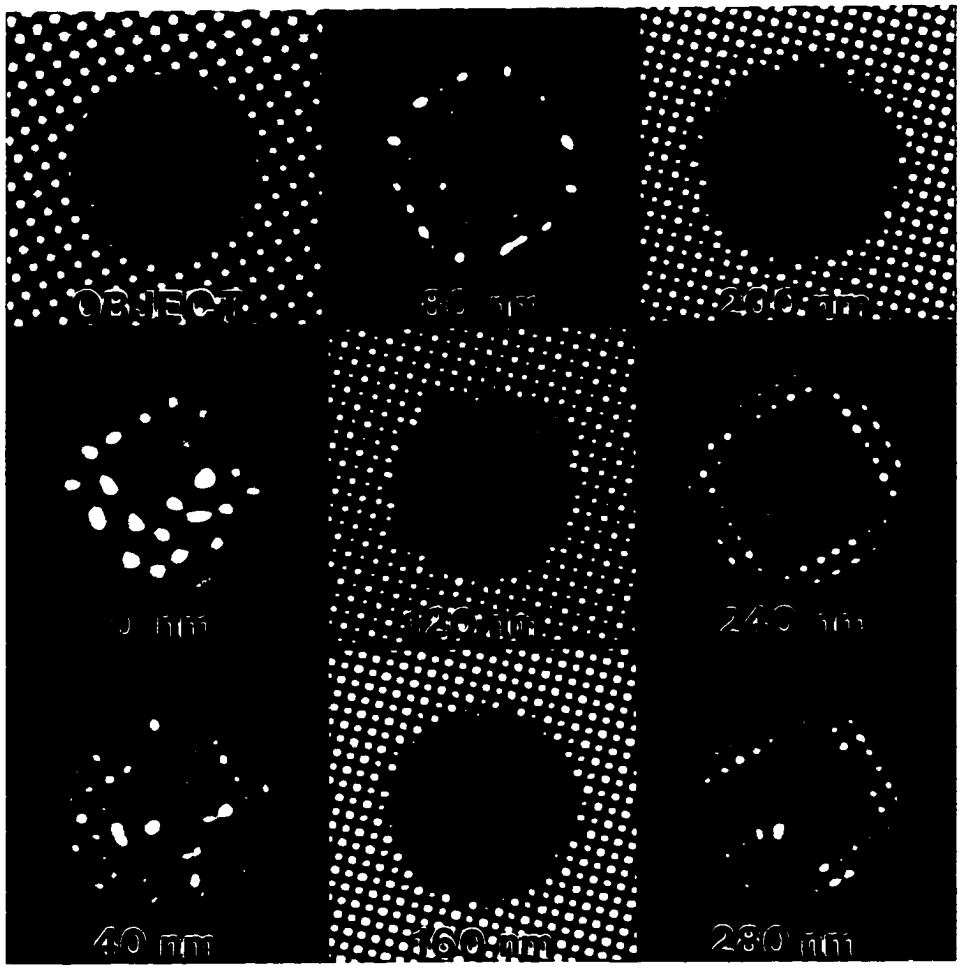

Figure A1 A simulated through focal series of the object in the top left corner (linear imaging theory). The object is intended to represent an amorphous cylinder surrounded by a square lattice; the lattice parameter is 0.385 nm. The objective defocus is indicated in each image. This series clearly shows two imaging artifacts dependent upon the defocus: the apparent size of the cylinder and a bending of the lattice fringes. Both of these effects are minimized at the overlap defocus (160 nm).

REFERENCES

Abrikosov, A. A. 1957. On the magnetic properties of superconductors of the second group. *Journal of Soviet Physics JETP* 5(6): 1174-1182.

Allen, C. W., L. L. Funk, E. A. Ryan and A. Taylor. 1989. In situ irradiation/implantation studies in the HVEM-Tandem facility at Argonne National Laboratory. *Nuclear Instruments and Methods B* 40/41: 553-556.

Anderson, P. W. and Y. B. Kim. 1964. Hard superconductivity: Theory of the motion of Abrikosov flux lines. *Review of Modern Physics* 36(1): 39-43.

Ashby, M. F. and L. M. Brown. 1963. Diffraction contrast from spherically symmetrical coherency strains. *Philosophical Magazine* 7: 1083-1103.

Bardeen, J., L. N. Cooper and J. R. Schreiffer. 1957. Theory of superconductivity. *Physical Review* 108(5): 1175-1204.

Basu, S. N., T. Roy, T. E. Mitchell and M. Nastasi. 1989. Electron beam induced oxygen disordering in $YBa_2Cu_3O_{7-x}$ superconductors. *Journal of Applied Physics* 69: 3167-3171.

Bednorz, J. G. and K. A. Müller. 1986. Possible high T_c in the Ba-La-Cu-O System. *Zeitschrift für Physik B-Condensed Matter* 64: 189-193.

Beyers, R., B. T. Ahn, G. Gorman, V. Y. Lee, S. S. P. Parkin, M. L. Ramirez, K. P. Roche, J. E. Vazquez, T. M. Gür and R. A. Huggins. 1989. Oxygen ordering, phase separation and the 60-K and 90-K plateaus in $YBa_2Cu_3O_x$. *Nature* 340: 619-621.

Brinkman, J. A. 1954. On the nature of radiation damage in metals. *Journal of Applied Physics* 25(8): 961-970.

Budhani, R. C., Y. Zhu and M. Suenaga. 1992. Effects of 300 MeV Au^{+24} ion irradiation on superconductivity in $YBa_2Cu_3O_7$ epitaxial films. *Applied Physics Letters* 61(8): 985-987.

Buseck, P. R., J. M. Cowley and L. Eyring, ed. 1988. High-resolution transmission electron microscopy. New York:Oxford University Press.

Cava, R. J., A. W. Hewat, B. Batlogg, M. Marezio, K. M. Rabe, J. J. Krajewski, W. F. P. Jr. and L. W. R. Jr. 1990. Structural anomalies oxygen ordering and superconductivity in oxygen deficient $Ba_2YCu_3O_x$. *Physica C* 165: 419-433.

Chen, N., S. J. Rothman, J. L. Routbort and K. C. Goretta. 1992. Tracer diffusion of Ba and Y in $YBa_2Cu_3O_x$. *Journal of Materials Research* 7(9): 2308-2316.

Chmaissem, O., D. N. Argyriou, D. G. Hinks, J. D. Jorgensen, B. G. Storey, H. Zhang, L. D. Marks, Y. Y. Wang, V. P. Dravid and B. Dabrowski. 1995. Chromium clustering and ordering in $Hg_{1-x}Cr_xSr_2CuO_{4+\delta}$. *Physical review B* 52(21): 15636-15643.

Chmaissem, O., T. Z. Deng and Z. A. Sheng. 1995. Synthesis and study of (Hg,Cr)-based 1201-type superconducting cuprate $(Hg,Cr)Sr_2CuO_{4+\delta}$. *Physica C* 242: 17-22.

Chmaissem, O., J. D. Jorgensen, B. G. Storey, H. Zhang and L. D. Marks. 1996. *In preparation* :

Chu, C. W., P. H. Hor, R. L. Meng, L. Gao, Z. J. Huang and Y. Q. Wang. 1987. Evidence for superconductivity above 40 K in the La-Ba-Cu-O system. *Physical Review Letters* 58(4): 405-407.

Cieplak, M. Z., G. Xiao, C. L. Chien, A. Bakhshai, D. Artymowicz, W. Bryden, J. K. Stalick and J. J. Rhyne. 1990. Incorporation of gold into $YBa_2Cu_3O_7$: Structure and T_c Enhancement. *Physical Review B* 42(10): 6200-6208.

Cieplak, M. Z., G. Xiao, C. L. Chien, J. K. Stalick and J. J. Rhyne. 1990. Unexpected effects of gold on the structure, superconductivity, and normal state of $YBa_2Cu_3O_7$. *Applied Physics Letters* 57(9): 934-936.

Civale, L., A. D. Marwick, M. W. McElfresh, T. K. Worthington, A. P. Malozemoff, F. H. Holtzberg, J. R. Thompson and M. A. Kirk. 1990. Defect independence of the irreversibility line in proton-irradiated Y-Ba-Cu-O crystals. *Physical Review Letters* 65: 1164-1167.

Civale, L., A. D. Marwick, T. K. Worthington, M. A. Kirk, J. R. Thompson, L. Krusin-Elbaum, Y. Sun, J. R. Clem and F. Holtzberg. 1991. Vortex confinement by columnar defects in YBa2Cu3O7 crystals: Enhanced pinning at high fields and temperatures. *Physical Review Letters* 67(5): 648-651.

Clem, J. R. 1992. Fundamentals of vortices in the high-temperature superconductors. *Superconductor Science and Technology* 5: S33-S40.

Cliff, G. and G. W. Lorimer. 1975. The quantitative analysis of thin specimens. *Journal of Microscopy* 103: 203-207.

de Fontaine, D., G. Ceder and M. Asta. 1990. Low-temperature long-range oxygen order in $YBa_2Cu_3O_x$. *Nature* 343: 544-546.

Dew-Houghes, D. 1974. Flux pinning mechanisms in type II superconductors. *Philospical Magazine* 30: 293-305.

Diaz de la Rubia, T., R. S. Averback, R. Benedek and W. E. King. 1987. Role of thermal spikes in energetic displacement cascades. *Physical Review Letters* 59(17): 1930-1933.

Dravid, V. P., H. Zhang, L. D. Marks and J. P. Zhang. 1992. Combined HRTEM, X-ray microchemical and EELS fine structure analysis of planar defects in $YBa_2Cu_3O_{7-\delta}$. *Physica C* 192: 31 34.

Eibschütz, M., M. E. Lines, W. M. Reiff, B. v. Dover, J. V. Waszczak, S. Zahurak and R. J. Felder. 1993. Direct measurement of gold valence change as a function of oxygen stoichionetry in $YBa_2C_{3-y}Au_yO_{7-\delta}$. *Applied Physics Letters* 62(15): 1827-1829.

Fisk, Z., J. D. Thompson, E. Zirngiebl, J. L. Smith and S.-W. Cheong. 1987. Superconductivity of rare earth-barium-copper oxides. *Solid State Communications* 62(11): 743-744.

Frischherz, M. C. Conversation with Frischherz, M. C. 1993.

Frischherz, M. C., M. A. Kirk, J. Farmer, L. R. Greenwood and H. W. Weber. 1994. Defect cascades produced by neutron irradiation in $YBa_2Cu_3O_{7-\delta}$. *Physica C* 232: 309-327.

Frischherz, M. C., M. A. Kirk, J. Farmer and H. W. Weber. 1994. 34-39. Defect cascades produced by neutron irradiation in $YBa_2Cu_3O_{7-\delta}$ superconductors. In *Critical Currents in Superconductors*. Singapore:World Scientific.

Frischherz, M. C., M. A. Kirk, J. P. Zhang and H. W. Weber. 1993. Transmission electron microscopy of defect cascades in $YBa_2Cu_3O_{7-d}$ produced by ion irradiation. *Philosophical Magazine A* 76(6): 1347-1363.

Gao, L., Y. Y. Xue, F. Chen, Q. Xiong, R. L. Meng, D. Rarrirez, C. W. Chu, J. H. Eggert and H. K. Mao. 1994. Superconductivity up to 164 K in $HgBa_2Ca_{m-1}Cu_mO_{2m+2+d}$ (m=1,2, and3) under quasihydrostatic pressures. *Physical Review B* 50(6): 4260 4263.

Giapintzakis, J., W. C. Lee, J. P. Rice, D. M. Ginsberg, I. M. Robertson, R. Wheeler, M. A. Kirk and M. O. Ruault. 1992. Production and identification of flux-pinning defects by electron irradiation in $YBa_2Cu_3O_{7-x}$ single crystals. *Physical Review B* 45(18): 10677-10683.

Gorter, C. J. 1935. Note on the supraconductivity of alloys. *Physica II* 2: 449-452.

Gorter, C. J. 1964. Superconductivity until 1940 In Lieden and as seen from there. *Review of Modern Physics* 36(1): 3-7.

Gray, K. E. and D. H. Kim. 1991. Flux pinning and dissipation in high-temperature superconductors. *Physica C* 180: 139-147.

Hagen, S. J., Z. Z. Wang and N. P. Ong. 1989. Anisotropy of the thermal conductivity of $YBa_2Cu_3O_{7-y}$. *Physical Review B* 40(13): 9389-9392.

Hobbs, L. 1979. *Radiation effects in analysis of inorganic specimens by TEM.* New York: Plenium Press.

Iijima, S., T. Ichihashi, Y. Kubo and J. Tabuchi. 1987. Incipient twinning in $Ba_2YCu_3O_{7-x}$ crystals. *Japanese Journal of Applied Physics* 26: L1790-L1793.

Jin, S., G. W. Kammlott, S. Nakahara, T. H. Tiefel and J. E. Graebner. 1991. Disloctions and flux pinning in $YBa_2Cu_3O_{7-\delta}$. *Science* 253: 427-429.

Jorgensen, J. D., M. A. Beno, D. G. Hinks, L. Soderholm, K. J. Volin, R. L. Hitterman, J. D. Grace, I. K. Schuller, C. U. Segre, K. Zhang and M. S. Kleefisch. 1987. Oxygen ordering and the orthorhombic-to-tetragonal phase transition in $YBa_2Cu_3O_{7-x}$. *Physical Review B* 36(7): 3608-3616.

Jorgensen, J. D., B. W. Veal, A. P. Paulikas, L. J. Nowicki, G. W. Crabtree, H. Claus and W. K. Kwok. 1990. Structural properties of oxygen-deficient $YBa_2Cu_3O_{7-d}$. *Physical Review B* 41(4): 1863-1877.

Joy, D. C., A. D. Romig and J. I. Goldstein, ed. 1986. Principles of analytical electron microscopy. New York:Plenum Press.

Kaiser, D. L., F. Holtzberg, M. F. Chisholm and T. K. Worthington. 1987. Growth and microstructure of superconducting $YBa_2Cu_3O_x$ single crystals. *Journal of Crystal Growth* 85: 593-598.

Kes, P. H. 1987. Recent developments in flux pinning. *IEEE Transactions On Magnetics* Mag-23(2): 1160-1166.

Kirk, M. A. 1993. Structure and flux pinning properties of irradiation defects in $YBa_2Cu_3O_{7-x}$. *Cryogenics* 33(3): 235-242.

Kirk, M. A., M. C. Baker, J. Z. Liu, D. J. Lam and H. W. Weber. 1988. Defect structures in $YBa_2Cu_3O_{7-x}$ produced by electron irradiation. *Materials Research Society Symposium Proceedings* 99: 209-214.

Kirsanov, V. V., N. N. Musin and E. I. Shamarina. 1994. The threshold displacement energies in the high-temperature superconductors. III. The thresholds for oxygen and copper in $YBa_2Cu_3O_7$. *Superconductivity: Physics, Chemistry, Technology* 7(3): 412-421.

Kirsanov, V. V., N. N. Musin and H. J. Shamarina. 1992. Displacement threshold energy in high-temperature superconductors. II Thresholds for O, Ba and Y in $YBa_2Cu_3O_7$. *Physics Letters A* 171: 223-233.

Kirsanov, V. V., N. N. Musin and A. Wisniewski. 1993. Collision cascade progress in the ortho-I and ortho-II phases of YBaCuO. *Physics Letters A* 182: 169-177.

Kirsanov, V. V., N. N. Muslin, D. G. Roskin and E. I. Shamarina. 1993. Collision cascades in HTSC as possible pinning centers. *Cryogenics* 33(5): 477-480.

Kishio, K., K. Suzuki, T. Hasegawa, T. Yamaoto and K. Fueki. 1989. Study on chemical diffusion of oxygen in $Ba_2YCu_3O_{7-\delta}$. *Journal of Solid State Chemistry* 82: 192-202.

Kulik, J. 1991. Defect structures in $YBa_2Cu_3O_{7-\delta}$ with enhanced pinning at low fields. *Journal of Applied Physics* 70(8): 4398-4408.

Kvam, E. P. 1992. Pinning potential of stacking fault-related dislocations in $YBa_2Cu_3O_7$. *Physica C* 200: 409-412.

Kwok, W. K., S. Fleshler, U. Welp, V. Vinokur, J. Downey and G. W. Crabtree. 1991. Flux pinning by planar defects in single crystal $YBa_2Cu_3O_{7-\delta}$. *Physica C* 185-189: 2371-2372.

Lessure, H. S., S. Simizu, S. G. Sankar, M. E. McHenry, J. R. Cost and M. P. Maley. 1991. Critical current density and flux pinning dominated by neutron irradiation induced defects in $YBa_2Cu_3O_{7-x}$. *Journal of Applied Physics* 70(10): 6513-6515.

Li, D. J., H. Shibahara, J. P. Zhang, L. D. Marks, H. . Marcy and S. Song. 1988. Synthesis and structure of copper- and yttrium-rich $YBa_2Cu_3O_{7-x}$ superconductors. *Physica C* 156: 201 207.

London, F. 1950. *Superfluids, macroscopic theory of superconductivity.* New York: John Wiley & Sons.

London, H. 1935. Phase-equilibrium of supraconductors in a magnetic field. *Proceedings of the Royal Society of London* A152: 650-663.

Marks, L. D. 1984. Dispersive equations for high resolution imaging and lattice fringe artifacts. *Ultramicroscopy* 12: 237-242.

Marks, L. D. 1985. Image localisation. *Ultramicroscopy* 18: 33-38.

Marks, L. D. 1996. Wiener-filter enhancement of noisy HREM Images. *Ultramicroscopy* : In Press.

Marks, L. D., D. J. Li, H. Shibahara and J. P. Zhang. 1988. High-resolution electron microscopy of high-temperature superconductors. *Journal of Electron Microscopy Technique* 8: 297-306.

Meissner, W. and R. Ochsenfeld. 1933. Kurze originalmitteilungen. *Naturwissenchaften* 21: 787-788.

Mendelssohn, K. and J. R. Moore. 1935. Supra-conducting alloys. *Nature* 135: 826-827.

Onnes, K. 1911. *Leiden Communication* 120b, 122b, 124c

Paciornik, S., R. Kilaas and U. Dahmen. 1993. Assessment of specimen noise in HREM images of simple structures. *Ultramicroscopy* 50: 255-262.

Parks, R. D. 1965. Quantum effects in superconductors. *Scientific American* 213: 57-67.

Pennycook, S. J. 1990. Direct imaging of the atomic structure and chemistry of defects and interfaces by Z-contrast STEM. MRS Symposia Proceedings, Boston, Materials Research Society.

Pippard, A. B. 1987. Early superconductivity research (except Lieden). *IEEE Transactions On Magnetics* Mag-23(2): 371-375.

Putilin, S. N., E. V. Antipov, O. Chmaissem and M. Marezio. 1993. Superconductivity at 94 K in $HgBa_2CuO_{4+\delta}$. *Nature* 362: 226-228.

Radaelli, P. G., J. L. Wagner, B. A. Hunter, M. A. Beno, G. S. Knapp, J. D. Jorgensen and D. G. Hinks. 1993. Structure, doping and superconductivity in $HgBa_2CaCu_20_{6+\delta}$ (T_c < 128 K). *Physica* C 216: 29-35.

Reimer, L. 1993. *Transmission electron microscopy*. Berlin: Springer-Verlag.

Reyes-Gasga, J., G. v. Tendeloo, T. Krekels, G. v. Tendeloo, J. v. Landuyt, S. Amelickx, W. H. M. Bruggink and H. Verweij. 1989. 3-D vacancy ordered superstructures in "homogenous" $YBa_2Cu_3O_{7-\delta}$. *Physica* C 159: 831-848.

Ringnalda, J., C. J. Kiely, P. Fox and G. J. Tatlock. 1994. Stacking fault structures in melt-processed $YBa_2Cu_3O_{7-\delta}$ superconductors. *Philosophical Magazine A* 69(4): 729-739.

Rothman, S. J., J. L. Routbort, U. Welp and J. E. Baker. 1991. Anisotropy of oxygen tracer diffusion in single-crystal $YBa_2Cu_3O_{7-\delta}$. *Physical Review B* 44(5): 2326-2333.

Saldin, D. K., A. Y. Stathopoulos and M. J. Whelan. 1979. Electron microscope image contrast of small dislocation loops and stacking-fault tetrahedra. *Philosophical Transactions of the Royal Society of London* 292: 523-537.

Schilling, W. 1994. Properties of Frenkel defects. *Journal of Nuclear Materials* 216: 45 48.

Seitz, F. and J. S. Koehler. 1956. Displacement of atoms during irradiation. *Solid State Physics* 2: 307 448.

Shao-Chun, C., Z. Dong-Ming, Z. Dian-Lin, H. M. Duan and A. M. Hermann. 1991. Anisotropic thermal conductivity of $Tl_2Ba_2CaCu_2O8$ and YBa_2Cu_3O7 single crystals: Anomaly in both in-plane and out-of-plane directions. *Physical Review B* 44(22): 12571-12574.

Shimoyama, J., S. Hahakura, K. Kitazawa, K. Yamafuji and K. Kishio. 1994. A new mercury-based superconductor: $(Hg,Cr)Sr_2CuO_y$. *Physica C* 224: 1-5.

Shimoyama, J., S. Hahakura, R. Kobayashi, K. Kitazawa, K. Yamafuji and K. Kishio. 1994. Interlayer distance and magnetic properties of Hg-based superconductors. *Physica C* 235-240: 2795-2796.

Spence, J. C. H. 1988. *Experimental high-resolution electron microscopy.* New York: Oxford University Press.

St. Louis-Weber, M., V. P. Dravid and U. Balachandran. 1995. Facts and artifacts of TEM specimen preparation for $YBa_2Cu_3O_{7-x}$ superconductors. *Physica C* 243: 273 280.

Tafto, T., M. Suenaga and R. L. Sabatini. 1988. Characterization of planar crystal lattice defects in the high-temperature superconductor $YBa_2Cu_3O_7$. *Applied Physics Letters* 52: 667 669.

Takahashi, H., H. Shaked, B. A. Hunter, P. G. Radaelli, R. L. Hitterman, D. G. Hinks and J. D. Jorgensen. 1994. Structural effects of hydrostatic pressure in orthorhombic $La_{2-x}Sr_xCuO_4$. *Physical Review B* 50(5): 3221-3229.

van Tendeloo, G. and S. Amelinckx. 1988. Defect structure of superconducting $YBa_2Cu_3O_{7-\delta}$. *Journal of Electron Microscopy Technique* 8: 285-295.

Vetrano, J. S. 1990. Heavy-ion damage in Cu, Ni and dilute Ni alloys. Ph. D. diss., University of Illinois at Urbana-Champaign.

Viswanathan, H. K., M. A. Kirk, P. Baldo, U. Welp, W. C. Lee, J. Giapintzakis and G. W. Crabtree. 1996. Effect of proton irradiation and annealing on the critical current densities in $YBa_2Cu_3O_{7-\delta}$ Single Crystals. *In Preparation* :

Vlcek, B. M., M. C. Frischherz, S. Fleshler, U. Welp, J. Z. Liu, J. Downey, K. G. Vandervoort, G. W. Crabtree, M. A. Kirk, J. Giapintzakis and J. Farmer. 1992. Flux pinning in $YBa_2Cu_3O_{7-d}$ single crystals: Neutron irradiation and annealing. *Physical Review B* 46(10): 6441-6450.

Wagner, J. L., B. A. Hunter, D. G. Hinks and J. D. Jorgensen. 1995. Structure and superconductivity of $HgBa_2Ca_2Cu_3O_{8+\delta}$. *Physical Review B* 51(21): 15407-15414.

Wagner, J. L., P. G. Radaelli, D. G. Hinks, J. D. Jorgensen, J. F. Mitchell, B. Dabrowski, G. S. Knapp and M. A. Beno. 1993. Structure and superconductivity of $HgBa_2CuO_{4+\delta}$. *Physica C* 210: 447-454.

Werder, D. J., C. H. Chen, R. J. Cava and B. Batlogg. 1988. Diffraction evidence for oxygen-vacancy ordering in annealed $Ba_2Y\ Cu_3O_{7-\delta}$ ($0.3\leq\delta\leq0.4$) superconductors. *Physical Review B* 37(4): 2317-2319.

Wheeler, R., M. A. Kirk, A. D. Marwick, L. Civale and F. H. Holtzberg. 1993. Columnar defects in YBa2Cu3O7-d induced by irradiation with high energy heavy ions. *Applied Physics Letters* 63(11): 1573-1575.

Wilkens, M. 1970. 233-256. Identifictation of small defect clusters. In *Modern Diffraction and Imaging Techniques in Material Science.* Amsterdam:North-Holland Publishing Company.

Wisniewski, A., G. Brandstatter, C. Czurda, H. W. Weber, A. Morawski and T. Lada. 1994. Comparison of fast neutron irradiation effects in $YBa_2Cu_3O_{7-x}$ (123) and $YBa_2Cu_4O_8$ (124) ceramics. *Physica C* 220: 181-186.

Wu, M. K., J. R. Ashburn, C. J. Torng, P. H. Hor, R. L. Meng, L. Gao, Z. J. Huang, Y. Q. Wang and C. W. Chu. 1987. Superconductivity at 93 K in a new mixed phase Y-Ba-Cu-O compound system at ambient pressure. *Physical Review Letters* 58(9): 908-910.

Xu, P., D. Dunn, J. P. Zhang and L. D. Marks. 1993. Atomic imaging of surfaces in plan view. *Surface Science Letters* 285: L479-L485.

Zandbergen, H. W., R. Gronsky and G. Thomas. 1988. Surface decomposition of superconducting $YBa_2Cu_3O_7$. *Physical Status Solidi (a)* 105: 207 218.

Zandbergen, H. W., R. Gronsky, K. Wang and G. Thomas. 1988. Structure of $(CuO)_2$ double layers in superconducting $YBa_2Cu_3O_7$. *Nature* 331: 596 599.

Zhang, H., L. D. marks, Y. Y. Wang, V. P. Dravid, P. Han and D. A. Payne. 1995. Structure of planar defects in $(Sr_{0.9})Ca_{0.3})_{1.1}Cu0_2$ infinite-layer superconductors by quantitative high-resolution electron microscopy. *Ultramicroscopy* 57: 103-111.

Zhu, Y., R. C. Budhani, Z. X. Cai, D. O. Welch, M. Suenaga, R. Yoshizaki and H. Ikeda. 1993. Structure of Au^{+24}-ion-irradiated -induced defects in high T_c superconductors. *Philosophical Magazine Letters* 67(2): 125-130.

Zhu, Y., Z. X. Cai, R. C. Budhani, M. Suenaga and D. O. Welch. 1993. Structures and effects of radiation damage in cuprate superconductors irradiated with several-hundred-MeV heavy ions. *Physical Review B* 48(9): 6436-6450.

Zhu, Y., M. Suenaga and A. R. Moodenbaugh. 1991. Oxygen, diffuse scattering and tweed structure in the $YBa_2Cu_3O_{7-\delta}$ system. *Ultramicroscopy* 37: 341-350.

Ziegler, J. F., J. P. Biersack and U. Littmark. 1985. *The stopping and range of ions in solids.* New York: Pergamon Press.